LUND UNIVERSITY

UNIVERSITY OF MARYLAND 1856

Simulation of colorless distributed combustion

A study of reaction zone, thermal field and pollutant emissions in a model laboratory combustor

Hampus Olsson

Thesis for the degree of Master of Science in Engineering
Division of Fluid Mechanics
Department of Energy Sciences
Faculty of Engineering, Lund University
Lund, Sweden 2019

Thesis for the Degree of Master of Science in Engineering

ISRN LUTMDN/TMHP-19/5444-SE

ISSN 0282-1990

Division of Fluid Mechanics
Department of Energy Sciences
Faculty of Engineering, Lund University
Box 118, 221 00 Lund
Sweden

www.energy.lth.se

Abstract

Colorless distributed combustion (CDC) is a promising novel technology to reduce emissions of carbon monoxide and nitrogen oxides in gas turbine combustors. CDC features a different flame regime than conventional gas turbine combustors, associated with a distributed reaction zone and low and uniform temperatures due to dilution of combustion air with exhaust gases. In this thesis, an attempt has been made at proposing a suitable simulation strategy in order to accurately predict reaction zone, temperature and pollutant emissions for methane-air combustion at an affordable computational cost. The simulations were performed in tandem with experiments on a specific combustor at the Combustion Laboratory of University of Maryland.

The most popular approach in literature was found to be solution of the Reynolds-averaged Navier Stokes equations (RANS) with finite-rate chemistry as modeled by Eddy Dissipation Concept (EDC). Fluid dynamics and chemistry were simulated using the commercial computational fluid dynamics software Ansys Fluent. The non-reacting flow field was predicted using several two-equation and Reynolds stress (RSM) models. The results were compared to particle image velocitmetry (PIV) measurements of the flow field. The reacting flow was then simulated using different global reaction mechanisms and EDC model parameters. Numerical results were compared to experimentally obtained exhaust gas pollutant levels and flame front visualization by OH chemiluminescence.

Results showed best convergence performance using the realizable $k-\varepsilon$ and SSG RSM turbulence models, although additional data are required to make a final choice. Severe issues were encountered when using in-situ tabulation (ISAT) in the reacting flow simulation to accelerate chemistry integration times, which limited the extent of the reacting flow study. Despite this, preliminary findings indicate the need for increased detail in the chemistry, such as by use of reduced or skeletal mechanisms, to correctly predict pollutant emissions.

Acknowledgements

Firstly, I would like to express my gratitude towards Prof. Ashwani K Gupta, who invited me to conduct research in the Combustion Laboratory group at University of Maryland at College Park. I would also like to thank fellow graduate student Joe Feser of the Combustion Laboratory, who provided complimentary experimental data to my simulations and helped me settle in at the laboratory. Secondly, I would like to state my appreciation for Prof. Johan Revstedt and Dr. Rixin Yu of Lund University. Prof. Revstedt supervised this thesis and his support and guidance has been invaluable. Dr. Yu has dedicated his time to guide my research and has patiently answered my many questions about simulation of reacting flows, even those that were apparently just a Google search away. Lastly, I would like to thank my family and Kristyna Herman, who have given me unyielding support and love during difficult times. The completion of this thesis would not have been possible without you.

Contents

List of Figures

List of Tables

Nomenclature

General fluid mechanics and turbulent flow

Symbol	Description	Unit	Symbol	Description	Unit
g	Gravitational acceleration	m/s^2	k	Turbulent kinetic energy	m^2/s^2
ρ	Density	kg/m^3	ε	Turbulent dissipation rate	m^2/s^3
μ	Dynamic viscosity	$Pa \cdot s$	ω	Specific turbulent dissipation	s^{-1}
ν	Kinetmatic viscosity	m^2/s			
$\mathbf{U}$	Instantaneous velocity	m/s	l	Turbulent length scale	m
$\bar{u}$	Mean velocity	m/s	L	Integral length scale	m
u'	Fluctuating velocity	m/s	V_{rms}	RMS velocity fluctuation	m/s
p	Instantaneous pressure	Pa	η	Kolmogorov length scale	m
$\bar{p}$	Mean pressure	Pa	t_η	Kolmogorov time scale	s
p'	Fluctuating pressure	Pa	v_η	Kolmogorov velocity scale	m/s
T	Temperature	K			
β	Coefficient of thermal expansion	K^{-1}			
Re	Reynolds number	-	D	Diameter (dimension)	m
Re_T	Turbulent Reynolds number	-	R, r	Radius (dimension, variable)	m
Gr	Grashof number	-			

Turbulence modeling

Symbol	Description	Unit	Symbol	Description	Unit
ν_T	Turbulent viscosity	$Pa \cdot s$	T_{kij}	Reynolds stress flux	m^3/s^3
S_{ij}	Mean rate of strain tensor	s^{-1}	$\mathscr{R}_{ij}$	Pressure-rate-of-strain tensor	$J/kg \cdot s$
τ_{ij}	Reynolds stress tensor	$m^2/s2$	$\mathscr{R}_{ij}^{(s)}$	Slow pressure-rate-of-strain	$J/kg \cdot s$
a_{ij}	Reynolds stress anisotropy tensor	$m^2/s2$	$\mathscr{R}_{ij}^{(r)}$	Rapid pressure-rate-of-strain	$J/kg \cdot s$
b_{ij}	Normalized anisotropy tensor	-	$\mathscr{R}_{ij}^{(h)}$	Harmonic pressure-rate-of-strain	$J/kg \cdot s$
T_i'	Turbulent energy flux	m^3/s^3	ε_{ij}	Dissipation tensor	$J/kg \cdot s$
$\mathscr{P}_{ij}$	Production tensor	$J/kg \cdot s$	F_{ij}	Production by system rotation	$J/kg \cdot s$
ω_i	Vorticity tensor	rad/s	θ_k	Rotation vector	rad
σ_k	Turbulent Prandtl number	-	Ω_{ij}	Mean rate-of-rotation tensor	rad/s
δ_{ij}	Kronecker delta	-	e_{ijk}	Cyclic permutation operator	-

Combustion

Symbol	Description	Unit	Symbol	Description	Unit
D	Diffusivity	m^2/s	t_c	Chemical time scale	s
s_L	Laminar burning velocity	m/s	t_f	Flow time scale	s
u_F	Flame speed	m/s	Da	Damkohler number	-
l_F	Flame thickness	m	Da_T	Turbulent Damkohler number	-
t_F	Flame time scale	s	Ka	Karlovitz number I	-
l_δ	Fuel consumption layer thickness	m	Ka_δ	Karlovitz number II	-
δ	Fuel consumption layer ratio	-	Φ	Equivalence ratio	-

Combustion modeling

Symbol	Description	Unit
E	Specific internal energy	J/kg
h	Specific enthalpy	J/kg
Y_k	Mass fraction of *k*th species	-
S_E	Energy equation source term	
h_k^0	Enthalpy of formation of *k*th species	J/kg
R_k	Volumetric rate of creation	$mol/m^3 \cdot s$
M_k	Molar mass of *k*th species	g/mol
κ_{eff}	Effective thermal conductivity	$W/m \cdot K$
Pr_t	Turbulent Prandtl number	-
$(\tau_{ij})_{eff}$	Effective deviatoric stress tensor	Pa
$\mathbf{J}_k$	Diffusive flux of *k*th species	m/s
Sc_t	Turbulent Schmidt number	-
$D_{k,m}$	Mass diffusion coefficient	$m^5/kg \cdot s$
$D_{T,m}$	Thermal diffusion coefficient	m^2/s

Symbol	Description	Unit
$\dot{\omega}_k$	Rate of production of the *k*th species	$mol/m^3 \cdot s$
ν'_{ki}	Forward stoichiometric coefficient	-
ν''_{ki}	Reverse stoichiometric coefficient	-
$[\mathscr{X}_k]$	Concentration of *k*th species	mol/m^3
$k_{fi/ri}$	Forward/reverse rate constant of *i*th reaction	$mol/m^3 \cdot s$
q_i	Rate of progress of *i*th reaction	$mol/m^3 \cdot s$
A_i	Pre-exponential factor of *i*th reaction	$mol - cm^3 - s$
β_i	Temperature exponent of *i*th reaction	-
E_i	Activation energy of *i*th reaction	J/mol
Z	Instantaneous mixture fraction	-
$\overline{Z}$	Mean mixture fraction	-
$\overline{Z'^2}$	Mixture fraction variance	-

Radiation modeling

Symbol	Description	Unit
$\mathbf{r}$	Position vector	m
$\mathbf{s}$	Direction vector	m
s	Path length	m
n	Refractive index	-
σ	Stefan-Boltzmann constant	$W/m^{2}\cdot K^{4}
T	Local temperature	K
Ω'	Solid angle	rad

Symbol	Description	Unit
a	Absorption coefficient	-
σ_s	Scattering coefficient	-
I	Radiation intensity	W/m^2
Φ	Phase function	-
ε	Total emissivity	-
$a_{\varepsilon,i}$	Emissivity weighting factor for *i*th gray gas	-
κ_i	Absorption coefficient for *i*th gray gas	-

1

Introduction

1.1 Background

Humanity's use of fossil fuels first became widespread during the industrial revolution of the 18th and 19th century. It did not take long for the rapid development of technology to reach a point where society was completely dependent on the burning of fossil fuels to produce energy. The fact that these resources are exhaustible first became a collective concern during the energy crisis of the 1970s, when the high rate of consumption led to the fear that the fossil fuel reserve will run out in the near future. This spurred the development of new alternative energy sources such as nuclear an solar energy. Although the field of sustainable energy has shown great development since its inception, fossil fuels are still the main source of energy in the world, accounting for about 80% of the total global energy demand in 2017 [1]. The international energy agency, IEA, predicts that even with an optimistic outlook on the achievement of internationally agreed objectives on climate change, fossil fuels will continue to be a major source of energy, accounting for over 70% by 2030 and dropping to 60% by 2040. The predicted energy trends are seen in Figure 1.1.

Besides there being limited reserves, the utilization of fossil fuels is the root of several environmental issues which have generated increasing concern over the last decades. The combustion of hydrocarbons such as coal, oil and natural gas, is an exothermic chemical process in which fuel molecules are consumed in a series of reactions. Completion of

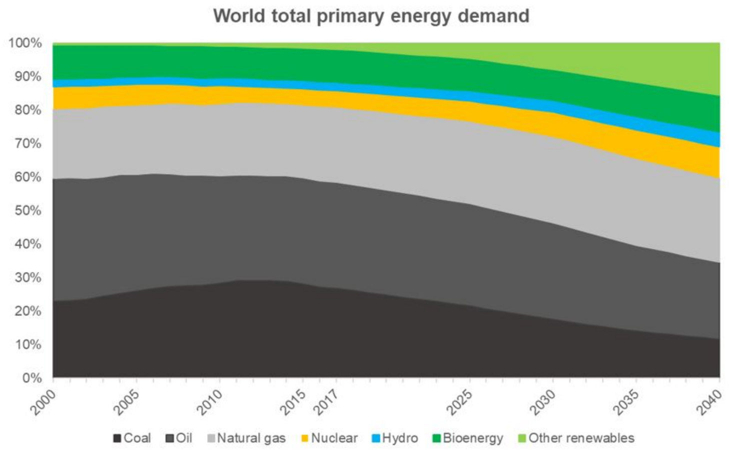

Figure 1.1: History and forecast of global total energy demand. Data provided by IEA, [1].

the process leads to formation of hot product gases, mainly water vapor (H_2O) and carbon dioxide (CO_2), both of which are major contributors to global warming. Combustion products also include pollutants formed in the combustion process, the most notable being nitrogen oxides, NO_x, and sulphur oxides, SO_x. Besides combustion products, the exhaust also contains species of incomplete combustion, such as carbon monoxide, CO, unburned hydrocarbons, HC or UHC, and particulate matter, PM. Many developed countries suffer the effects of air pollution due to combustion exhaust brought on by the rapidly increasing demand for energy and motorization of the private sector. The environmental effects of fossil fuel combustion can therefore be considered in two parts: Contribution to global warming through emission of greenhouse gases and effects on the environment and health through emission of pollutants. Measures to limit the extent of global warming on a large scale were first taken in 1997, when the Kyoto protocol was established to prevent dangerous anthropogenic interference with the climate system by reducing the concentrations of greenhouse gases in the atmosphere. According to recent statistics published by the statistical office of the European Union, eurostat [2], 78% of total CO_2 emissions in Europe during 2016 were related to combustion of fossil fuels. Out of these 78%, 54% were related to stationary applications, such as the production of electricity and heat in power plants. The remaining 24% were related to transport, including both road vehicles and aviation. As such, both stationary and transport combustion systems are key elements in the quest to reduce emissions, although the scope of this thesis only includes the former.

Even though there is increasing competition from renewable technologies such as solar-, wind- and hydro energy, combustion-based energy systems are expected to remain a critical component of the energy market mix. The combustion of fossil fuels still has significant advantages, such as safety and non-radioactivity, reliability, high conversion efficiency and matured distribution and utilization networks [3]. Therefore, research and development of combustion technologies with reduced emissions and improved efficiency is important to meet the global environmental goals. Currently, stationary gas turbines are increasingly popular for production of electricity and are expected to provide the majority of new power generation capacity over the coming decades [4]. Even in a future dominated by renewable energy, they may be necessary as backup for power generation: While solar and wind energy are intermittent sources, gas turbines are quick to start or change load level, which means they can counter sudden changes in electricity demand or wind and sun shortfall [5]. Besides being a primary source of power-generation, gas turbines are the dominant propulsion method for aircraft and are used to produce mechanical work and propel large naval vessels. It should be mentioned that aircraft gas turbines operate under different conditions than stationary turbines, due to constraints imposed by the physics of flight.

The gas turbine operates by burning natural gas or liquid fuels. The hot combustion gases are used to drive a turbine, the shaft of which is connected to a generator. In modern "combined cycle" systems, the hot turbine exhaust is used to raise steam for a steam turbine. Such systems can reach thermal efficiencies (the ratio of produced heat that is transformed into work) in the range of 55-60%, [6], and have superior efficiency and pollutant emission characteristics compared to, for example, coal-fired power plants [4]. Higher thermal efficiencies indicate lower fuel consumption per unit energy produced and thus, lower emissions of CO_2 per unit electricity or unit distance travelled by an aircraft. The thermal efficiency is determined by pressure ratio, measured as ratio of stagnation pressure between compressor inlet and outlet, and turbine Rotor Inlet Temperature (RIT). The latter should be distinguished from flame temperature, as an increase in flame temperature does not necessarily yield higher RIT if the total energy release is unchanged. Reducing flame temperature while keeping RIT constant is one of the main objectives of the colorless distributed combustion technology.

1.2 Gas turbine emissions

On a local level, the environmental goals are implemented in regulations involving criteria for lower emission levels. Although the regulatory pressure to reduce emissions differs between countries, increasing awareness of pollution impact on both the global (through climate change) and local (by air quality) scale is expected to keep increasing the priority of pollutant mitigation. Therefore, gas turbine manufacturers that can offer the lowest emission levels are likely to gain market advantage. In stationary gas turbine applications, the predominant fuels used are natural gas and petroleum-based liquid hydrocarbons. Lately, alternatives to mitigate the addition of CO_2 to the global carbon cycle has attracted interest, such as the use of biofuels. The focus of this thesis, however, is on gas turbines operating on gaseous fuels. The primary pollutant emissions of such gas turbines are NO_x, CO and to a lesser extent HC, as the fuel sulphur content is negligible and PM formation is generally an issue only in aircraft engines [4]. The primary nitrogen oxides that constitutes the sum of NO_x is nitrogen oxide (NO) and nitrogen dioxide (NO_2). NO_x are linked to a number of environmental issues such as the formation of atmospheric nitric acid (e.g acid rain), tropospheric ozone(a main component of photochemical smog), and global warming. Inhalation of CO leads to a reduction of blood oxygen (O_2) transport, resulting in adverse health effects. HC pollution contributes to photochemical smog, and can pose significant health risks, as most hydrocarbons are toxic and carcinogenic. In conclusion, limiting the emissions of these pollutants is of considerable interest to society. To understand the effect of new combustion technology on emissions, an introduction to the conditions that control the production of NO_x, CO and HC will first be made. A detailed explanation is presented in section 2.2.

CO is an intermediary product in the oxidation of hydrocarbons to CO_2. In general, complete conversion to CO_2 (and thus, minimal emission of CO) is favored by high temperatures and long residence times inside the combustor. NO_x formation in combustion of gaseous fuels is mainly related to fixation of atmospheric nitrogen (N_2) with oxygen through three different mechanisms. In conditions relevant to gas turbine combustion, the dominating contribution is through the so called thermal mechanism, for which the reaction rate increases exponentially with temperature, [4]. Low emission of NO_x is therefore favored by low flame temperature. Because the temperature conditions have opposite effects on emission of CO and NO_x, a trade-off must generally be made, [7].

1.2.1 Emission reduction strategies

Due to the onset of stricter regulations, the first emission reduction concepts were developed in the 1990s. One of the most popular ones is "wet control" of NO_x, where the maximum temperature in the combustor is decreased by injection of steam or water. Such systems can produce NO_x levels of 25 ppm using natural gas. However the injected mass flow is generally limited due to additional wear on turbine components and an increase in CO emissions, which limits further reduction of NO_x [8, 6]. In addition, the installment of such systems, including treatment of the water, is bulky and can incur significant operating costs [4]. Recently, technology avoiding injection of water or steam, called "Dry

Low Emissions" (DLE) or "Dry Low NO_x" (DLN), has become well established, where low NO_x emissions are achieved through lean, premixed combustion. Premixed flames features lower flame temperatures than non-premixed flames, which inhibits the thermal mechanism, while operating in fuel-lean conditions inhibits the prompt mechanism. As a result, NO_x levels below 10 ppm can be accomplished for gas turbines burning natural gas near the lean blowout limit. However, DLE/DLN combustors are larger and more complicated in design than ordinary diffusion combustors because they require a premixing chamber [9]. Moreover, the premixing of air and fuel risks premature auto-ignition (spontaneous self-ignition), which has to be carefully managed. In addition, operating near the blowout limit increases the risk of combustion instabilities and can result in high CO and HC emissions. Lastly, the use of premixed flames proves difficult when burning liquid fuels, as premature auto-ignition is a much larger issue than when burning natural gas. Lately, methods have been developed to extend the use of lean premixed combustion to liquid fuels, such as lean direct injection (LDI) and lean prevaporized, premixed (LPP) combustion. However, these technologies pose their own set of problems, such as a high level of complexity and questionable durability and maintainability, [7], and thus are not widely used yet [4]. Another concept that has generated considerable interest is the rich-burn, quick-quench, lean-burn (RQL) combustor. RQL is based on having a fuel-rich primary combustion zone where NO_x formation is inhibited due to low temperature and oxygen levels. Combustion is then completed in a secondary zone downstream, where additional air is injected in a way that promotes uniform mixing. However, the mixing process must be rapid and effective or pockets of high oxygen concentration are formed, resulting in local high temperatures and NO_x formation. Just as with the other emission reduction strategies, the downsides are increased hardware size and complexity of the system [4]. In conclusion, there is need for research on relatively simple, stable systems producing low amounts of both NO_x and CO using gaseous and liquid fuels and that can operate over a wide range of conditions.

Several novel technologies are currently under development to yield such systems. One of the most promising concepts, and the focus of this thesis, is the use of distributed, diluted combustion. Variations of this technology has many names, such as flameless combustion (FC), high temperature air combustion (HiTAC), Moderate and intense low oxygen dilution (MILD) combustion in Italy, flameless oxidation (FLOX) in Germany and Low NO_x injection or colorless distributed combustion (CDC) in the US [10, 3]. No matter what it is called, they all rely on the same basic principles: Dilution of reactants prior to combustion by recirculation of exhaust gases at high turbulence levels and with use of preheated combustion air.

1.2.2 Colorless Distributed Combustion

In a conventional diffusion flame, such as the one present in current jet engines and gas turbines for stationary applications, air and fuel react in a thin flame front that is characterized by high temperature gradients and local temperature peaks or so called hot-spots [10]. The latter are what cause a large degree of NO_x formation through the thermal mechanism [11]. In contrast, the use of exhaust gas recirculation and high turbulence levels in distributed combustion promotes mixing of reactants (fuel or air) with hot product gases prior to combustion [12]. Although the product gas in a globally lean system contains oxygen, the concentration is low in comparison to the air stream. The mixing with product gases alters the reactant mixture in several ways, mainly by lowering the overall oxygen concentration and increasing the heat capacity [13]. The small amounts of oxygen that are entering the fuel stream also allows reaction to begin in fuel rich conditions before the main reaction occurs. Lowering the oxygen concentration increases the auto-ignition time of the combustion process [14]. This allows the reactant mixture to distribute throughout the combustor volume before reaction. Because the volume where heat is released is greater, peak temperatures are reduced for a given amount energy release. The resulting distributed reaction zone occupies a large part of the combustor and is characterized by a homogeneous temperature field with little fluctuations and no hot spots [10, 12]. The reaction zone is therefore drastically different from that of a diffusion flame. Production of pollutants is greatly lowered [12, 15, 14]. In addition, the thermo-acoustic instabilities, which generate combustion noise, are severely reduced [16]. These characteristics make CDC combustion an ideal candidate to reach the aforementioned environmental goals.

1.3 Objectives and limitations

Development of CDC still requires significant work before it can be implemented in an industrial gas turbine combustor. The specific conditions required to achieve CDC are highly sensitive to the fluid flow through the combustor, which is difficult to investigate using purely experimental means. Complex fluid flows are best studied using a full field approach, which can be achieved through the implementation of a validated computational fluid dynamics (CFD) model. Numerical simulation can also prove an efficient tool in design of a practical combustor, as it is considerably cheaper and faster than constructing prototypes and performing experiments. The main objective of this thesis is to develop a simulation strategy to accurately predict the reaction zone, temperature and pollutant emissions for methane-air combustion at an affordable computational cost using commercial software ANSYS Fluent. The simulation model will be validated with experimental data obtained at the University of Maryland Combustion Laboratory to assess accuracy of different model approaches and provide a final suggestion for future computational setups. To accomplish this goal, the project was divided into the following activities:

1. Study set-up of mesh and boundary conditions.
2. Study choice of turbulence model in a non-reacting flow by comparing PIV measurements and simulations.
3. Study the capability of global chemical mechanisms for methane combustion to predict reaction zones, temperature field and pollutant emissions.

The simulations were split into study of non-reacting and reacting flows. Initially, the (cold) mixing of air and fuel was investigated through experiments and CFD simulation. This way, the accuracy of boundary conditions and turbulence model could be studied with minimal disturbances. Then, actual combustion of air and methane was investigated, with a focus on investigating the ability of simple global reaction mechanisms and effect of combustion model parameters. Simulations were limited to the Reynolds Averaged Navier Stokes (RANS) equations. More advanced calculations, such as Large Eddy Simulation (LES), were not performed due to significantly longer computational times. Especially when coupled with the complexity added by reacting flow, performing such simulations would have been impossible under the scope of this thesis. Use of combustion model was limited to the Eddy Dissipation Concept (EDC), as it provides relatively high accuracy in comparison to computational cost. Based on the same argument as applied to choice of RANS flow equations, the EDC model was chosen over more detailed yet expensive models, such as transported PDF methods. Experimental data was generated using a single high frequency particle image velocimeter (PIV) and in the reacting case, chemiluminescence, thermocouple and emission probe measurements. Due to the restrictions imposed by this setup, comparison of any three-dimensional fields are omitted, as are distributions of different species.

1.4 Disposition

The previous chapter has explained the background, motivations and details of the conducted research in the subject of colorless distributed combustion. Next, underlying theory will be presented, such as the chemical kinetics which govern formation of pollutants, historical, physical and chemical aspects of colorless distributed combustion and an introduction of the models used in the CFD analysis. Once all necessary concepts have been introduced, the computational set-up will be presented, followed by a discussion of numerical and experimental results. Lastly, a conclusion regarding the simulation strategy will be made and future areas for further research will be identified.

2

Theory and method

2.1 Fundamentals of Combustion

Combustion can be summarized as an exothermic chemical reaction between a fuel and an oxidant. It can occur in many forms and although one might assume that combustion is accompanied by a visible flame or luminescence, this is not always the case. In gas turbine applications, the oxidant is always oxygen present in the air, while the fuel may be either gaseous or liquid. Combustion includes a plethora of different physical and chemical processes, which authors have spent entire books describing. Therefore, the following is a short introduction to the most important aspects of gas turbine combustion by relevance to this thesis. The following section is based on the work by Lefebvre and Ballal [7], which would also serve as a reference for those who want to delve deeper into the matter.

Combustion can generally be divided into two different modes. In the premixed mode, reactants are mixed at the molecular level before ignition. Many low-NO_x gas turbine combustors burning natural gas operate in this mode, as mentioned previously in the introduction. In the non-premixed mode, also called diffusion mode, fuel and oxidizer enter the reaction zone in separate streams. Most gas turbine combustors burning liquid fuel, such as aircraft jet engines, generally operate in the non-premixed mode. Microscopically, the flame can be defined as a rapid change of chemical composition over a thin fluid layer, featuring large gradients of species concentrations and temperatures. The burned mixture has elevated temperature and higher volume but lower density than the unburned mixture. On a macroscopic level, the flame can be seen as an interface between the unburned and burned mixture. If the mixture is stationary, such as in internal combustion engines, this interface will propagate at a certain flame velocity. For hydrocarbon flames, the flame velocity is generally below 1 m/s. In gas turbine engines, the flame is usually stabilized at a fixed point where it is supplied with a continuous flow of fuel and air. Depending on the Reynolds number of the flow (and other parameters related to laminar - turbulent transition), the flame may be further classified as either laminar or turbulent. These different combustion modes are depicted in figure 2.1.

As previously mentioned, combustion include multiple topics in both chemistry and physics. In terms of the latter, we are mainly concerned with thermodynamics, fluid dynamics, gas dynamics, heat transfer and mass transfer. For most traditional gas turbine combustors, completion of the chemical oxidation process occurs rapidly in comparison to physical processes, such as interdiffusion or turbulent mixing of reactants. These are then the rate-controlling mechanisms of the combustion process. However, in colorless

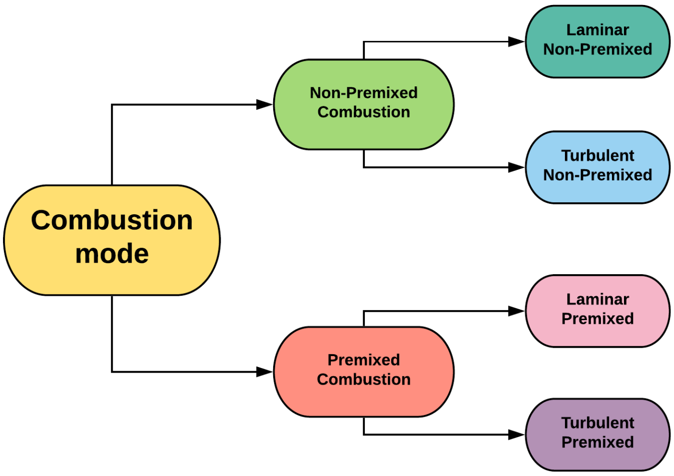

Figure 2.1: Combustion mode classification.

distributed combustion (CDC), oxidation processes are associated with a low Damköhler number (the ratio of flow and chemical time scales) and thus physical processes may no longer be the rate limiting step [13]. Larger emphasis must then be put on correctly resolving the underlying chemistry. For any combustion regime, chemistry also plays a large role in the subject of pollutant emissions [7].

2.1.1 Turbulent combustion

Because most fluid flows in engineering applications are turbulent, the flames in combustion applications are also turbulent. Flame speeds in turbulent combustion are elevated in comparison to laminar flames. The increase in flame speed, or burning rate, is attributed to wrinkling of the flame front, which leads to an increased surface area in contact with fresh mixture [7]. As noted by Peters [17], turbulence in itself is one of the most significant unresolved problems in classical physics, and things become considerably more complicated when adding combustion to the table. Mathematical modeling of turbulence is usually based on the so-called eddy cascade hypothesis for high Reynolds number flows. In the eddy cascade hypothesis, the turbulent flow is represented by large eddies that break up into consecutively smaller and smaller eddies, until the smallest eddies, with sizes comparable to the so called Kolmogorov length scale, dissipate into heat due to viscous effects. Similar concepts have been implemented in the modeling of turbulent combustion. Peters [17] made a rigorous treatment of this subject and the following is a summary based on his work.

For combustion to take place, fuel and oxidizer must mix at the molecular level. In turbulent combustion, this takes place through turbulent mixing, where shear and strain at the interface between eddies enhance mixing. Because the strain and shear increase with decreasing eddy size, the largest concentration gradients are found at the small eddies. Larger concentration gradients then lead to increased rates of molecular diffusion. Therefore, molecular mixing of fuel and oxidizer take place at interfaces between the smallest eddies, in the so called inertial subrange, and this also applies to the transport of radicals and heat released in the combustion process. To complicate things further, as fuel and reactants are consumed during the combustion process, the concentration gradients are further increased. The resulting increase in molecular diffusion then accelerates the combustion process. In general, chemical reactions in combustion elevated temperatures are fast in comparison to all turbulent time scales and take place in thin layers that are usually smaller than the Kolmogorov scale. If combustion takes place at time and length scales that are separated from those of turbulence, the mixing process in the inertial subrange may be considered independent of chemical effects. Most turbulent combustion models are based on this concept of scale separation, [17].

The structure of the flame will be affected by the level of turbulence, through the effect on turbulent velocity and length scale ratios. In premixed combustion, the flame structure can be divided into three layers. These are the inert preheat zone, the reacting fuel consumption layer, the width of which is denoted δ, and the reacting oxidation layer. It is possible to define a velocity scale, the laminar burning velocity, s_L, which is the velocity at which the flame front propagates perpendicular to itself and into the unburnt mixture. It is a property of the mixture (its fuel structure and equivalence ratio) and the thermodynamic conditions (pressure and temperature). We may also define a length scale as the flame thickness, l_F, and a time scale, t_F, based on the laminar burning velocity and the diffusivity D,

$$l_F = \frac{D}{s_L}, \quad t_F = \frac{D}{s_L^2} \quad D = \frac{\kappa}{\rho c_p} \quad . \tag{2.1}$$

In equation (2.1), κ is the thermal conductivity, ρ the density and c_p the isobaric heat capacity of the fluid. Using these quantities, the RMS velocity fluctuation V_{rms} and the turbulent length scale l, we can define a turbulent Reynolds number and a turbulent Damköhler number,

$$Re_T = \frac{V_{rms}}{s_L l_F}, \quad Da_T = \frac{s_L l}{V_{rms} l_F} \quad . \tag{2.2}$$

We may also define two Karlovitz numbers, as the ratio of chemical time scale and Kolmogorov time scale t_η and the ratio of the fuel consumption layer thickness l_δ to the Kolmogorov length scale η,

$$Ka = \frac{t_F}{t_\eta} = \frac{l_F^2}{\eta^2} = \frac{v_\eta^2}{s_L^2}, \quad Ka_\delta = \frac{l_\delta^2}{\eta^2} = \delta^2 Ka \quad . \tag{2.3}$$

where δ corresponds to the fraction of the flame thickness occupied by the fuel consumption layer. With these definitions, it is possible to set up a regime diagram, where the ratio of turbulent and flame velocity scales, V_{rms}/s_L, is plotted against the ratio of turbulent and flame length scales, l/l_F. The result is shown in figure 2.2, where different regimes correspond to different behaviours of the flame, dictated by the interaction between turbulence and chemistry. The different regimes are separated by specified values of Re, η, Ka and Ka_δ. While most premixed gas turbine combustors operate in the corrugated flamelets or thin reaction zones regime, Khalil and Gupta [10] have showed that CDC operate in the broken reaction zones regime. This regime is defined by $Ka > 1$ and $Ka_\delta > 1$. According to equation (2.3), the former implies that the smallest eddies can enter the flame structure as $\eta < l_F$. This interchange promotes mixing. The second inequality implies that the fuel consumption layer width is larger than the Kolmogorov length scale [17]. At this point, the scale separation assumption becomes invalid, which could present a problem when using standard turbulence combustion models to simulate CDC. Although this regime diagram is based on premixed combustion, it could be relevant for CDC even when fuel and air enter the combustor separately, as the high level of recirculation and turbulent mixing

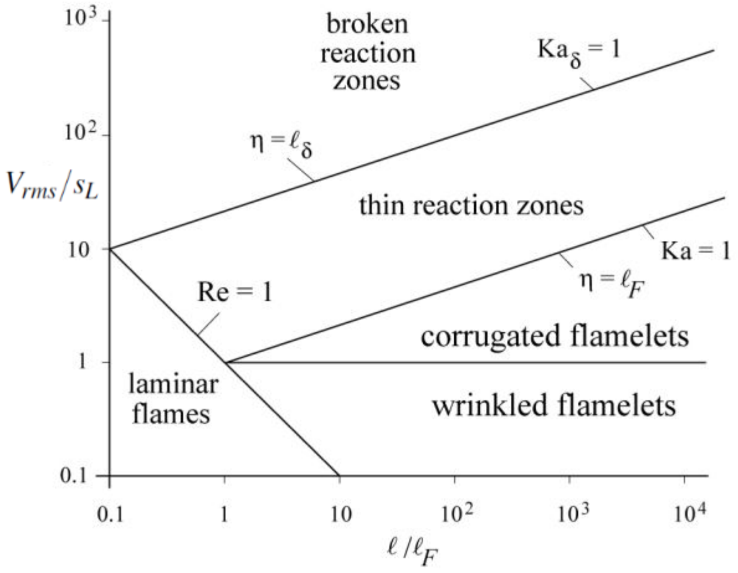

Figure 2.2: Premixed combustion regime diagram. Adapted with permission from Peters [17].

promotes a nearly homogeneous distribution of reactants, similar to a well-stirred reactor. Another way to characterize CDC as a reaction regime is to produce an adapted so called Borghi diagram, where the axes are Damköhler number and turbulent Reynolds number. This is explained further in section 2.3.2.

2.2 Emission formation

Understanding the chemical kinetics governing the formation of combustion pollutants is necessary in order to assess the effect of emission reduction strategies such as CDC. A brief introduction to the mechanisms governing CO and NO_x formation and HC emissions will now be made. For more detailed explanations, the reader is referenced to Lieuwen and Yang, [4], and Correa, [11].

2.2.1 Carbon dioxide and carbon monoxide

Based on combustion conditions, the oxidation of hydrocarbons can be classified into three different regimes based on temperature. These are the low, intermediate and high temperature oxidation regimes, which feature different reaction pathways. Although the oxidation pathways are not only dependent on temperature, most gas turbine combustors can be said to operate in the high temperature regime [4]. In this regime, combustion can be viewed in a simplified way as starting with two fundamental steps. First, hydrogen (H) is scissioned from the hydrocarbon and reacts with oxygen (O_2) to form HO_2 and HO. Hydrocarbons then react with these oxygenated combustion species to form formaldehyde (CH_2O). In general, formaldehyde then decomposes into either the formyl radical (HCO) or CO through thermal dissociation (collision with a third-body species, M) according to reactions 1 and 2, respectively,

$$CH_2O + M \rightleftharpoons HCO + H + M \tag{1}$$
$$CH_2O + M \rightleftharpoons CO + H_2 + M \tag{2}$$

CH_2O may also chemically decompose to HCO through reacting with H, O, OH or HO_2,

$$\begin{aligned} CH_2O + H &\rightleftharpoons HCO + H_2 && \{3\} \\ CH_2O + O &\rightleftharpoons HCO + OH && \{4\} \\ CH_2O + OH &\rightleftharpoons HCO + H_2O && \{5\} \\ CH_2O + HO_2 &\rightleftharpoons HCO + H_2O_2 && \{6\} \end{aligned}$$

HCO formed through reactions 1 and 3-6 forms CO through thermal dissociation, 7, or oxidation, 8, as

$$\begin{aligned} HCO + M &\rightleftharpoons CO + H + M && \{7\} \\ HCO + O_2 &\rightleftharpoons CO + HO_2 && \{8\} \end{aligned}$$

Finally, CO reacts with any of OH, HO_2, O and O_2 to form CO_2 through the following reactions,

$$\begin{aligned} CO + OH &\rightleftharpoons CO_2 + H && \{9\} \\ CO + HO_2 &\rightleftharpoons CO_2 + OH && \{10\} \\ CO + O{\equiv}M &\rightleftharpoons CO_2 + M && \{11\} \\ CO + O_2 &\rightleftharpoons CO_2 + O \quad . && \{12\} \end{aligned}$$

For high temperatures, 9 is the principal contributing reaction due to lower reaction rates for reactions 10 - 12, [4]. In general, complete conversion of CO to CO_2, i.e completion of reactions 9 - 12, is favored by high temperatures and long residence times inside the combustor.

2.2.2 Nitrogen oxides

Studies of NO_x emissions can usually be restricted to NO that is formed during combustion, as NO_2 is primarly formed through further reaction of NO downstream of the combustion zone [6]. Atmospheric nitrogen in the combustion air reacts to form NO through four main pathways: thermal NO, prompt NO, through the N_2O path and through the NNH path. The thermal mechanism is heavily temperature dependent and is one of the major sources of NO in combustors where temperatures above 1800 K are reached, as is the case in most gas turbines. High temperatures are required because fixation of nitrogen first requires breaking of the strong N_2 bond. In the thermal mechanism, nitrogen reacts with oxygen in a set of reactions known as the extended Zeldovich mechanism,

$$\begin{aligned} N_2 + O &\rightleftharpoons NO + N && \{13\} \\ N + O_2 &\rightleftharpoons NO + O && \{14\} \\ N + OH &\rightleftharpoons NO + H && \{15\} \end{aligned}$$

where reaction 13 is the rate limiting step due to its high activation energy. Because the concentration of atomic oxygen (O) in the flame is essentially an exponentially increasing function of temperature, thermal NO formation shows a similar trend.

NO is formed through the N_2O path when atmospheric nitrogen reacts with an O atom in a third-body reaction, 16, producing N_2O as opposed to the thermal route in 13. N_2O

then reacts further with oxygen or hydrogen, forming NO according to reactions 17 and 18, respectively.

$$N_2 + O + M \rightleftharpoons N_2O + M \tag{16}$$
$$N_2O + O \rightleftharpoons 2\,NO \tag{17}$$
$$N_2O + H \rightleftharpoons NO + NH \tag{18}$$

N_2O can also disassociate, returning to N_2 and O_2 or OH according to reactions 19 and 20,

$$N_2O + O \rightleftharpoons N_2 + O_2 \tag{19}$$
$$N_2O + H \rightleftharpoons N_2 + OH \tag{20}$$

The N_2O route features relatively slow reactions and is therefore overshadowed by other mechanisms except under lean, low temperature conditions, where the other mechanisms are inhibited. It also plays a larger part under elevated pressures due to an increased rate of reaction 16. It is therefore expected to be a major contributor in CDC applications, at both atmospheric and operational pressure levels.

Prompt NO is governed by reaction of hydrocarbon radicals with molecular N_2, as opposed to interaction between a single O atom and N_2 in the thermal and N_2O mechanisms. Although there is some disagreement about the reaction paths of the prompt mechanism, it is deemed plausible that hydrocarbon radicals, particularly CH, react with N_2 to form an intermediary species HCN, which then further reacts with OH or O to form NO. The reaction route that is considered in Ansys Fluent is the following:

$$CH + N_2 \rightleftharpoons HCN + N \tag{21}$$
$$N + O_2 \rightleftharpoons NO + O \tag{22}$$
$$HCN + OH \rightleftharpoons CN + H_2O \tag{23}$$
$$CN + O_2 \rightleftharpoons NO + CO \tag{24}$$

Prompt NO is predominant only in rich mixtures, where the quantities of hydrocarbon radicals are greater. It is therefore expected not to be a significant contributor in CDC combustion.

2.2.3 Unburned hydrocarbons

UHC or HC includes any fuel species that exit the combustor as liquid droplets or vapor. HC contains a combination of unburned fuel and species of lower molecular weight that are formed through thermal degradation of primary fuel. Fuel and fuel derivatives can remain unburned due to low burning rates, quenching of the flame by cooling air and, in gas turbines operating on liquid fuel, inadequate atomization. Although the chemical kinetics that describe HC formation are too complex to describe here, HC emissions are generally dependent on similar conditions as those that govern CO emission. As such, HC emissions are reduced by longer residence times and higher combustor temperatures, [7].

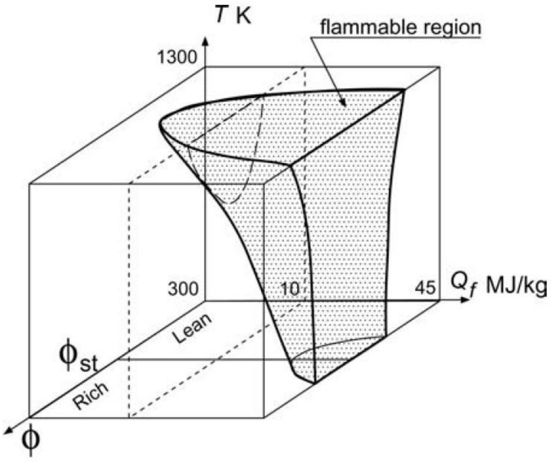

Figure 2.3: Flammable domain by mixture equivalence ratio ϕ, fuel calorific value Q_f and initial mixture temperature T. Reprinted with permission from Tsuji et al. [18].

2.3 Colorless distributed combustion

To achieve a deeper level of understanding of the application of CDC to gas turbine engines, it should first be described in relation to previous combustion technologies to unravel the fundamental similarities and differences between conventional combustion regimes and CDC.

2.3.1 Preliminaries and furnace combustion

In the 1980s, research was being made on ultra-lean combustion in industrial furnaces to reduce NO_x emissions. Ultra-lean mixtures near the flammability limit do not burn under normal conditions and thus require special measures. One possible option is the use of preheated air, as both rich and lean flammability limits are expanded with higher air temperature for a given calorific value of the fuel (the amount of energy released when a fuel undergoes complete combustion with oxygen under standard conditions) [18]. This effect is depicted in figure 2.3. Combustion air, or a mixture of air and fuel, was preheated by recycling of heat from hot flue gases using regenerative heat exchangers, which allowed a large amount of waste heat to be recovered. Depending on the level of preheating, fuel savings of 30% to 50% could be achieved [19]. However, preheating also increases the flame temperature, resulting in higher emissions of NO_x due to a drastic increase in reaction rate of the thermal NO_x mechanism. Another concern was the temperature limit imposed by the furnace material, which requires external cooling if temperatures near the tolerance limit are reached [18]. Because the thermal efficiency increases with rising levels of preheating, the trade-off between efficiency, emission control and tolerance of materials was, and still is, a critical consideration in combustion system design [18].

During the development of one particular experimental staged combustor heat-recirculating furnace in Japan, a surprising phenomenon was detected. During operation, no visible flame could be seen and even though the combustion air was preheated to 1400 K, emissions of NO_x and CO were measured in single digit percentages [19]. The cause was found to be a combination of the highly preheated combustion air and the combustor configuration. The geometry of the combustor, positioning of fuel nozzles and high momentum of the air jet allowed internal recirculation of exhaust gases, which mixed and diluted the air and fuel jets [18]. This marked the discovery of a new combustion regime, different from that of normal diffusion or non-premixed flames, which was termed flameless oxidation (FLOX) in Germany, moderate and intense low oxygen dilution (MILD) combustion in Italy and high temperature air combustion (HiTAC) in the US and Japan. The combination of low and controlled flame temperature, uniform thermal field in the entire combustion zone, reduced fuel consumption and reduced formation of NO_x and other pollutants such as CO, UHC and soot are clearly ideal characteristics and spurred intense research both in industry and academia [19]. New flame visualization techniques, such as Laser Sheet Visualization and methods based on luminescence intensity of excited combustion species were developed in the late 90s and allowed a more thorough mapping of this newly discovered combustion mode. Weber, Smart, and Kamp [14] made the following observations for HiTAC using gaseous fuel in furnace applications:

1. Combustion air is preheated to temperatures above 1000 C.
2. The furnace exit temperature is only marginally higher than the combustion air inlet temperature, showing an increase of around 50-100 C.
3. The fuel nozzles should be positioned such that the fuel is injected into the recirculated hot flue gases.
4. The recirculated flue gases have low oxygen concentration, typically in the range of 2-5 volume %.
5. Fuel and air jets entrain large quantities of flue gases before mixing with each other.
6. The combustion process takes place globally in the furnace and typically shows no visible flame. The combustor behaves similarly to a well-stirred reactor.
7. The furnace temperature and oxygen fields are relatively uniform with the largest gradients found close to the burner. The radiative fluxes are uniform.

While these observations were made for specific furnaces, they give an idea of what to be expected from HiTAC in general, and consequently also the application of similar combustion technology to gas turbine combustors. Since the 90s, practical developments of HiTAC technology in academia and industry has led to considerable progress in simultaneously achieving fuel savings and reduction of NO_x emissions.

The two key mechanisms of air preheating and recirculation of exhaust gases have been studied extensively in furnace applications, but it should be noted that the process has many similarities with CDC for gas turbine applications, except for the considerably shorter residence times and higher pressures that characterize a gas turbine combustor. As such, an attempt to describe the physical and chemical phenomena that govern this combustion regime will now be made based on literature by Tsuji et al. [18].

When fuel and air mixes, an amount of heat must be supplied to overcome the reaction activation energy and start the combustion process. At ambient conditions, a flame holder or pilot flame is used to supply the activation energy. A strong shear flow may cause blow-off and flame extinction, which would affect the entire flame zone. However, sufficient preheating of the air will cause the fuel to auto-ignite somewhere downstream in the furnace, removing the need for a flame holder while also increasing flame stability, as it would not be affected by blow-off. The "high temperature" in HiTAC is defined as the air temperature at which a gaseous fuel auto-ignites and combustion becomes self-sustaining. The second key mechanism, exhaust gas recirculation, was a known technique to decrease flame temperature before it was coupled with air preheating, but the extent of the temperature decrease was limited due to flame extinction. In ambient conditions, combustion generally becomes unstable when the recirculation ratio, defined as the mass flow ratio between recirculated gases and fresh reactants, exceed 30%. However, addition of preheated air above the fuel auto-ignition temperature expands the flammability limit, allowing stable combustion at much higher recirculation ratios (>3) and low single digit oxygen levels.

The combustor is designed so that fuel and air jets are directed into the recirculated flue gases separately. The combustion process that follows can then be explained in two stages. The first stage is in rich conditions, where the fuel jet has entrained hot, inert product gases (mostly CO_2 and H_2O) of low oxygen concentration but not yet mixed with the air jet. This entails an increase in ignition delay while keeping the oxidation reaction time relatively low. The second stage is in lean conditions, when the diluted fuel and air jets mix, [14]. Homogeneous distribution of the air-fuel mixture is promoted by strong recirculation and high turbulence levels. As the fuel-air mixture has a lower oxygen concentration, reaction rates are lower, allowing the mixture to spread out into a large part of the furnace volume before combustion occurs. Because the local reaction rate is smaller while the reaction volume is larger, the total heat release is the same as that of a diffusion or non-premixed flame. Lower reaction rates imply lower heat release rates and consequently lower temperature peaks as well as smaller temperature fluctuations [14]. Reduction of the maximum temperature inhibits NO_x production through the thermal mechanism. Smaller temperature fluctuations also mean that the operating temperature of the furnace can be increased in HiTAC without exceeding the material limit. Consequently, the thermal load can be increased, or alternatively a smaller size furnace can be used for the same load [18].

Similarly to the definition of HiTAC made by Tsuji et al., Cavaliere and De Joannon [13] made a rigorous definition of what they called MILD combustion. The authors defined the MILD combustion regime in the following way: "A combustion process is named MILD when the inlet temperature of the reactant mixture is higher than mixture self-ignition temperature whereas the maximum allowable temperature increase with respect to inlet temperature during combustion is lower than mixture self-ignition temperature (in Kelvin)". This definition shares many similarities with that of HiTAC, as the temperature in the latter can be controlled through the transfer of heat and mass of hot product gases into the inlet reactant stream. The mixture self-ignition temperature of a well-stirred reactor is defined as the inlet temperature of which any incremental temperature increase causes the system to reach a state where the chemical process is self-sustaining. Furthermore, MILD combustion was concluded to differ from other combustion regimes in that the evolution of the latter is characterized by a wide temperature range where kinetics and physical parameters may change abruptly or chaotically during the process. In MILD combustion, a gradual evolution is achieved. Except for the requirement of a maximum temperature increase in MILD combustion, which will be inherently fulfilled in most if not all cases, it is seen that the definitions of HiTAC and MILD combustion are nearly identical.

2.3.2 Combustion phenomena of CDC in gas turbine applications

The characteristics that make HiTAC or MILD combustion desirable in industrial furnaces are clearly desirable in essentially any combustion process, for example in gas turbine applications. Although HiTAC furnaces have been available on the market for some time, development is still required for the combustion technology to be available for gas turbine use. This can largely be attributed to fundamental differences in the way these systems work. Furnaces generally operate at atmospheric pressure levels and low thermal intensity (TI $\sim 0.1-1$ MW/m^{3}atm), whereas stationary gas turbines operate at high intensities (TI ~ 20 MW/m^{3}atm) [15] and elevated pressures ($\sim 3-5$ bar) [9]. In addition, gas turbine engines pose different constraints in terms of available space and acceptable geometries of a potential modified combustor. Nevertheless, as previously mentioned, many of the underlying mechanisms are nearly the same. This allows us to extend fundamental thermodynamic aspects of HiTAC, (Tsuji et al. [18]) and MILD combustion, as reviewed by Cavaliere and De Joannon, [13], for applications to CDC.

Thermal field uniformity

The thermal field of CDC has been mentioned to be uniform in temperature and to show small gradients. Cavaliere and De Joannon [13] performed thermodynamic analyses, namely heat balance and equilibrium evaluation, to obtain three important quantities that describe the temperature range covered by the system. These quantities are the frozen temperature, the equilibrium temperature and the maximum temperature. By use of these three temperatures, the thermal field of CDC can be compared to that of a diffusion flame. The frozen temperature, being the initial temperature of the air-fuel mixture, is defined as a weighting of inlet temperatures of the separate air and fuel streams, being a function of mixture fraction Z. $Z=1$ and $Z=0$ corresponds to the pure fuel and air streams, respectively. $T_{frozen}(Z=1)$ is then the inlet fuel temperature and $T_{frozen}(Z=0)$ the inlet air temperature. The maximum temperature is defined as the temperature resulting from complete oxidation of reactants into CO_2 and H_2O. Lastly, the equilibrium temperature is the temperature the system would reach if evolving from the initial condition without constraints, meaning that it can imply non-complete oxidation. In the undiluted case, the system evolves from initial towards the maximum temperature because the initial temperature is too low for auto-ignition. It may then decay towards the equilibrium temperature. The system temperature at some value of mixture fraction must therefore be bounded by the maximum and equilibrium temperatures. In contrast, in the diluted case the longer residence times and possibly higher air inlet temperature allows the system to evolve directly towards either the equilibrium or maximum temperature. The system temperature is then bounded by the maximum and initial temperatures. If the simultaneous existence of both flames was possible, diluted combustion would therefore imply larger temperature variations for a given oxygen concentration X_{O_2}. In the practical case, this turns out to be counteracted by the influence of dilution, which reduces X_{O_2}. Cavaliere and De Joannon [13] plotted analytic expressions of the frozen, equilibrium and maximum temperatures, acquired through heat- and equilibrium balances, for a CH_4-N_2-O_2 system. Temperature as a function of mixture fraction was plotted for two initial conditions, one representing an undiluted mixture without preheating and one a diluted mixture with preheating. These correspond to standard cases of a diffusion flame and preheated distributed flame, respectively, and are found in figure 2.4.

As can be seen, the maximum system temperature decreases from about 2600 K to

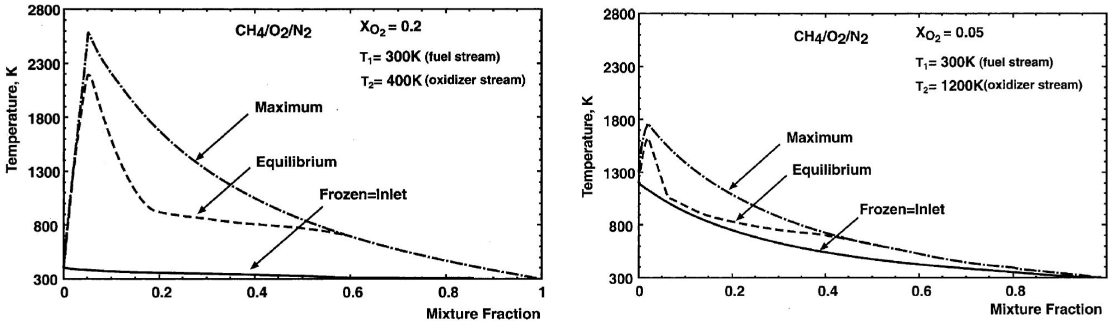

(a) Diffusion flame

(b) Distributed flame

Figure 2.4: Frozen (initial), equilibrium and maximum temperatures for undiluted and diluted conditions. Reprinted with permission from Cavaliere and De Joannon [13].

1800 K and the maximum temperature difference decreases from around 900 K to 600 K when the air is preheated and diluted. Another interesting observation is that for the diluted case, the equilibrium and frozen conditions differs only by a small amount.

Temperature fluctuations, heat release fluctuations and noise

Besides producing a more uniform mean thermal field, HiTAC and CDC have also been shown to dramatically reduce both temperature fluctuations and heat release fluctuations. While temperature fluctuations of 50 to 100 K are common in many turbulent non-premixed flames, in one case HiTAC was shown to produce fluctuations below 5 K using air preheated to 1200 °C at 4% O_2, measured at the point of maximum mean temperature [18]. An important aspect to achieving clean combustion in gas turbines is the dynamic stability of the flame and how it responds to fluctuations in the inlet air stream. Heat release instabilities generated by such perturbations can cause feedback and resonance phenomena, leading to local flame extinction and even damage to the combustor. Feedback is caused by local density variations as a result of heat release fluctuations, which in turn lead to pressure oscillations. These travel upstream in the form of acoustic waves, interfering with the inlet air stream. The pressure oscillations are also correlated with combustion noise. Khalil and Gupta [16] investigated such phenomena for swirl assisted distributed combustion in a methane-air flame diluted with N_2 and CO_2. In normal swirl combustion there was a strong correlation between acoustic sound pressure and heat release fluctuations at 200 Hz, which indicates the possibility of feedback. Distributed combustion, achieved with oxygen levels below 15%, showed no such correlation. In addition, the heat release fluctuations were reduced by some 50% and the sound pressure level was reduced by 17 dBA. In conclusion, MILD combustion shows increased stability in comparison to diffusion flames, while also producing significantly lower combustion noise. The latter is an especially interesting characteristic if considering application in jet engines for commercial aircraft, as reducing noise has seen increasing interest lately [20].

Flame-turbulence interaction

In turbulent combustion, the interaction between the turbulent flow field and the flame dictates the combustion behaviour. Consequently, it can be described in terms of turbulence and flame characteristic quantities. Khalil and Gupta [10] used particle image velocimetry (PIV) to investigate the flow field of a laboratory premixed swirl combustor operating. The captured flow field was used to assess the interaction between flame and flow characteristics by comparing turbulence quantities, namely the integral length scale and turbulent Reynolds number, and reaction time scale quantities, which were flame thickness and laminar flame speed. The flame-turbulence interaction was evaluated using the Damköhler number, Da, and turbulent Reynolds number, Re_T. The Damköhler number is defined as the ratio of flow time scale to chemical time scale,

$$Da = \frac{t_f}{t_c} \quad , \tag{2.4}$$

where t_f is the flow time scale, defined by the integral length scale L and root-mean-square velocity fluctuation V_{rms}:

$$\begin{aligned} t_f &= L/V_{rms} \\ t_c &= l_F/u_F \quad . \end{aligned} \tag{2.5}$$

The chemical timescale t_c is defined by flame thickness, l_F and flame speed u_f. The turbulent Reynolds number is defined as the ratio of inertial and viscous forces at the integral length scale,

$$Re_T = \frac{V_{rms}L}{\nu} \quad , \tag{2.6}$$

where ν is the kinematic viscosity of the fluid. The Damköhler and turbulent Reynolds number were then plotted in a Borghi diagram, which is commonly used when categorizing flame regimes. The HiTAC and CDC flame regimes are characterized by low Damköhler numbers in relation to turbulent Reynolds numbers, as can be seen in the Williams diagram of Figure 2.5. A sufficiently low Damköhler number is achieved by increasing the chemical time scale or lowering the flow time scale. It was found that lowering the oxygen concentration significantly increases flame thickness while reducing the flame speed and thus increases the chemical time scale. However, multiple researchers have also shown that distributed combustion can be achieved solely through air dilution [21, 22] by increasing the air jet mass flow rate. However, pure air dilution lowers the Damköhler number to a smaller extent while also increasing the turbulent Reynolds number, forcing the flame closer to the 'flamelets in eddies' regime as given by Figure 2.5. Therefore, the authors found that controlling oxygen concentration is the most critical parameter to achieving distributed combustion.

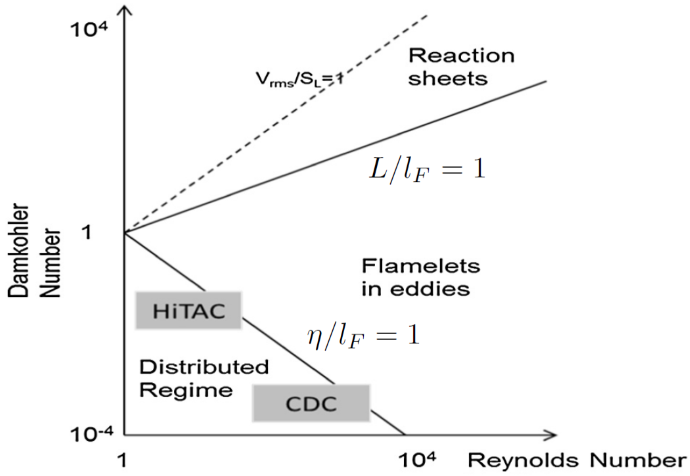

Figure 2.5: Flame regime classification by Damköhler number and turbulent Reynolds number for premixed combustion. Adapted with permission from Khalil and Gupta [10].

2.4 Modeling

2.4.1 Turbulence

In the following sections an introduction to turbulence modeling and specifically the models used in this thesis will be made. For a more detailed approach, the reader is advised to consult Pope [23], upon which the following section is based. The motion of constant property Newtonian fluids (such as air) is governed by the Navier-Stokes equations. They consist of conservation of mass (continuity):

$$\frac{\partial \rho}{\partial t} + \nabla \cdot (\rho \mathbf{U}) = 0 \quad , \tag{2.7}$$

and the three equations for conservation of momentum,

$$\frac{\partial \mathbf{U}}{\partial t} + \mathbf{U} \cdot \nabla \mathbf{U} = -\frac{1}{\rho}\nabla p + \nu \nabla^2 \mathbf{U} \tag{2.8}$$

Due to the random nature of turbulence, various statistical quantities are introduced to describe the turbulent fields. One way to derive equations for the evolution of the turbulent flow field is by decomposing the velocity, $\mathbf{U}(\mathbf{x},t)$ into its mean $\bar{\mathbf{u}}$ and fluctuating parts $\mathbf{u}'$, for which evolution equations can then be derived. This decomposition is known as the Reynolds decomposition. Introducing the mean and fluctuating velocity components and the mean density of a non-constant property fluid into the Navier-Stokes equations ((2.7), (2.8)) and performing a time-averaging of the continuity and momentum equations results in the so called Reynolds Averaged Navier-Stokes (RANS) equations. In tensor format, there are given by

$$\frac{\partial (\bar{\rho}\bar{u}_i)}{\partial x_i} = 0 \quad \text{(i = 1, 2, 3)} \quad , \tag{2.9}$$

for conservation of mass and

$$\bar{\rho}\bar{u}_j \frac{\partial \bar{u}_i}{\partial x_j} = \frac{\partial}{\partial x_j}\left[-\bar{p}\delta_{ij} + \mu\left(\frac{\partial \bar{u}_i}{\partial x_j} + \frac{\partial \bar{u}_j}{\partial x_i}\right) - \bar{\rho}\overline{u_i' u_j'}\right] \quad \text{(i, j = 1, 2, 3)} \quad , \tag{2.10}$$

for conservation of momentum. In equation (2.10), $\bar{\rho}$ is the mean fluid density, $\bar{p}$ is the mean pressure and μ is the fluid kinematic viscosity. The bracketed term can be seen as the sum of three stresses: The isotropic stress $-\bar{p}\delta_{ij}$ that arises from the mean pressure field, the viscous stress $\mu\left(\frac{\partial \bar{u}_i}{\partial x_j}+\frac{\partial \bar{u}_j}{\partial x_i}\right)$ from the mean strain and the apparent stress from the fluctuating velocity field, $\bar{\rho}\overline{u_i'u_j'}$. The latter is referred to as the Reynolds stress tensor, τ_{ij}. Similar to how viscous stresses arise from momentum transfer at the molecular level, the Reynolds stress arises from momentum transfer by velocity fluctuations. For a statistically three-dimensional flow, one is presented with a situation where there are four independent governing equations, these being the three averaged momentum equations and the averaged continuity equation, but more than four unknowns. The mean velocities and pressure constitute four unknowns, unto which the nature of the decomposition and averaging of equations has added six additional unknowns that make up the symmetric Reynolds stress tensor. This is called the closure problem, as the equation system is under-determined. To solve the system, the Reynolds stresses must somehow be modeled. Besides accuracy, robustness and computational cost, such models can be appraised based on their completeness, i.e how well they represent certain physical qualities that must be fulfilled by the Reynolds stress tensor. The most important such quality is realizability, which prevents the turbulence model to generate nonphysical results by imposing the following constraints on tensor components,

$$\overline{u_i^2} \geq 0 \tag{2.11}$$

$$\left|\frac{\overline{u_i u_j}}{\bar{u}_i^2 \bar{u}_j^2}\right| \leq 1 \quad . \tag{2.12}$$

The first condition requires that the normal stresses are all non-negative, an intuitive argument being that any real number squared will be non-negative. The second condition is the Schwarz inequality which has its basis in linear algebra. The realizability condition will appear when describing different turbulence models in the next section.

The most common tubulence models used in industry are turbulent-viscosity models. They rely on the eddy viscosity hypothesis, which is based on the assumption that turbulent eddies transport momentum in the same way that molecules do, analogous to the stress-rate-of-strain constitutive relation for a Newtonian fluid. The hypothesis imposes a linear relation between the Reynolds stress anisotropy $a_{ij}=\overline{u_i'u_j'}-\frac{2}{3}k\delta_{ij}$ and the mean rate of strain, $S_{ij}=\frac{1}{2}\left(\frac{\partial \bar{u}_i}{\partial x_j}+\frac{\partial \bar{u}_j}{\partial x_i}\right)$, such that

$$\overline{u_i'u_j'}-\frac{2}{3}k\delta_{ij}=-\nu_T\left(\frac{\partial \bar{u}_i}{\partial x_j}+\frac{\partial \bar{u}_j}{\partial x_i}\right) \quad \text{or} \quad a_{ij}=-2\nu_T S_{ij} \tag{2.13}$$

where k is the turbulent kinetic energy and ν_T the turbulent viscosity, a model parameter that must be determined. Unfortunately, the eddy viscosity hypothesis is not generally valid and results in poor accuracy for many types of flows. Among those are flows with sudden changes in mean strain-rate, flows over curved surfaces, flows in rotating fluids and three-dimensional flows. The hypothesis assumes that the principal axes of the Reynolds-stress tensor τ_{ij} are coincident with those of the mean strain-rate tensor, scaled by a coefficient of proportionality. Unlike the molecular viscosity, which is a fluid property, the eddy viscosity depends on several flow quantities, such as the shape of solid boundaries, freestream turbulence intensity and flow history, [24]. Despite these deficiencies, two-equation models based on the eddy viscosity hypothesis are used because of their robustness and low computational cost.

In the following sections, terms related to production of turbulent kinetic energy, dissipation rate, specific dissipation and Reynolds stresses due to buoyancy effects have been removed from their respective equations. This is motivated by the fact that body forces are negligible in the present study, on the grounds that viscous forces will be several orders of magnitude larger than buoyancy forces. The relative importance of buoyancy forces in a flow containing both forced and natural convection can be expressed by the Richardson number, as the ratio of the Grashof and Reynolds numbers, [25],

$$Ri = \frac{Gr}{Re^2} = \frac{g\beta\Delta TL}{U^2} \tag{2.14}$$

where $g = 9.81 \quad m/s$ is the gravitational acceleration, β is the coefficient of thermal expansion for the fluid (approximately equal to $1/T$ for ideal gases), ΔT is the difference between wall temperature and bulk fluid temperature, L is the characteristic length and U is the fluid velocity. When the Richardson number approaches unity, the effects of buoyancy become appreciable. In the non-reacting case, Ri is obviously zero as there is no temperature difference. Even in the reacting case, taking $\Delta T = 1000\ K$, $U = 5\ m/s$ (an estimation of the near-wall velocity at the bottom combustor wall from preliminary simulation) and L as the combustor width, $L = 1.75" = 44mm$, the predicted value is $Ri \approx 0.004$. To reach unity, clearly non-physical values of ΔT would be required (the adiabatic flame temperature of methane is roughly 2200 K). Therefore, we may neglect buoyancy in all cases.

$k-\varepsilon$ models

The k-ε model is a two-equation model based on the eddy viscosity hypothesis (2.13), and was originally developed by Jones and Launder [26]. The model solves two separate transport equations for turbulent kinetic energy, k, and dissipation rate, ε, and defines the turbulent viscosity as

$$\nu_T = C_\mu k^2/\varepsilon \quad . \tag{2.15}$$

C_μ is a model constant set to $C_\mu = 0.09$. The exact transport equation for turbulent kinetic energy, k, is

$$\frac{\bar{D}}{\bar{D}t}k + \nabla \cdot \mathbf{T}' = \mathscr{P} - \varepsilon \quad , \tag{2.16}$$

where $\frac{\bar{D}}{\bar{D}t}$ is the material derivative. The energy flux $\mathbf{T}'$ is defined by

$$T_i' = \frac{1}{2}\overline{u_i'u_j'u_j'} + \frac{1}{\rho}\overline{u_i'p'} - 2\nu\overline{u_j's_{ij}} \quad . \tag{2.17}$$

The production of k, $\mathscr{P}$, is given by

$$\mathscr{P}_{ij} = -\overline{u_i'u_j'}\frac{\partial \bar{u}_j}{\partial x_k} - \overline{u_j'u_k'}\frac{\partial \bar{u}_i}{\partial x_k} \tag{2.18}$$

In equation (2.16), $\mathbf{T}'$ and ε both contain unknown quantities, (2.17), which are not solved for in the equations and thus must be modeled. The flux is modeled with a gradient-diffusion hypothesis approach, as

$$\mathbf{T}' = -\frac{\nu_T}{\sigma_k}\nabla k \quad , \tag{2.19}$$

where σ_k is the turbulent Prandtl number for kinetic energy, which is set to $\sigma_k = 1$. Insertion of (2.19) into (2.16), then yields the modeled k equation,

$$\frac{\bar{D}k}{\bar{D}t} = \nabla \cdot \frac{\nu_T}{\sigma_k}\nabla k + \mathscr{P} - \varepsilon \quad . \tag{2.20}$$

An empirically based transport equation for ε is constructed with similarly to the k equation. The dissipation rate equation then has generation and destruction terms which are presumed proportional to the respective quantities in turbulent kinetic energy, divided by large eddy turn-over time, k/ε. The model equation is given by

$$\frac{\overline{D}}{\overline{D}t}\varepsilon = \frac{\partial}{\partial x_j}\left(\frac{\nu_T}{\sigma_\varepsilon}\frac{\partial \varepsilon}{\partial x_j}\right) + C_{\varepsilon 1}\frac{\mathscr{P}\varepsilon}{k} - C_{\varepsilon 2}\frac{\varepsilon^2}{k} \quad , \tag{2.21}$$

where C_μ, $C_{\varepsilon 1}$, $C_{\varepsilon 2}$ and σ_ε are model parameters, given by

$$C_{\varepsilon 1} = 1.44, \quad C_{\varepsilon 2} = 1.92, \quad \sigma_\varepsilon = 1.3 \tag{2.22}$$

The $k - \varepsilon$ model is the simplest complete turbulence model, and has long been the workhorse of industry due to its high robustness, low computational cost and reasonable accuracy. However, while the accuracy for simple flows with low gradients and near straight streamlines can be acceptable, it is known to produce results that can be qualitatively incorrect for more complex flows. These include flows featuring strong gradients of mean strain rate and highly curved streamlines. For example, the quadratic nature of the eddy viscosity hypothesis results in an overprediction of the production of k in highly curved streamlines. In addition, the predicted spreading rate of round jets is known to be poor, which is attributed to the model ε equation.

An attempt to remedy these faults has been proposed by Shih et al., [27], resulting in the realizable $k - \varepsilon$ model. It features a different formulation for the turbulent viscosity and a new formulation for the dissipation rate equation. The new dissipation rate equation was derived by developing a model equation for the dynamic equation of mean-square vorticity fluctuation, $\overline{\omega_i \omega_i}$, which can then be related to dissipation through

$$\varepsilon = \nu \overline{\omega_i \omega_i} \quad , \tag{2.23}$$

in large Reynolds number flows. The revised eddy viscosity model is based on the same relation as the standard $k - \varepsilon$ model, (2.15), although with a variable value of C_μ. This is due to the fact that for a constant value of $C_\mu = 0.09$ as used in the standard formulation, the model becomes non-realizable in cases of large mean strain rate. The normal Reynolds stresses may then become negative and the Schwarz shear stress inequality can be violated. To ensure realizable Reynolds stresses, a variable C_μ must be implemented. In the formulation by Shih et al., [27], C_μ is a function of mean strain rate, mean rotation rate and angular velocity. The realizable model is known to perform better than the standard model in many cases, notably for rotating shear flows and round jets, [27], both of which are relevant to the flow pattern inside the combustor analyzed in this thesis.

$k-\omega$ models

The second most widely used family of two-equation models are the $k-\omega$ models, developed by Wilcox and others. In this model, the rate of dissipation ε equation is replaced by an equation for the specific dissipation $\omega = \varepsilon/k$, while the k equation and expression for μ_T are identical to the $k-\varepsilon$ model. The transport equation for ω is given by

$$\frac{\overline{D}}{\overline{D}t}\omega = \nabla\cdot\left(\frac{\nu_T}{\sigma_\omega}\nabla\omega\right) + C_{\omega 1}\frac{\mathscr{P}\omega}{k} - C_{\omega 2}\omega^2 \quad . \tag{2.24}$$

Because of the relationship between ε and ω, an ω equation can also be derived from the $k-\varepsilon$ model, resulting in

$$\frac{\overline{D}}{\overline{D}t}\omega = \nabla\cdot\left(\frac{\nu_T}{\sigma_\omega}\nabla\omega\right) + (C_{\varepsilon 1}-1)\frac{\mathscr{P}\omega}{k} - (C_{\varepsilon 2}-1)\omega^2 + \frac{2\nu_T}{\sigma_\omega k}\nabla\omega\cdot\nabla k \quad . \tag{2.25}$$

Clearly, the formulation implied by the $k-\varepsilon$ model, (2.25), involves an additional term compared to (2.24). In terms of performance, the $k-\omega$ model is superior in treatment of the viscous near-wall region, which does not require any damping functions and allows for easy setting of boundary conditions and shows greater numerical stability as compared to the standard $k-\varepsilon$ model. It is also superior in accounting from streamwise pressure gradients. The main drawback is the treatment of non-turbulent free-stream boundaries, which requires a non-physical ω boundary condition, to which the predicted flow is highly sensitive. A remedy to this problem was proposed by Menter, [28], by introducing a blending function that results in a hybrid between the $k-\omega$ and $k-\varepsilon$ models. The Baseline (BSL) and Shear-Stress Transport (SST) models are written as a $k-\omega$ model that include the last cross diffusion term in (2.25), multiplied by a blending function. The blending function is zero near the walls, leading to the standard $k-\omega$ formulation, and unity in the free stream, thus adapting a $k-\varepsilon$ formulation. In addition, in the SST model, the turbulent viscosity is modified to better replicate the effects of shear stress transport, which in other two-equation models caused an overprediction of the principal turbulent shear stress $\overline{u'v'}$ in adverse pressure gradients. The result is a numerically stable model that has improved treatment of boundary layers and adverse pressure gradients, without the freestream sensitivity that plagues the standard $k-\omega$ model. Because the flow studied in this thesis features adverse pressure gradients downstream of the inlet air jet, this advantage of the SST $k-\omega$ model could prove useful.

Reynolds-Stress Models

Reynolds stress models (RSM) avoid the defects associated with the eddy viscosity hypothesis by solving model transport equations for individual components of the Reynolds stress tensor and the dissipation ε or specific dissipation ω. These models are also reffered to as second-order closure models. An exact transport equation for the Reynolds stresses can be derived from Navier-Stokes equations and is given below, adapting a combined style of Pope [23] and the ANSYS Theory Guide, [25]:

$$\frac{\overline{D}}{\overline{D}t}\overline{u_i'u_j'} + \frac{\partial}{\partial x_k}T_{kij} = \mathscr{P}_{ij} + \mathscr{R}_{ij} - \varepsilon_{ij} + F_{ij} \quad . \tag{2.26}$$

Because the equation contains terms for convection and diffusion of τ_{ij}, RSM models include effects of flow history, which were missing from the eddy-viscosity models. The convection, production and (optionally) body-force terms ensure a qualitative response to streamline curvature and sudden changes to mean strain-rate. Lastly, the inclusion of the production by system rotation term, $\mathscr{F}_{ij}$, naturally includes the effect of rotation, which is also a deficiency of the two-equation models, [24]. In equation (2.26),

$$T_{kij} = \overline{u'_i u'_j u'_k} + \frac{1}{\bar{\rho}}\overline{u'_i p'}\delta_{jk} - \nu\frac{\partial \overline{u'_i u'_j}}{\partial x_k} \qquad \text{(i, j, k = 1, 2, 3)} \tag{2.27}$$

is the Reynolds stress flux, composed of three terms: Turbulent transport, pressure transport and viscous diffusion. Out of these three, the first two need to be modeled, as they involve quantities that are not among the solved variables. In RSM models, this is done using a gradient diffusion approach, assuming the transport term T_{kij} is proportional to the gradient of velocity fluctuations $\frac{\partial \overline{u_i u_j}}{\partial x_k}$, multiplied with some scaled combination of the known quantities k and ε to achieve the correct dimensions.

The production tensor, $\mathscr{P}_{ij}$, is given by

$$\mathscr{P}_{ij} = -\overline{u'_i u'_j}\frac{\partial \bar{u}_j}{\partial x_k} - \overline{u'_j u'_k}\frac{\partial \bar{u}_i}{\partial x_k} \quad . \tag{2.28}$$

The individual Reynolds stresses are known and thus $\mathscr{P}_{ij}$ does not need to be modeled. The most important quantity to model is the pressure-rate-of-strain tensor, $\mathscr{R}_{ij}$,

$$\mathscr{R}_{ij} = \overline{\frac{p'}{\bar{\rho}}\left(\frac{\partial u_i}{\partial x_j} + \frac{\partial u_j}{\partial x_i}\right)} \quad . \tag{2.29}$$

Because the equation for pressure fluctuations is linear, p' may be decomposed into a rapid, slow and harmonic part, accordingly,

$$p' = p^{(r)} + p^{(s)} + p^{(h)} \quad .$$

The pressure-rate-of-strain tensor may then be decomposed in the same fashion,

$$\mathscr{R}_{ij} = \mathscr{R}^{(r)}_{ij} + \mathscr{R}^{(s)}_{ij} + \mathscr{R}^{(h)}_{ij} \quad . \tag{2.30}$$

The slow pressure-rate-of-strain $R^{(s)}_{ij}$ in (2.30) is modeled on the assumption that turbulence has a natural tendency toward isotropy as it decays. It is calculated through a differential equation for the normalized anisotropy tensor, $b_{ij} = \frac{a_{ij}}{2k}$. The rapid pressure-rate-of-strain $R^{(r)}_{ij}$ is modeled in accordance to Rapid-Distortion Theory, which applies to the evolution of turbulence when $\mathscr{S}k/\varepsilon$ is arbitrarily large ($\mathscr{S} = (2\overline{S_{ij}S_{ij}})^{1/2}$). This yields exact and linear equations for the fluctuating velocity, which may be solved using linear summation of simple Fourier waves.

The last quantity in equation (2.26) is the dissipation tensor,

$$\varepsilon_{ij} = 2\nu\overline{\frac{\partial u_i}{\partial x_k}\frac{\partial u_j}{\partial x_k}} \quad . \tag{2.31}$$

The dissipation tensor needs to be modeled and this is usually done by use of Kolmogorov's hypothesis of local isotropy. Kolmogorov postulated that at sufficiently high Reynolds numbers, the small scale turbulent motions are statistically isotropic. Instead of solving a total of six transport equations, one for each term of the dissipation tensor, only one equation is solved for the isotropic part, ε_{ii}, and the tensor is then modeled as being entirely isotropic by $\varepsilon_{ij} = \frac{2}{3}\varepsilon\delta_{ij}$. For models based on the specific dissipation, the dissipation equation is replaced with a similar treatment, [23]. Lastly, the production by system rotation term, $\mathscr{F}_{ij}$ is given by

$$\mathscr{F}_{ij} = -2\theta_k\left(\overline{u'_j u'_m}e_{ikm} + \overline{u'_i u'_m}e_{jkm}\right) \quad . \tag{2.32}$$

In equation (2.32), θ_k is the rotation vector and e_{ijk} is the cyclic permutation operator. As all terms are known, Ω_{ij} does not need to be modeled. The difference between different RSM models is largely the way the slow pressure-rate-of-strain tensor is modeled. The ideal model fulfills a number of constraints, the specifics of which will be left to the reader to pursue in works such as Pope [23], Wilcox [24] and Speziale, Sarkar, and Gatski [29]. The most basic model available in Fluent is known as the LRR model and was proposed by Launder, Reece, and Rodi, [30]. Here, the pressure-rate-of-strain is modeled in three parts as

$$\mathscr{R}_{ij} = \mathscr{R}^{(s)}_{ij} + \mathscr{R}^{(r)}_{ij} + \mathscr{R}^{(w)}_{ij} \quad , \tag{2.33}$$

where $\mathscr{R}^{(s)}_{ij}$ is the slow pressure-strain or return-to-isotropy term, modeled as

$$\mathscr{R}^{(s)}_{ij} = -C_1\bar{\rho}\frac{\varepsilon}{k}\left(\overline{u'_i u'_j} - \frac{2}{3}k\delta_{ij}\right) \quad . \tag{2.34}$$

The rapid pressure-strain term, $\mathscr{R}^{(r)}_{ij}$, is modeled as

$$\mathscr{R}^{(r)}_{ij} = -C_2\left[\mathscr{P}_{ij} + F_{ij} - \frac{1}{3}(\mathscr{P}_{kk} - \mathscr{C}_{kk})\delta_{ij}\right] \quad , \tag{2.35}$$

where the turbulent convection $\mathscr{C}_{ij}$ is defined as

$$\mathscr{C}_{ij} = \frac{\partial}{\partial x_k}\left(\bar{\rho}\bar{u}_k\overline{u'_i u'_j}\right) \quad . \tag{2.36}$$

Lastly, the wall-reflection term $\mathscr{R}^{(w)}_{ij}$ is given as

$$\begin{aligned} \mathscr{R}^{(w)}_{ij} = {} & C'_1\frac{\varepsilon}{k}\left(\overline{u'_k u'_m}n_k n_m\delta_{ij} - \frac{3}{2}\overline{u'_i u'_k}n_j n_k - \frac{3}{2}\overline{u'_j u'_k}n_i n_k\right)\frac{C_l k^{3/2}}{\varepsilon d} \\ & + C'_2\left(\mathscr{R}^{(r)}_{km}n_k n_m\delta_{ij} - \frac{3}{2}\mathscr{R}^{(r)}_{ik}n_j n_k - \frac{3}{2}\mathscr{R}^{(r)}_{jk}n_i n_k\right) \quad , \end{aligned} \tag{2.37}$$

where n_k is the coordinate component of the wall unit normal and d is the normal distance to the wall. The model constants are given by

$$C_l = C_\mu^{3/4}/\kappa$$

where κ is the Von Karman constant (=0.4187) and

$$C_1 = 1.8, \quad C_2 = 0.6, \quad C'_1 = 0.5, \quad C'_2 = 0.3 \quad ,$$

in the freestream. The wall-reflection term (2.37) is required to produce physical near-wall results by redistributing stress from the direction perpendicular to the wall to the parallell stresses. In addition, Low-Re modifications of the model constants are required when using the enhanced wall treatment option in Fluent. Enhanced wall treatment uses a two-layer model, subdividing the near-wall region into a viscosity-affected part and a fully-turbulent part, and generally produces more accurate results than standard or scaled wall functions employing the law-of-the-wall [25]. The model constants are then given as functions of turbulent Reynolds number, $Re_T = \rho k^2/(\mu\varepsilon)$ and Reynolds stress invariants [25].

Clearly, (2.33) is linear in the anisotropy tensor a_{ij}. Based on this model, Speziale, Sarkar, and Gatski, [29], developed a non-linear model they named the SSG model, which involves a quadratic term in a_{ij}. This model fulfilled a number of additional constraints to ensure physical results, such as consistency with Rapid-Distortion Theory for rotating shear flows and physical experiments on decay of isotropic turbulence and return to isotropy of anisotropic, homogeneous turbulence. The pressure-rate-of-strain is then given by

$$\begin{aligned}\mathscr{R}_{ij} = &-\Big(C_1\bar{\rho}\varepsilon + C_1^*P\Big)b_{ij} + C_2\bar{\rho}\varepsilon\Big(b_{ik}b_{kj} - \frac{1}{3}b_{mn}b_{mn}\delta ij\Big) + \Big(C_3 - C_3^*\sqrt{b_{ij}b_{ij}}\Big)\bar{\rho}kS_{ij} \\ &+ C_4\bar{\rho}k\Big(b_{ik}S_{jk} + b_{jk}S_{ik} - \frac{2}{3}b_{mn}S_{mn}\delta_{ij}\Big) + C_5\bar{\rho}k\Big(b_{ik}\Omega_{jk} + b_{jk}\Omega_{ik}\Big) \quad ,\end{aligned} \tag{2.38}$$

where the mean rate-of-rotation tensor Ω_{ij} is defined by

$$\Omega_{ij} = \frac{1}{2}\left(\frac{\partial u_i}{\partial x_j} - \frac{\partial u_j}{\partial x_i}\right) \quad . \tag{2.39}$$

Here, P represents the half-trace of the production tensor, i.e

$$P = \frac{1}{2}\mathscr{P}_{ii} \quad .$$

The model constants are given by

$$C_1 = 3.4 \quad C_1^* = 1.8 \quad C_2 = 4.2 \quad C_3 = 0.8 \quad C_3^* = 1.3 \quad C_4 = 1.25 \quad C_5 = 0.4 \quad .$$

This model has been shown to produce more accurate results than the LRR model for a range of shear flows including rotating plane shear and plane strain, as well as axisymmetric expansion and contraction. This should imply better performance for a wider class of more complex flows, including those with streamline curvature [29].

Both the LRR and SSG RSM models are based on the ε equation. Similarly to the differences in performance between the two-equation models using ε and ω, greater performance in near-wall boundary layer predictions can be achieved in a RSM model based on the ω equation. This was proposed by Wilcox [24] in the Stress-ω model. Just as with the LRR model, low-Reynolds number corrections had to be included, but viscous damping and wall reflection functions are not required. In Fluent, a stress-BSL model is implemented, which solves a scale equation to remove the freestream sensitivity, similar to that of the BSL and SST $k-\omega$ models. The pressure-rate-of-strain is linear in τ_{ij} and is given by

$$\begin{aligned}\mathscr{R}_{ij} = &-C_1\bar{\rho}\beta^*\omega(\overline{u_i'u_j'} - \frac{2}{3}k\delta_{ij}) - \tilde{\alpha}(\mathscr{P}_{ij} - \frac{1}{3}\mathscr{P}_{kk}\delta_{ij}) \\ &- \tilde{\beta}(\mathscr{D}_{ij} - \frac{1}{3}\mathscr{P}_{kk}\delta_{ij}) - k\tilde{\gamma}(S_{ij} - \frac{1}{3}S_{kk}\delta_{ij}) \quad ,\end{aligned} \tag{2.40}$$

where

$$\mathscr{D}_{ij} = -\overline{u_i' u_m'}\frac{\partial \bar{u_m}}{\partial x_j} - \overline{u_j' u_m'}\frac{\partial \bar{u_m}}{\partial x_i}$$

and the model constants are defined by

$$\beta^* = 0.09\frac{4/15 + (Re_T/8)^4}{1 + (Re_T/8)^4}, \quad Re_T = \frac{\bar{\rho} k}{\mu \omega}$$

and

$$\tilde{\alpha} = \frac{C_2 + 8}{11}, \quad \tilde{\beta} = \frac{8C_2 - 2}{11}, \quad \tilde{\gamma} = \frac{60C_2 + 4}{55} \quad C_1 = 1.8, \quad C_2 = 0.52.$$

2.4.2 Energy and Species Transport

Modeling chemical reactions requires that both the energy equation and individual species transport equations are solved together with the momentum and continuity equations, (2.10) and (2.9). In ANSYS Fluent, turbulent heat transport is modeled analogously to the concept of turbulent momentum transfer and is identical for both two-equation and RSM turbulence models. The unsteady energy equation is given by

$$\frac{\partial}{\partial t}(\bar{\rho} E) + \nabla \cdot \Big[\bar{\mathbf{u}}(\bar{\rho} E + p)\Big] = \nabla \cdot \Big[\kappa_{eff} \nabla T - \sum_k h_k \mathbf{J}_k + \tau_{eff} \cdot \bar{\mathbf{u}}\Big] + S_E \quad . \tag{2.41}$$

For steady state incompressible flow, it reduces to

$$\bar{\rho} \bar{\bar{\mathbf{u}}} \nabla \cdot \Big[(E + \frac{p}{\rho})\Big] = \nabla \cdot \Big[\kappa_{eff} \nabla T - \sum_k h_k \mathbf{J}_k + \tau_{eff} \cdot \bar{\bar{\mathbf{u}}}\Big] + S_E \quad , \tag{2.42}$$

where the right-hand side terms represent energy transfer due to conduction, species diffusion and viscous dissipation, in order of appearance. The last term, S_E, is a source or sink term, representing for example heat of chemical reaction or radiation. The total specific energy E in equations (2.41) and (2.42) for incompressible flow is

$$E = h - \frac{p}{\bar{\rho}} + \frac{\bar{u}^2}{2}$$

and the sensible enthalpy h is the sum of specific enthalpies h_k for each species k. For incompressible flow, it is

$$h = \sum_k Y_k h_k + \frac{p}{\bar{\rho}} \quad ,$$

where Y_k is the mass fraction of the kth species. Energy sources due to chemical reaction are calculated as

$$S_{E,r} = -\sum \frac{h_k^0}{M_k} R_k \quad ,$$

where h_k^0 is the enthalpy of formation, R_k is the volumetric rate of creation and M_k is the molar mass of the kth species. In equations (2.41) and (2.42), κ_{eff} is the effective thermal conductivity. It is modeled as

$$\kappa_{eff} = \kappa + \frac{c_p \nu_T}{Pr_t} \quad , \tag{2.43}$$

where Pr_t is the turbulent Prandtl number, with a default value in Fluent of $Pr_t = 0.85$. Lastly, $(\tau_{ij})_{eff}$ is the deviatoric stress tensor, representing the effects of viscous heating. It is given by

$$(\tau_{ij})_{eff} = \mu_{eff}\Big(S_{ij} - \frac{2}{3}\frac{\partial u_k}{\partial x_k}\delta_{ij}\Big) \quad .$$

The unsteady transport equation for the kth species mass fraction Y_k is given by

$$\frac{\partial}{\partial t}(\bar{\rho} Y_k) + \nabla \cdot (\bar{\rho}\bar{\mathbf{u}} Y_k) = -\nabla \cdot \mathbf{J}_k + S_k \tag{2.44}$$

where $k = 1, 2, ..., K$ for a total of K species. In equation (2.44) , $\mathbf{J}_k$ denotes the diffusive flux and S_k is the chemical source term. In the present case of steady-state incompressible flow, it simplifies to

$$\bar{\rho}\bar{\mathbf{u}} \cdot \nabla Y_k = -\nabla \cdot \mathbf{J}_k + S_k \quad . \tag{2.45}$$

The diffusive flux, $\mathbf{J}_k$, arises due to gradients of temperature and concentration. It is modeled by use of Fick's law, which allows it to be calculated as

$$\mathbf{J}_k = -\Big(\rho D_{k,m} + \frac{\nu_T}{Sc_t}\Big)\nabla Y_k - D_{T,k}\frac{\nabla T}{T}$$

where $D_{k,m}$ is the mass diffusion coefficient of species k in the mixture m, Sc_t is the turbulent Schmidt number (with a default value of 0.7) and $D_{T,k}$ is the thermal diffusion coefficient of species k. When using volumetric reactions in ANSYS Fluent, the chemical source term is calculated by an exterior software named Chemkin. The chemical source term is then given the rate of production $\dot{\omega}_k$ of the kth species as a summation of rate-of-progress variables for all reactions that include this particular species:

$$\dot{\omega}_k = \sum_{i=1}^{I} \nu_{ki} q_k \tag{2.46}$$

where

$$\nu_{ki} = \nu'_{ki} - \nu''_{ki} \quad .$$

Here, ν'_{ki} are the forward stoichiometric coefficients and ν''_{ki} are the reverse stoichiometric coefficients for a reaction written in the general form,

$$\sum_{k=1}^{N} \nu'_{ki}\mathcal{X}_k \Longleftrightarrow \sum_{k=1}^{N} \nu''_{ki}\mathcal{X}_k \quad ,$$

where $\mathcal{X}_k$ is the chemical symbol of the kth species. The rate of progress q_i for the ith reaction is the difference of the forward and reverse reaction rates. The rate of an elementary reaction is proportional to the concentration of each species involved raised to the power its stoichiometric coefficient:

$$q_{i,elem} = k_{fi}\prod_{k=1}^{N}[\mathcal{X}_k]^{\nu'_{ki}} - k_{ri}\prod_{k=1}^{N}[\mathcal{X}_k]^{\nu''_{ki}} \quad . \tag{2.47}$$

In equation (2.47), $[\mathscr{X}_k]$ indicates the molar concentration of the kth species. Elementary reactions are featured in the detailed GRI 3.0 mechanism to be discussed later. For global mechanisms, the reaction order is not necessarily equal to the stoichiometric coefficient. q_i is then given by the following expression,

$$q_{i,global} = k_{fi} \prod_{k=1}^{N} [\mathscr{X}_k]^{F_{ki}} - k_{ri} \prod_{k=1}^{N} [\mathscr{X}_k]^{R_{ki}} \quad , \tag{2.48}$$

where the forward and reverse reaction orders, F_{ki} and R_{ki}, can be arbitrary real numbers generated from fitting experimental data. The Jones-Lindstedt and Westbrook-Dryer mechanisms are both global mechanisms and will be presented in the concluding part of the theory section. The rate constants k_{fi} and k_{ri} can be described by different relations, although the most common and indeed the one to be used later on in this study is a general Arrhenius expression:

$$k_{fi/ri} = A_i T^{\beta_i} e^{-\frac{E_i}{RT}} \quad , \tag{2.49}$$

where the pre-exponential factor A_i, the temperature exponent β_i and the activation energy E_i are specified in the forward direction for irreversible reactions and both forward and backward directions for reversible reactions. During the solution procedure, the chemical source term is integrated over a time step Δt to yield the change in composition. Because this involves integration of every reaction rate in every cell, the process is computationally expensive.

2.4.3 Combustion

Because of the fundamental physical and chemical differences of the CDC regime in comparison to conventional regimes, one must be careful when trying to model this behaviour. The Damköhler number has been shown to approach unity in general cases. This implies that the process is governed by turbulence-chemistry interactions as opposed to molecular transport [10]. Therefore the simulation must include models that accurately describe both chemical reactions and turbulent mixing. This causes some turbulent combustion models relying on the so called 'fast chemistry' assumption (those based on the flamelet concept) to be unsuitable [31] and therefore finite rate chemistry models must be employed. The general consensus in literature ([31, 32]) seems to be that RANS modeling coupled with the Eddy Dissipation Concept (EDC) by Magnussen [33] results in the best performance in terms of accuracy and computational cost. However, it should be noted that downsides of RANS modeling for combustion are the lack of inclusion of unsteady mixing or stirring effects. LES simulation per definition includes these effects but is restricted to the use of only a handful of scalar transport equations due to the computational expense. This means that one instead has to sacrifice detailed chemistry, something that could play an important role in CDC simulation.

The Eddy Dissipation Concept

The EDC model by Magnussen [33] is a turbulent reacting flow model that has found widespread use in industry and research because of its inclusion of detailed chemical kinetics at a relatively low computational cost when compared to more complex models. Moreover, the regular model can be used with In-Situ Adaptive Tabulation (ISAT) or Dynamic Cell Clustering (DCC) to further increase this advantage [25]. ISAT dynamically stores the result of performed direct integrations of chemical reactions in an adaptive table. When subsequent cells are updated, the table is queried for the specific state of the current cell. If an integration from a state similar to the current one has already been performed, it can then be tabulated "on the fly" within a certain error tolerance, instead of performing the computationally direct integration again. This ensures that integration between two exact states is only performed once during a simulation. ISAT is known to reduce the chemistry computation time by as much as two or three orders of magnitude [25], which makes it essential when using the EDC model with detailed reaction mechanisms and fine grids. DCC is a mapping algorithm which clusters cells with similar states of temperature and equivalence ratio, within a specified range. One integration is then performed for every cluster, as opposed to every cell, and the updated states are then mapped back to each cell [25].

The EDC model is based on the concept of chemical reactions taking place in intermittent isolated regions of small volume, so called fine structures, such as thin vortex tubes and sheets or ribbons of vorticity. The characteristic dimensions of the fine structures are comparable to those of the Kolmogorov microscale. The fine structures act as a well-stirred reactor, assumed to be adiabatic and isobaric with homogeneously mixed reactants. They are also the place where turbulence is dissipated into heat [33]. The physical quantities describing the fine structures are mass fraction in relation to the total fluid mass, γ_λ and mean residence time of fluid within the structures, $\tau *$. These quantities are determined by an energy cascade model according to

$$\begin{aligned} \gamma_\lambda &= \left(\frac{3C_{D2}}{4C_{D1}^2}\right)^{1/4}\left(\frac{\nu\varepsilon}{k^2}\right)^{1/4} = C_\gamma\left(\frac{\nu\varepsilon}{k^2}\right)^{1/4} \\ \tau^* &= \left(\frac{C_{D2}}{3}\right)^{1/2}\left(\frac{\nu}{\varepsilon}\right)^{1/2} = C_\tau\left(\frac{\nu}{\varepsilon}\right)^{1/2} \quad , \end{aligned} \tag{2.50}$$

where ν is the kinematic viscosity and ε is the dissipation rate of turbulent kinetic energy k. In the original model, C_{D1} was calculated using the assumption that for a Reynolds number much larger than unity, dissipation in the largest eddies is negligible. C_{D2} was empirically determined to fit a range of flows. The constants were set to 0.135 and 0.5 respectively, giving C_γ=2.1377 and $C_\tau = 0.4083$. [32]. The source term in the transport equation of the kth species (2.45) is calculated as

$$S_k = \frac{\bar{\rho}(\gamma_\lambda)^2}{\tau^*\left[1-(\gamma_\lambda)^3\right]}\left(Y_k^* - Y_k\right) \quad , \tag{2.51}$$

where Y_k^* is the fine-scale species mass fraction after reacting according to equation (2.46) over time τ^*. The energy cascade model is based on the transfer rate of mechanical energy, first from mean flow to the largest turbulent eddies and from there into successively smaller eddies which are described by 'levels' in the model. The eddy strain rate $\omega_n = u_n/Ln$ at level n is defined by the level characteristic velocity u_n and length L_n and is assumed to double for each level, i.e $\omega_{n+1} = 2\omega_n$. The last level is described by scales on the same order of magnitude as the Kolmogorov scales [33]. The original cascade model was developed with a clear separation between the scales at which mechanical energy is introduced to the turbulence and the scales where reactions take place. However, in the CDC regime no such clear separation can be made, as the reactions take place in a much wider range of scales than that of traditional combustion. This fundamental error can be (partly) remedied by revision of the cascade model [32].

Modified EDC

In a recent study of MILD combustion on the so called Delft Jet in Hot Co-flow burner, it was shown that although the standard EDC model accurately described the mean velocity profiles there were systematic deviations between the measured and predicted temperature fields [34]. This was attributed to an over-prediction of the mean reaction rate. The parameters of the EDC model were determined for high Reynolds number flows and fast chemistry. The standard values are therefore, not surprisingly, better fitted to the conventional combustion regimes than to CDC, which by definition is characterized by slower reactions. The authors then noted that performance could be improved by changing these parameters to $C_\gamma = 1.0$ and $C_\tau = 3.0$, or $C_\gamma = 2.1377$ and $C_\tau = 3.0$. This was later confirmed using the same burner by Evans, Medwell, and Tian [35]. Parente et al. [32] revisited the energy cascade concept of the EDC model to identify the relationship between the parameters and the specific flow and reaction characteristics related to MILD combustion or CDC, quantified by the Reynolds and Damköhler numbers. By choosing the characteristic speed of the reacting fine structures as the turbulent flame speed S_T and using dimensional analysis, they found that the two major parameters were related in the following way

$$C_\tau \propto 1/(Da_\eta^2(Re_T+1)) \qquad C_\gamma \propto Da_\eta^{1/2}(Re_T+1)^{1/2} \tag{2.52}$$

where Da_η is the Damköhler number evaluated at the Kolmogorov scale and Re_T being the turbulent Reynolds number. For low Damköhler numbers, the fine structure time coefficient C_τ should be larger than for traditional combustion regimes, accounting for larger reaction regions, smaller driving forces due to smooth gradients and lower temperatures due to dilution of reactants. The fine structure coefficient C_γ should be decreased because distribution of the fine structures would result in them having a lower local mass fraction. Both of these arguments are in line with the changes proposed by Evans, Medwell, and Tian [35]. The authors then proposed an extension to the EDC model, where values of Da_η and Re_T were calculated for each cell allowing calculation of local model coefficients C_τ and C_γ using user-defined functions in ANSYS Fluent.

Mixture fraction model

While the (modified) EDC model has been chosen to generate the final results in this study, a simpler mixture fraction model was also used. The inclusion of volumetric reactions is computationally expensive in comparison to a mixture fraction model. It is therefore recommended in the Fluent manual [25] to generate initial temperature, density and species fields using the latter before activating the former. This increases the robustness and rate of convergence of the simulation by providing a sound "starting guess". The basis of modeling non-premixed combustion by the mixture fraction approach is a number of simplifying assumptions that allows the thermochemical state to be determined by a single conserved scalar quantity, namely the mixture fraction Z. Among these assumptions are that the Lewis number is unity, i.e diffusion coefficients for all species and enthalpy are equal and that fuel and oxidizer enter the domain through discrete, separate inlets. The mixture fraction is defined as the local ratio of mass flux originating from the fuel stream to the sum of mass fluxes from the oxidizer and fuel streams, i.e

$$Z = \frac{\dot{m}_{fuel}}{\dot{m}_{fuel} + \dot{m}_{air}} \quad . \tag{2.53}$$

From equation (2.53), we then have that $Z = 1$ in the inlet fuel stream and $Z = 0$ in the inlet air stream. Assuming equal diffusivities D for all species, the species transport equations can be reduced to a single transport equation governing the mixture fraction, [17]

$$\bar{\rho}\frac{\partial Z}{\partial t} + \bar{\rho}\tilde{\mathbf{u}}\cdot\nabla Z = \nabla\cdot(\bar{\rho}D\nabla Z) \quad , \tag{2.54}$$

where $\tilde{\mathbf{u}}$ is the Favre-averaged mean velocity vector. Besides considerably reducing the number of scalar equations, this approach also features no chemical source term (because all element mass fractions are conserved), meaning no reaction rates have to be integrated during the solution procedure. The steady-state implementation of equation (2.54) in Fluent is divided into two equations: One for the Favre (density) averaged mixture fraction $\overline{Z}$, (2.55) and one for the mixture fraction variance $\overline{Z'^2}$, (2.56):

$$\bar{\rho}\bar{\tilde{\mathbf{u}}}\cdot\nabla\overline{Z} = \nabla\cdot\left[\left(\frac{k}{c_p} + \frac{\nu_T}{\sigma_T}\right)\nabla\overline{Z}\right] \tag{2.55}$$

and

$$\bar{\rho}\tilde{\mathbf{u}}\cdot\nabla\overline{Z'^2} = \nabla\cdot\left[\left(\frac{k}{c_p} + \frac{\nu_T}{\sigma_T}\right)\nabla\overline{Z'^2}\right] + C_g\nu_T\cdot(\nabla\overline{Z})^2 - C_d\bar{\rho}\frac{\varepsilon}{k}\overline{Z'^2} \quad , \tag{2.56}$$

where c_p is the mixture specific heat capacity. C_g and C_d are model constants set to 2.86 and 2.0, respectively. Different approaches are available to model the turbulence chemistry interaction based on the mixture fraction. In this study, the steady diffusion flamelet (SDF) model was used, which models the turbulent flame as a number of steady laminar flames (i.e diffusion flamelets). The flamelets are then ensembled into a turbulent flame structure using statistical PDF methods. This allows the preprocessing of 'look-up' tables for thermodynamic properties before starting a simulation, resulting in large computational savings. However, the flame is assumed to respond immediately to aerodynamic strain and thus cannot model strong non-equilibrium effects such as ignition and NO_x chemistry [25].

Reaction mechanisms

The last piece needed to assemble a full simulation model is a chemical reaction mechanism. While the combustion model provides the format to solve chemical reactions, the relevant species and their reactions must be supplied. Because combustion can involve hundreds or thousands of different reactions and species, a compromise must be made between the level of detail in the simulated chemistry and computational cost. In this thesis, three different mechanisms were used: The GRI 3.0 mechanism, a modified Jones-Lindstedt 4-step mechanism and a modified Westbrook-Dryer 3-step mechanism.

GRI 3.0 is an optimized mechanism for modeling of natural gas combustion, written by Smith et al. [36] of University of California, Berkley on behalf of the Gas Research Institute. It contains 325 reactions and 53 different species, making it a detailed and rather computationally heavy mechanism. For this reason the included reactions are confined to Appendix D, as they encompass several pages. GRI 3.0 also features a library of all related thermodynamic and transport properties based on NASA polynomials. They are appended in Appendix D. The mechanism is well used in both academia and industry and its quality has been proven in numerous studies. A clear advantage is that it naturally includes pollutant formation through NO formation and reburn chemistry by inclusion of reactions 13 through 20, unlike the less detailed mechanisms.

The Jones-Lindstedt mechanism (hereby referred to as JL) is a global 4-step mechanism for methane-air combustion originally developed by Jones and Lindstedt [37]. The mechanism includes oxidation of CH_4 and H_2 as well as two intermediate steps,

$$
\begin{aligned}
CH_4 + 0.5\,O_2 &\longrightarrow CO + 2\,H_2 && \{25\}\\
CH_4 + 2\,H_2O &\longrightarrow CO + 3\,H_2 && \{26\}\\
CO + H_2O &\rightleftharpoons CO_2 + H_2 && \{27\}\\
H_2 + 0.5\,O_2 &\rightleftharpoons H_2O \quad \cdot && \{28\}
\end{aligned}
$$

Due to the lower partial pressure of oxygen present during CDC conditions, a modification was proposed by Marinov, Westbrook, and Pitz [38] to adjust the reaction rate parameters governing the oxidation of H_2 into H_2O in reaction 28. The modification was verified by Wang et al. [39] and Kim, Schnell, and Scheffknecht [40] to produce temperature and species fields better fit to experimental data for CDC or MILD combustion of methane. The modified mechanism will be referred to as JL2.

The simplest mechanism used in this study was a modified version of the 3-step Westbrook-Dryer mechanism, hereby referred to as WD. It was first published by Westbrook and Dryer [41] in 1981. Wang et al. proposed a modification of the original Westbrook-Dryer mechanism by using the same reaction rate parameters for H_2 oxidation as in the JL mechanism. This modified mechanism will be called WD2. The WD mechanisms are based on three reactions governing the oxidation of CH_4, CO and H_2,

$$
\begin{aligned}
CH_4 + 1.5\,O_2 &\longrightarrow CO + {}_2H_2O && \{29\}\\
CO + 0.5\,O_2 &\rightleftharpoons CO_2 && \{30\}\\
H_2 + 0.5\,O_2 &\rightleftharpoons H_2O \quad \cdot && \{31\}
\end{aligned}
$$

As neither the WD or the JL reactions include NO_x chemistry, they require use of separate pollutant models in Fluent. These simulate NO formation as decoupled from the main combustion process, [25]. Because influence on combustion chemistry and flow field from the NO related species are removed this is expected to reduce accuracy.

The reaction rate parameters, including the modification proposed to the JL and WD mechanisms are presented in Appendix B. The GRI 3.0 mechanism was available online in Chemkin format on a website hosted by the authors and could therefore be downloaded and imported straight into Fluent. However, the JL and WD mechanisms were not available and had to be implemented as Chemkin mechanisms before they could be used in simulations. The written reaction mechanism files can be found in Appendix B. Because all species found in the global mechanisms are also present in GRI 3.0, the published GRI thermodynamics and transport databases could be used for the global mechanisms as well.

2.4.4 NOx

When using the global reaction mechanisms, NO_x formation can calculated in a manner that is decoupled from the other species fields. In Fluent, this is done by solving a transport equation for the NO_x species,

$$\frac{\partial}{\partial t}(\rho Y_{NO}) + \nabla \cdot (\rho \bar{\mathbf{u}} Y_{NO}) = -\nabla \cdot (\rho D \nabla Y_{NO}) + S_{NO} \quad . \tag{2.57}$$

In equation (2.57), the source term is the sum of NO_x formation rates through whichever routes are chosen to be included, in this case thermal, prompt and intermediate N_2O. Thermal NO_x rates are calculated by evaluating Arrhenius rate expressions corresponding to reactions 13 - 15. When the O radical and OH are not present among the resolved species, they are calculated through a partial equilibrium approach. The partial equilibrium approach approximates O concentration by an algebraic expression including O_2 concentration and temperature T. For OH, the expression is based on O, OH and T. Prompt NO_x rates are calculated by relating the formation rate directly to an algebraic expression fit to experimental data as function of Θ, T, p and the concentrations of O_2, N_2 and hydrocarbons. Lastly, NO_x generated through the N_2O path is modeled by calculating rate coefficients of reactions 16 and 17. Concentration of the O radical is here calculated by assuming dissociation of O_2. [25] Rate expressions for the thermal, prompt and N_2O NO_x models can be found in Appendix C.

2.4.5 Radiation

At high temperatures, the effect of radiative heat transfer becomes appreciable in relation to convective and conductive heat transfer processes. Therefore, it becomes important to include radiation in modeling of combusting flows to accurately predict the temperature field and, as NO_x chemistry is particularly temperature sensitive, also the pollutant emissions. Several pages could be dedicated to the subject of radiation theory and modeling but for the sake of brevity only a short introduction will be made. The transmission of radiation intensity I for an absorbing, emitting and scattering medium is described by the radiative transfer equation,

$$\frac{dI(\bar{r},\bar{s})}{d\bar{s}} + (a+\sigma_s)I(\bar{r},\bar{s}) = an^2\frac{\sigma T^4}{\pi} + \frac{\sigma_s}{4\pi}\int_0^{4\pi} I(\bar{r},\bar{s})\Phi(\bar{s}\cdot\bar{s}')d\Omega' \quad , \tag{2.58}$$

where

$\bar{r}$ = position vector
s = path length
n = refractive index
σ = Stefan-Boltzmann constant
T = local temperature
Ω' = solid angle .

$\bar{s}$ = direction vector
a = absorption coefficient
σ_s = scattering coefficient
I = radiation intensity
Φ = phase function

Discrete Ordinates Model

The discrete ordinates (DO) model solves equation (2.58) for a finite number of solid angles Ω' associated with matching direction vectors $\bar{s}$. This means that the number of added transport equations are equal to the number of solid angles or directions. The radiative transfer equation in each direction is solved as a transport equation, completely analogous to flow, species and energy equations presented earlier. For a gray medium (i.e emissivity is approximated as constant over wavelength) it is given by [25]

$$\nabla \cdot \left[I(\bar{r},\bar{s})\bar{s} \right] + (a+\sigma_s)I(\bar{r},\bar{s}) = an^2 \frac{\sigma T^4}{\pi} + \frac{\sigma_s}{4\pi} \int_0^{4\pi} I(\bar{r},\bar{s})\Phi(\bar{s}\cdot\bar{s}')d\Omega' \quad . \tag{2.59}$$

However, the gray gas model is a considerable oversimplification. In reality, the emissivity is dependent both on temperature, wavelength and local composition of the medium. However, non-gray models were deemed to complicated to be used in this study. The last part of solving for radiative heat transfer is the determination of absorption coefficients. The weighted sum of gray gases model (WSGGM) is a popular way to compute absorption coefficients in combusting flows. It lies somewhere between the oversimplified grey gas model and a complete model (which takes into account particular absorption bands) in terms of accuracy versus computational cost. The basic assumption is that total emissivity over a distance s are related through

$$\varepsilon = \sum_{i=0}^{I} a_{\varepsilon,i}(T)\left(1 - e^{-\kappa_i p s}\right) \quad , \tag{2.60}$$

where $a_{\varepsilon,i}$ are emissivity weighting factors for the ith gray gas, κ_i is the absorption coefficient for the ith gray gas and p is the sum of partial pressures of all gases considered in the WSGGM [25].

2.5 Gathering of experimental data

Experimental results were gathered for various setups on an experimental combustor in the University of Maryland Combustion Laboratory. All experiments except wall temperature measurements were performed by graduate student Joe Feser of University of Maryland. Experiments were conducted using particle image velocimetry (PIV), chemiluminescence, gas analysis and thermocouple measurements. The available PIV equipment did not include thermography cameras, which meant that temperature fields could not be extracted. The lack of a PLIF (planar laser-induced fluorescence) system also meant that species distributions could not be extracted. Validation of simulation results was therefore restricted to comparisons of velocity field, OH chemiluminescence and exhaust temperature and species composition. As the focus of this thesis is on simulation only a brief description of the experimental methods will be given.

The laboratory combustor is shown in figure 2.6, together with the associated pipes. It features two inlets, for air and for fuel, respectively, and one outlet in a reversed flow configuration. The fluid volume is visible through the quartz glass in the center of the iron frame. It has a simple geometry consisting of a rectangular box with two edge fillets and one symmetry plane. The dimensions of the computational domain are depicted in figure 2.7 below.

2.5.1 Particle Image Velocimetry (PIV) and Chemiluminescence

A schematic of the experimental arrangement used for PIV and chemiluminescence is depicted in figure 2.8. The main piece of equipment was a 527 nm ND:YLF laser, firing double pulses at 3kHz with a pulse width of 110 ns and a pulse separation of 11 μs. The first pulse fired at an energy of 5.5 mJ and the second at 5.8 mJ. The air jet was seeded with 3 μm diameter Al_2O_3 particles. Images were captured using a high-speed CMOS camera with a resolution of 1056x650 pixels and a pixel size of 16x16 μm. The camera was

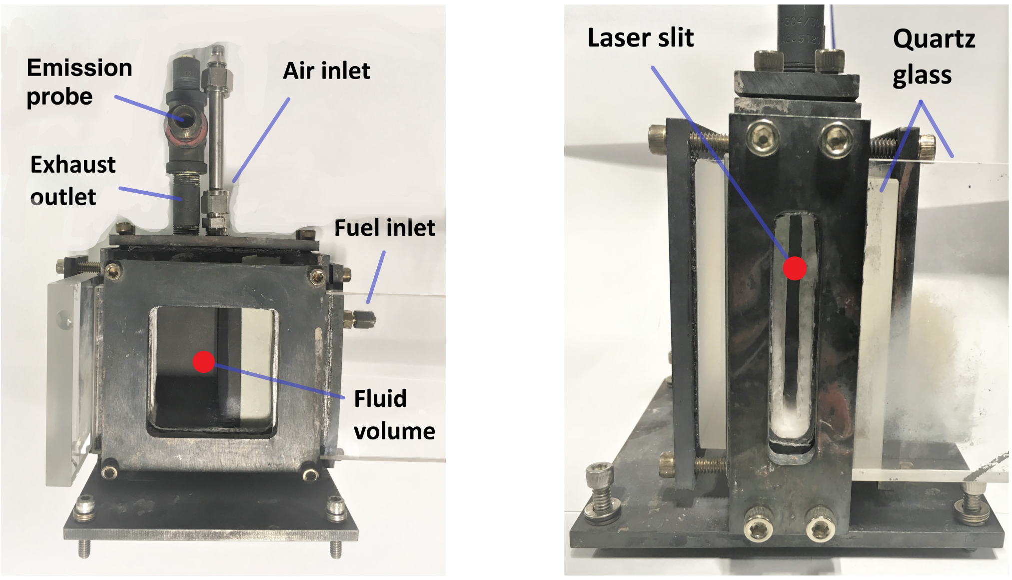

Figure 2.6: Images showing the front plane (left) and the side plane (right) of the laboratory combustor.

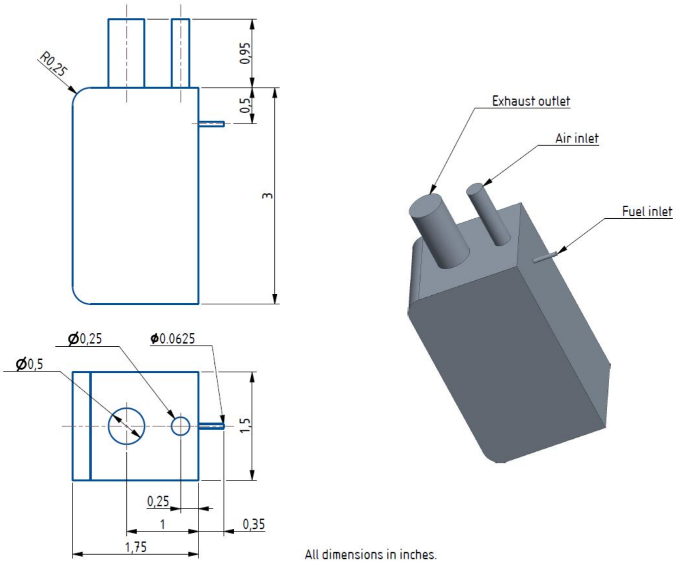

Figure 2.7: Combustor dimensions.

placed with a distance of 400 mm between the lens and the combustor symmetry plane. The camera captured 3000 image pairs over the course of one second with an exposure time of 5 μs. A 50 mm lens was used with a f-stop value of 1.8. Use of an aperture speed booster then lowered the effective f-stop value to 1.6. Particle velocity correlation was performed using 24x24 pixel interrogation windows at 60x80 nodes. PIV allowed capturing of the two-dimensional instantaneous velocity field in the combustor symmetry plane as well as velocity fluctuations which were used to calculate components of the Reynolds stress tensor and approximate the three-dimensional turbulent kinetic energy.

Instantaneous contours of OH^* radicals in the reacting flow were captured by chemiluminescence using nearly the same setup. While the laser settings were the same as for the PIV measurements, the CMOS camera was exchanged for an ICCD camera placed at a distance of 990 mm from the combustor. The ICCD camera had a resolution of 236x375

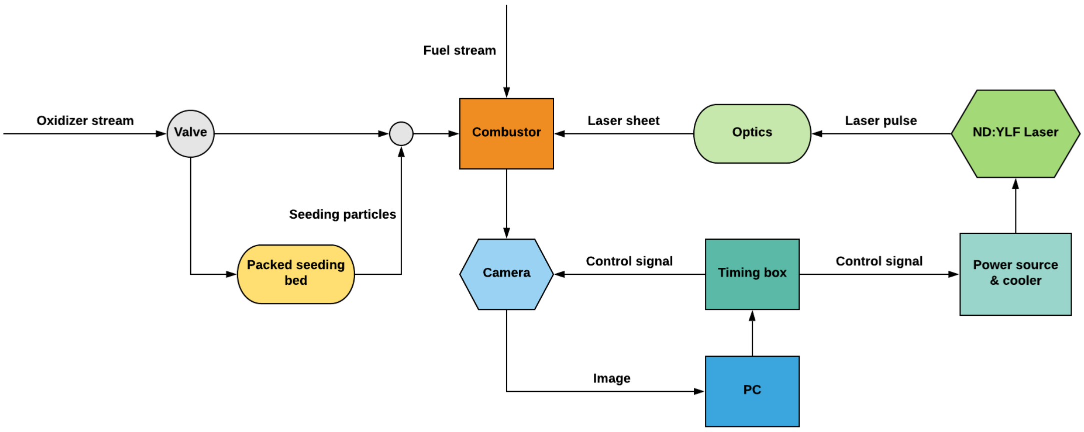

Figure 2.8: Experimental setup for PIV and chemiluminescence.

pixels after cropping and captured images using an exposure time of 50ms. It was fitted with a 105 mm UV lens with a f-stop value of 4.5 and a 307 nm filter with a bandwidth of ± 5 nm. The OH^* intensities were averaged over 10 images for each case studied.

2.5.2 Temperature and exhaust composition measurements

The experimental setup used for temperature and or emissions measurements is depicted in figure 2.9. Compressor air (composition 21% O_2, 0.35% CO_2, 78% N_2 by moles) and pure N_2, CO_2 and CH_4 were fed to separate mass flow controllers. The mass flow controllers were connected to a desktop computer controlling the separate flow rates. From the mass flow controllers, the CH_4 line was connected to the fuel inlet pipe. The compressor air, CO_2 and N_2 lines were connected to a junction, mixing the components before connecting to the air inlet pipe. The uncertainty of mass flow controller flow rates are shown for each stream in Table 2.1.

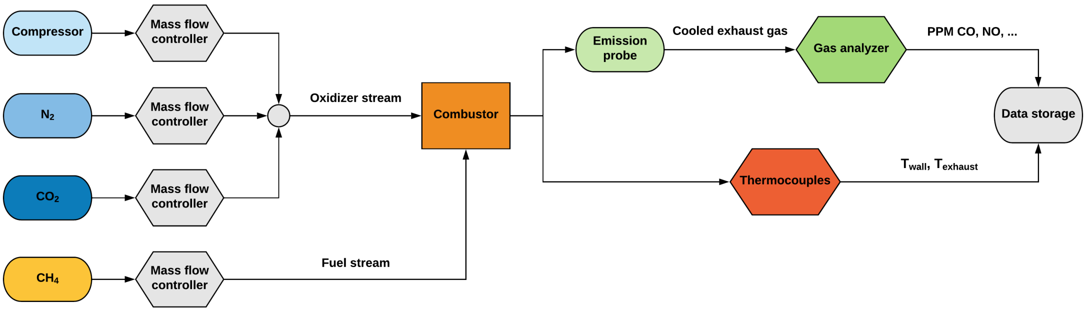

Figure 2.9: Experimental setup to measure temperature and emission levels.

Stream	Fuel	Air	CO_2	N_2
Uncertainty [%]	2.8	2.6	6.7	5.7
Type	Gravimetric	Laminar	Gravimetric	Laminar

Table 2.1: Mass flow controller types and uncertainties.

Near-wall and outlet temperatures

Thermocouples were used to capture the near-wall temperature and the outlet temperature of the reacting flow. For the near-wall measurements, twelve type K thermocouples were placed equidistantly on the inside of one half of the combustor domain, corresponding to the computational domain. Four thermocouples were placed on the "back" wall. Two were placed on each vertical side wall and two on the top and bottom horizontal walls, respectively. The arrangement is depicted in Figure 2.10. The combustor was started as a standard diffusion flame at 21 mol-% O_2. The oxygen level was then lowered incrementally by diluting the air with gradually increasing levels of CO_2 and *chN*2. The readings were started once 15.5 mol-% O_2 had been achieved (further reducing the O_2 concentration led to flame instabilities and eventually extinction just below 15 mol-%). The experiment was terminated once the measured temperatures were approximately constant.

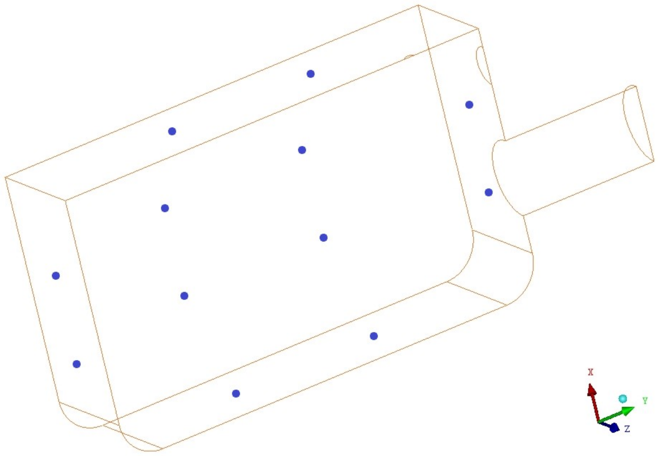

Figure 2.10: Thermocouple placements for near-wall temperature measurements.

The gathered data was processed in MATLAB. The last ten data points for each thermocouple were averaged to yield an estimation of the temperature distribution of the combustor walls. Taking the average of the resulting twelve temperature points then gave an approximation of the mean wall temperature which was used as boundary conditions for reacting flow simulations.

When measuring the outlet temperatures, four thermocouples were used, arranged in a circumferential pattern at roughly half of the pipe radius and 1 inch downstream from the combustor exit, to match the exhaust outlet plane in the simulations. The oxygen level was lowered in the same manner and temperature readings were taken until they leveled off. The flow rates used to achieve 15.5 mol-% O_2 are shown in Table 2.2. The thermal intensity was 25 MW/m^{3}atm, the equivalence ratio was 0.9 and both oxidizer and fuel were at room temperature (roughly 20 °C).

Stream	Air	CH_4	N_2	CO_2
flow rates [l/min]	56.22	5.31	20.24	2.25

Table 2.2: Fuel, air and diluent flow ratess at 15.5 mol-% O_2.

Exhaust composition

Emissions of O_2, CO_2, NO and CO were measured using an emission probe connected to a gas analyzer. The emission probe consisted of a stainless steel pipe with a coaxial water jacket to cool the combustion products and halt further chemical reactions. The probe was mounted at a junction in the exhaust pipe two inches downstream of the combustor exit. The junction can be seen in Figure 2.6. From the probe, gas flowed through a dessicant of $CaSO_4$ crystals followed by a pump and then into the gas analyzer. In the gas analyzer, levels of CO and CO_2 were measured using the NDIR method. NO and O_2 levels were measured using the chemiluminescence and Zirconia cell methods, respectively. The repeatability of these species are shown in Table 2.3.

Species	O_2	CO_2	NO	CO
Repeatability	0.125 vol-%	0.150 vol-%	0.125 ppm	50 ppm

Table 2.3: Gas analyzer repeatability

3

Computational set-up

3.1 Computational domain

When generating the computational domain the symmetry of the combustor allowed modeling of only half of the geometry, reducing the number of elements for a given mesh sizing.

3.1.1 Initial mesh generation

Meshes were generated in ANSYS ICEM CFD, a powerful software package which allows the creation of high resolution grids in an environment that allows a high degree of user manipulation. Initially, when constructing the mesh for the premixed case, it was deemed to difficult to generate a fully structured mesh. The different approaches that are generally used to create mesh for circular and rectangular geometries, respectively, caused problems with the mesh not following the geometry where the pipes join the combustor. Therefore, a hybrid meshing approach was chosen, where structured hexahedral meshes were generated separately for the inlet and outlet pipe and the bottom part of the rectangular combustor. Because it is not possible to merge structured meshes in ICEM CFD, the structured parts had to be merged together by an unstructured tetrahedral section that covered the upper part of the combustor and 0.1 inch of the pipes. The result can be seen in Figure 3.1 and 3.2 (left). The very first such attempt did not include the exhaust outlet pipe in order to reduce the number of elements. However, the strong recirculation zone inside the combustor caused recirculating flow to occur also at the outlet boundary, which resulted in convergence issues when running simulations. Adding a .5 inch length of the outlet pipe did not suffice, and .75 inch was enough to not yield recirculation at the boundary for the realizable $k-\varepsilon$ model but not for the SST $k-\omega$ model. Finally, adding .95 inch of the outlet pipe allowed the flow to settle before reaching the boundary for both models.

Boundary inflation layers were created with an initial layer height of 0.1 mm for the main combustor walls and 0.05 mm for the inlet and outlet pipe. The structured parts were merged to the unstructured part by a layer of pyramid elements so that the interface surface mesh consisted of quadratic elements on both sides. This allowed a conformal transition from hexahedral to tetrahedral elements. A cut-out of the resulting mesh containing hexahedral, tetrahedral, prism and pyramid elements is seen in figure 3.1.

Continuous wall inflation layers were created by generating prism layers in the unstructured mesh while forcing the prism generation algorithm to match the existing quad

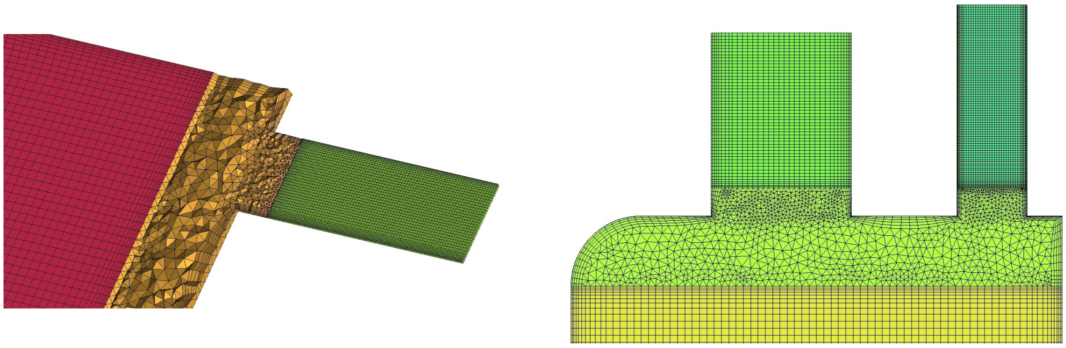

Figure 3.1: Cut-out plane of conformal hybrid mesh showing the air inlet-combustor joint (left) and the symmetry plane (right).

surface mesh. This produced adequate results in most of the domain, except at the upper corners, where the algorithm could not construct five layers from the quadratic surface mesh. This region also contained the elements with the worst quality. The resulting prism and pyramid layers, as well as the final volume mesh, are shown in figure 3.2.

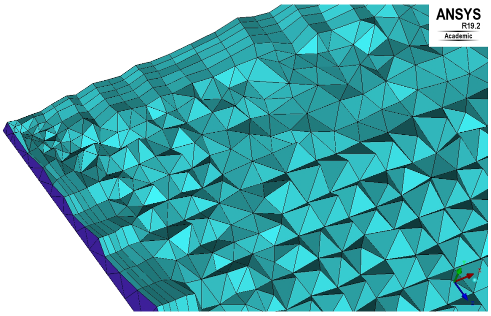

Figure 3.2: Pyramid layer generated after merging of tetrahedral section to hexahedral combustor mesh

While the hybrid approach produced adequate results for the premixed case using the realizable $k-\varepsilon$ and SSG RSM models, there were severe convergence issues when using any of the ω based models. Moreover, when making the next set of meshes to be used in the non-premixed cases, it was not possible to generate a conformal hybrid mesh. Adding the fuel inlet pipe increased the difficulty in generating matching prism layers, for which the boundary nodes would not merge with the structured parts without critical errors. After several days of tinkering with different settings and parameters, the hybrid meshing approach was abandoned.

3.1.2 Structured mesh generation

Fortunately, experience gained in making the structured part meshes allowed the construction of a full structured mesh, including both combustor and pipes. When setting up a structured hexahedral mesh in ICEM CFD, the geometry is first divided into so called "blocks". Blocks are cuboids associated with the geometry within which they are confined. A distribution of nodes are then specified along every edge of each block, which allows careful tailoring of refinement in boundary layers, for example. For irregular geometries, such as the combustor studied, a rather complex blocking strategy may need to be developed in order to create a mesh of good quality. Because of this it generally takes longer time to generate a structured mesh than an unstructured one, although the quality may be improved. In this case, the time spent generating the structured mesh was much lesser than that spent on the hybrid mesh and the resulting quality was clearly superior. While the inclusion of the air and fuel inlet pipes would be possible by adopting a similar strategy as for the exhaust outlet, a better solution was found. Because the inlets are naturally upstream of the combustor, and because no recirculation were taking place inside inlet pipes, it was not necessary to include the piping in the simulation. By removing the pipes, the number of elements would decrease and element sizing due to boundary layer first cell height would not be necessary. The pipe flows could then be simulated in a standalone fashion. The resulting velocity and turbulence quantities at the combustor entry were exported as a profile file to be read as boundary conditions for the combustor simulation. The blocking strategy for the combustor, sans inlet pipes, was as follows.

Combustor

The domain was first divided into rectangular cuboid blocks so that the inlets and outlet were each represented by one such block. Because all blocks in the domain must be divided at each instance to preserve nodal distributions, the fuel inlet consisted of one block, while the air inlet had two and the exhaust outlet three. The resulting blocking is shown in figure 3.3.

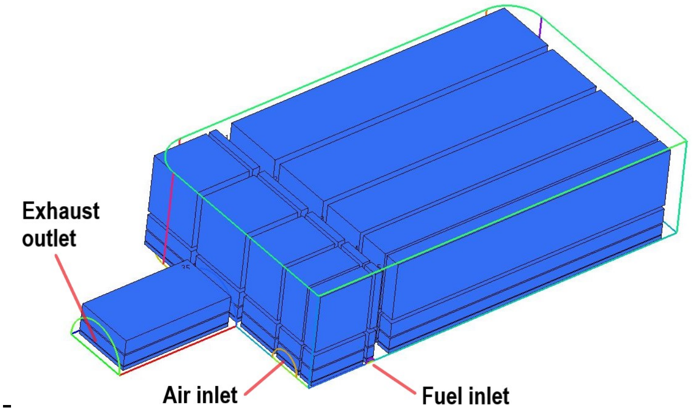

Figure 3.3: Initial rectangular combustor blocking.

Next, all blocks were associated to their bounding geometry. To allow boundary layer inflation near the combustor walls, one more division was made at a distance of 0.125 inch for each wall. The first layer height was set to 0.1 mm with a layer growth factor of 1.2. Then, the blocks containing the rounded edges had to be edited. Representing a circle sector geometry with a rectangular block results in highly skewed mesh. However, the quality can be much improved by converting the rectangular block into a prism and then splitting the prism into three cuboids. This was done by merging boundary nodes and then using the "convert to Y-mesh" tool in ICEM CFD. The blocking is depicted in figure 3.4. At this point, it was possible to generate a pre-mesh to ensure that the blocking was correct, which is seen in figure 3.4.

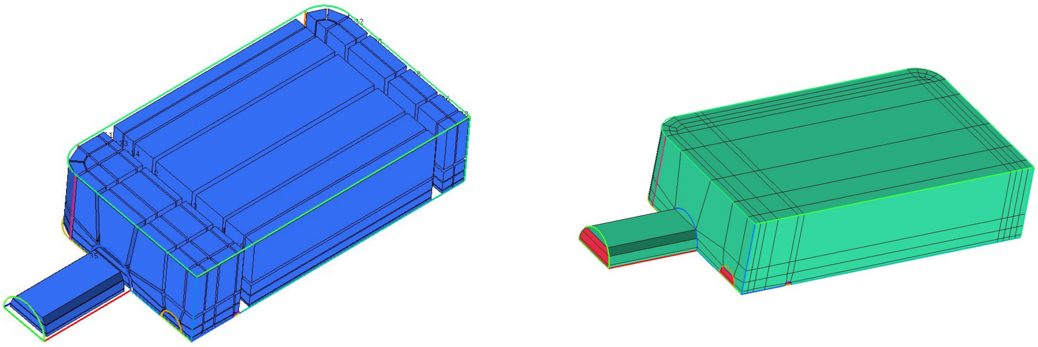

Figure 3.4: Blocking after wall boundary inflation and Y-blocks (left) and pre-mesh (right).

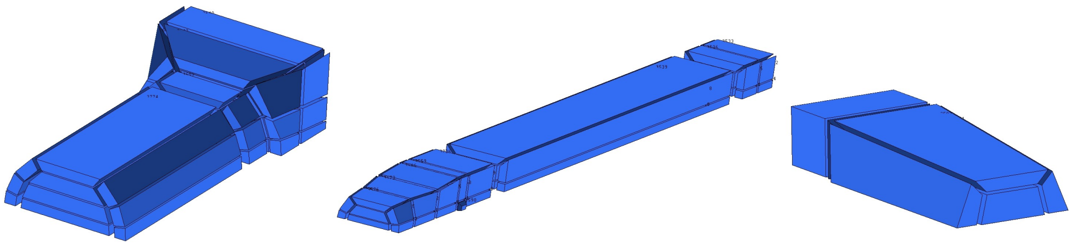

Exhaust outlet **Air inlet** **Fuel inlet**

Figure 3.5: Exhaust outlet blocking (left), air inlet blocking (center) and fuel inlet blocking (right).

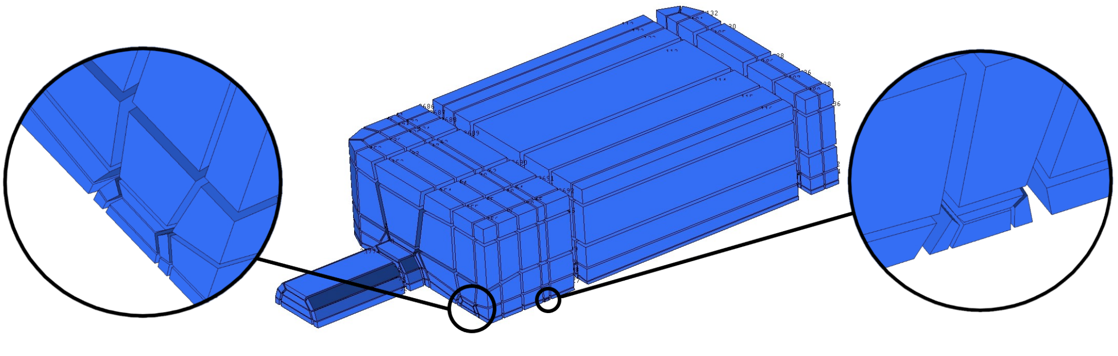

Figure 3.6: Final, full combustor blocking.

Similar to the highly skewed elements at the rounded combustor edges, the half-circle geometries of the inlets and outlet required special attention. In ICEM CFD, cylindrical block quality is improved by generating an internal o-grid, which divides the block into several sub-blocks. For the exhaust outlet, the o-grid allows prescription of boundary layer inflation near the pipe wall. Based on earlier simulations on the hybrid mesh, the first layer height was set to 0.05 mm and the growth factor to 1.2. The outermost element layer would be significantly thinner than the element size perpendicular to the exhaust pipe where the pipe joins the combustor. To avoid an extreme jump in element size, an external o-grid was added at the pipe joint. This allowed specification of nodal spacing to ensure a smoother transition in element size. The exhaust outlet blocking can be seen in figure 3.5. Similarly, because the exhaust pipe joins a wall, the element size parallel to the flow direction had to gradually diminish close to the joint.

The air and fuel inlets also necessitated the use of an internal o-grid in order to yield acceptable mesh quality. While the exhaust pipe o-grid was terminated at the pipe-combustor joint, the air inlet o-grid was allowed to run the entire length of the combustor, as can be seen in figure 3.5. This allowed the o-grid blocks to be used to refine the mesh in the inlet jet area, where high gradients had been observed from the previous simulations. As no pipe wall boundary layer inflation had to be created, no external o-grid was needed. The fuel inlet o-grid can be seen in figure 3.6 and found a natural stop where it connected with the air inlet o-grid. After generating the first mesh, certain nodal distributions were given special attention to minimize the maximum volume change between elements and their neighbors. High volume changes were generally found at the interface between o-grid blocks and regular blocks. The final block structure is depicted in figure 3.6.

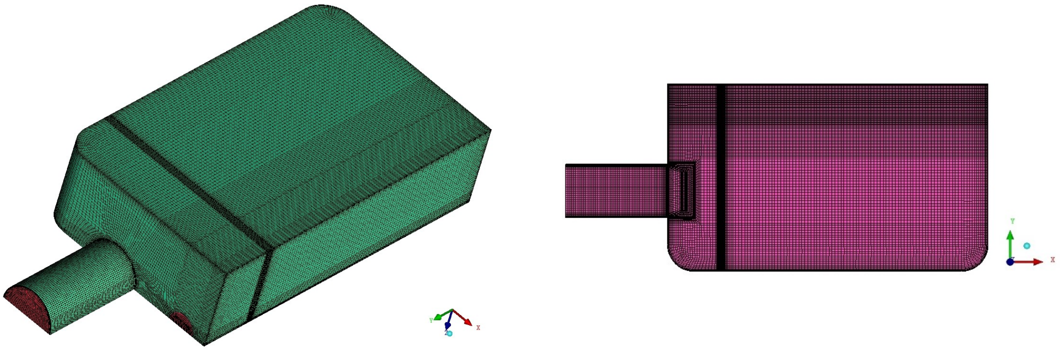

Figure 3.7: Isoparametric view (left) symmetry plane view (right) of the final structured mesh.

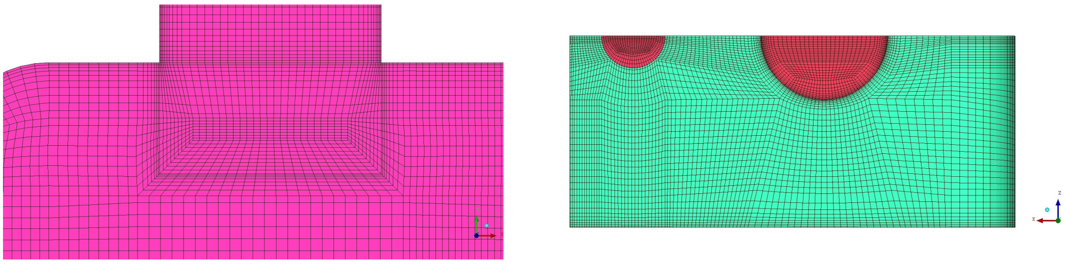

Figure 3.8: Exhaust outlet joint mesh (left) and exhaust outlet and air inlet o-grid mesh (right).

The final mesh that was chosen for further simulation after the mesh dependency (see section 3.2) is depicted in figure 3.7. It featured 830 000 elements with an average side length of 0.028 inches. It was refined further in the area of the air and fuel inlets to better resolve high gradients present in the shear layers. The success of the external o-grid in producing a smooth element size transition at the exhaust pipe joint is shown in figure 3.8. The internal o-grid of the exhaust outlet and air inlet can also be seen in figure 3.8.

Some of the most important mesh quality metrics for this mesh are shown in Table 3.1 below, where they are compared to a hybrid mesh with a similar number of elements. In the table, every metric of the structured mesh is seen to be a considerable improvement over the hybrid mesh, with the overall minimum quality increasing from 0.21 to 0.59.

	Max. Aspect ratio	Min. Skew	Max. Vol. change	Min. Quality
Hybrid	28	0.23	12	0.21
Structured	13	0.42	2.9	0.59

Table 3.1: Mesh quality metrics for hybrid and structured meshes

Air and fuel inlets

Meshes were created separately for the air and fuel inlets. As geometry and o-grid blocking had already been set up for the generation of such meshes used in the hybrid approach, those were reused. Wall boundary layer inflation was set up with a first layer height of 0.05 mm and a growth factor of 1.2. The air inlet pipe was 5 inches and the fuel inlet pipe 6 inches in length, according to measurements of the pipe lengths between the combustor and 90 °bends present upstream. The hydrodynamic entrance length predicted by equation (3.1) which were 1.2 inches for the fuel inlet and 5.5 inches for the air inlet. Both meshes were made to have approximately 200 000 elements and can be seen in figure

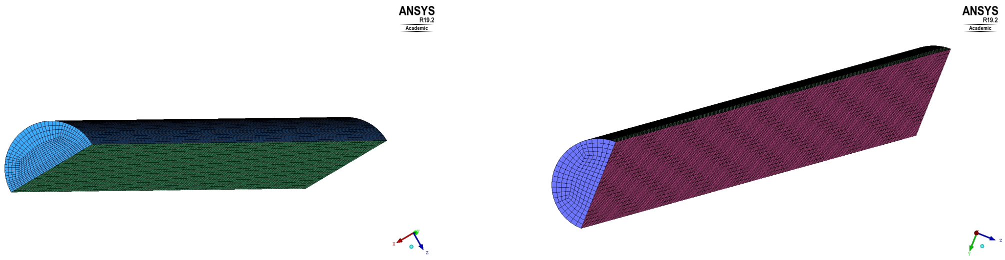

Figure 3.9: Air inlet pipe mesh (left) and fuel inlet pipe mesh (right).

3.9. The nodal distributions were made to match those of of the inlets in the combustor mesh in order to reduce interpolation error when importing the boundary profiles, as will be described later. The mass flowrate interpolation errors were found to be 0.1 % and 0.4 % for the air and fuel inlets, respectively. This was an order of magnitude lower than a previous attempt which used a finer, non-conforming nodal distribution in the pipes. Although said attempt did a better job of resolving the profiles, this did not translate onto the coarser mesh at the combustor inlets, and had a maximum error of 3%, which was deemed unacceptable.

$$L_h = 4.4 \cdot D(Re)^{1/6} \tag{3.1}$$

3.1.3 Generation of boundary condition profiles

Before starting the mesh dependency study, inlet boundary profiles had to be generated through simulation of the air and fuel pipes. Simulations were run in Fluent using the meshes mentioned previously. To yield the most accurate results possible, the BSL RSM turbulence model was used and species transport and the energy equation were enabled. Third order MUSCL scheme discretization was used for all variables except pressure, for which only 2nd order was available in the current version of Fluent. The convergence criterion set required the relative continuity residual to be less than 10^{-7} and all other residuals to be less than 10^{-9}. The outlet boundary condition was set to pressure outlet. The inlet boundary conditions were set to velocity inlet, with a uniform velocity distribution equivalent to a volumetric flow rate previously measured by flow rate controllers in the experimental setup of 76.56 l/minute and 2.07 l/minute for the air and fuel inlet, respectively. Turbulence boundary conditions were set by specifying turbulence intensity and hydraulic diameter. The turbulence intensities were set based on a correlation for fully developed turbulent pipe flow. The relation provided by Russo and Basse [42] relates turbulence intensity I in a smooth pipe to the Reynolds number Re_D by the following formula,

$$I = 0.227 \cdot Re_D^{-0.1} \quad . \tag{3.2}$$

Equation (3.2) predicts turbulence intensities of 8.6% for the air inlet. For the fuel inlet, predicted intensities were 5.2% and 10.8% for CH_4 and CO_2, respectively. Setting both the air inlet and CO_2 intensities to 10% in the pipe simulations thus seemed a reasonable approximation. The CH_4 intensity was set to 5%. Boundary condition values for the non-reacting case are presented in table 3.2 and values for the reacting cases are found in Table 3.3.

	Q [l/min]	V [m/s]	I [%]	T [K]	mole-%
Air inlet	76.56	40.29	10	293	15 O_2, 2.86 CO_2, 82.15 N_2
Fuel inlet	2.07	17.43	10	293	100 CO_2

Table 3.2: Pipe inlet simulation boundary conditions for non-reacting flow.

	Q [l/min]	V [m/s]	I [%]	T [K]	mole-%
Air inlet	76.56	40.08	10	293	15.5 O_2, 2.62 CO_2, 81.9 N_2
Fuel inlet	5.31	44.75	5	293	100 CH_4

Table 3.3: Pipe inlet simulation boundary conditions for reacting flow.
$\phi = 0.9$, $TI = 25MW/m^3 \cdot atm$.

The evolution of velocity magnitude, turbulent kinetic energy and turbulent dissipation rate for the air inlet and fuel inlet using CH_4 is shown in figure 3.10. The CH_4 profiles see little change during the last ten pipe diameters before the outlet and can be considered fully developed. However, the air profiles reach a stable value just about two diameters before the exit, and it is possible that having a longer pipe would see a different result. However, the profiles do resemble results presented in [42], and as the experimental setup had a 90 °bend just upstream of the domain chosen for the simulation, discrepancies because of this are likely to be larger.

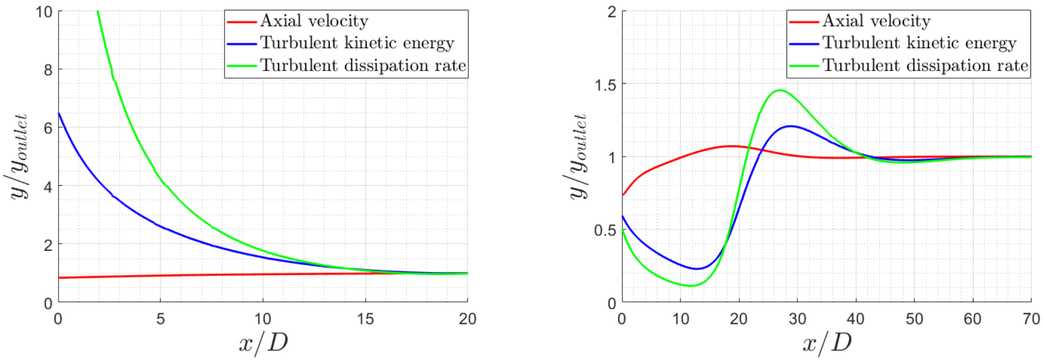

Figure 3.10: Evolution of velocity magnitude and turbulent kinetic energy of the air inlet pipe (left) and fuel inlet pipe (right).

Because of dissipation and production in the pipe, the average turbulence intensity level at the outlet, which would later become the combustor inlet level, had changed considerably. For the air inlet pipe, the mean turbulence intensity had reduced from 10% to 6.1%, while for the fuel inlet pipe, it had increased from 5% to 8.7 %. Scaling relations were used to deal with this issue and be able to specify a level directly as opposed to increasing the inlet level in the pipe calculation to reach a specified value at the exit. Profile files containing velocity and turbulence quantities for each node at the pipe outlets were extracted from Fluent. The turbulence kinetic energy, dissipation rate and specific dissipation rate were then scaled by the ratio of wanted combustor inlet mean turbulence intensity, I_c, and the simulated pipe mean outlet turbulence intensity, I_p, based on the following relations,

$$\begin{aligned} k &= \frac{3}{2}(UI)^2 \\ \varepsilon &= C_v \frac{k^{3/2}}{l^2} \\ \omega &= \frac{\varepsilon}{kC_v} \quad . \end{aligned} \tag{3.3}$$

Rearranging then provides the scaling relations,

$$\begin{aligned} \frac{k_c}{k_p} &= (\frac{I_c}{I_p})^2 \\ \frac{\varepsilon_c}{\varepsilon_p} &= (\frac{I_p}{I_c})^3 \\ \frac{\omega_c}{\omega_p} &= \frac{I_p}{I_c} \quad , \end{aligned} \tag{3.4}$$

which were used to prepare the boundary condition profile files in a MATLAB script. The script is presented in Appendix E. These profiles were then imported and used for inlet velocity and turbulence boundary conditions in the combustor simulations. The resulting profiles are presented in figures 3.11 - 3.13.

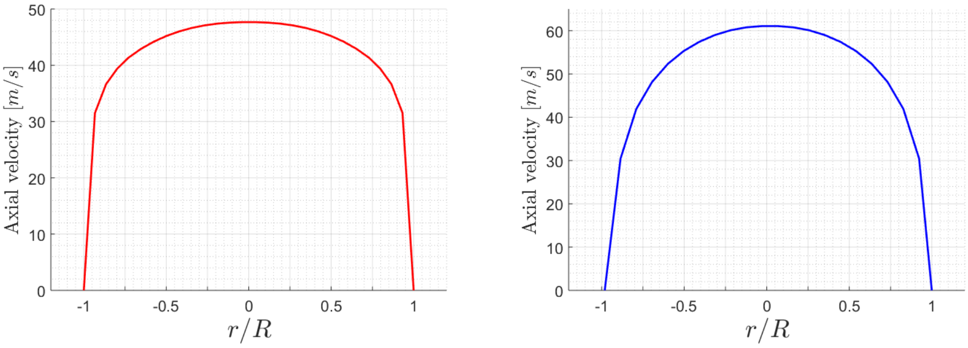

Figure 3.11: Axial velocity boundary profile for the air inlet (left) and fuel inlet using CH_4 (right).

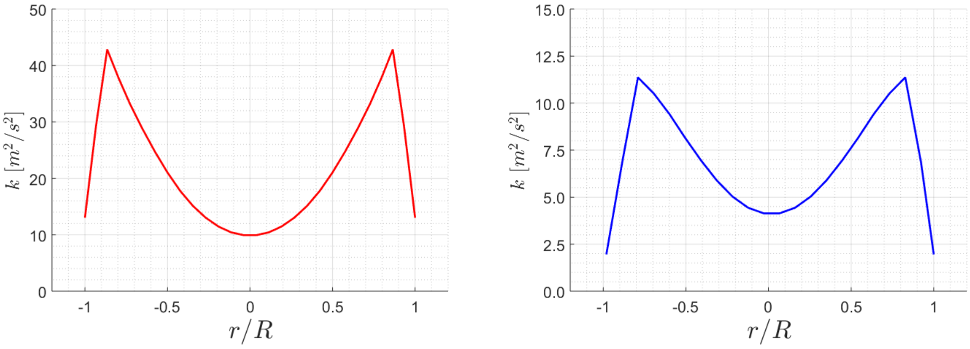

Figure 3.12: Turbulent kinetic energy boundary profile for the air inlet (left) and fuel inlet using CH_4 (right).

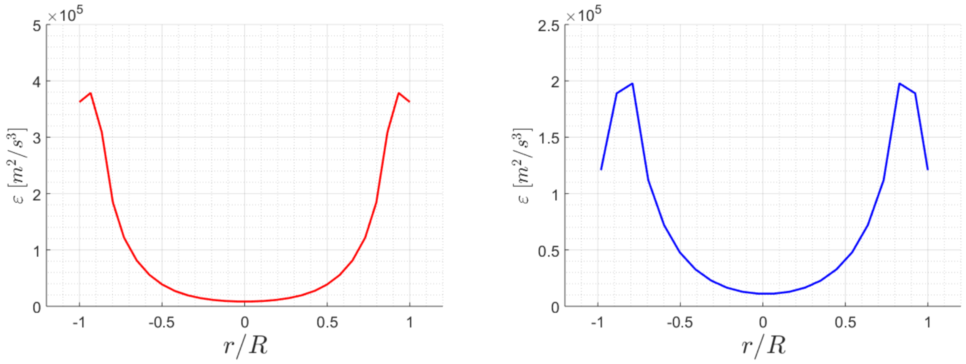

Figure 3.13: Turbulent dissipation rate boundary profile for the air inlet (left) and fuel inlet using CH_4 (right).

3.2 Mesh dependency study

In ANSYS Fluent, the computational domain is discretized according to the finite volumes approach, where the fluid volume is divided into a finite number of control volumes or elements. The governing equations in differential form may then be integrated over each such volume and variations of variables of interest may be approximated using interpolation between neighboring volumes. The result is then a number of algebraic equations which are solved numerically. However, representation of the governing equations as algebraic equations in a discrete domain of space and time inevitably introduces numerical errors, also called discretization errors. A numerical method will approach the solution to the governing equations acting on a continuum domain as the number of grid points increase, i.e the discretization error tends to zero. Because the discretization error reduces with increasing number of elements, in general the solution is expected to differ if comparison is made between two meshes of different element sizing. Therefore, it is common practice to conduct a mesh dependency study, where the variation of the solution with respect to grid size (or number of elements used) is investigated. The goal is to find an acceptable trade-off between accuracy and sizing. Increasing accuracy is, of course, always a desirable trait, but must be weighed against the increased computational cost of having more elements. Because numerical simulation feature multiple error sources besides the discretization error, a point may be found when the order of magnitude of the discretization error is smaller than other errors, such as the modeling error. Further refinement of the grid will then yield little or no increase in accuracy.

3.2.1 Setup

The mesh dependency study was conducted by running simulations on three initial meshes where the number of elements was increased roughly by a factor two for each step, ranging from 380000 to 1530000. Four additional meshes with 240 000, 540 000, 1050 000 and 2500000 elements were then added to yield additonal data points. The incompressible RANS equations were solved using the PISO (Pressure-Implicit with Splitting of Operators) algorithm. The PISO algorithm is in most regards identical to the SIMPLE algorithm, but features an additional predictor step. It has been shown to have robust convergence behaviour while requiring less computational effort than the SIMPLE family of algorithms for flows with weak or no coupling between momentum and scalar equations [43]. Turbulence was modeled using the realizable k-ε model with enhanced wall

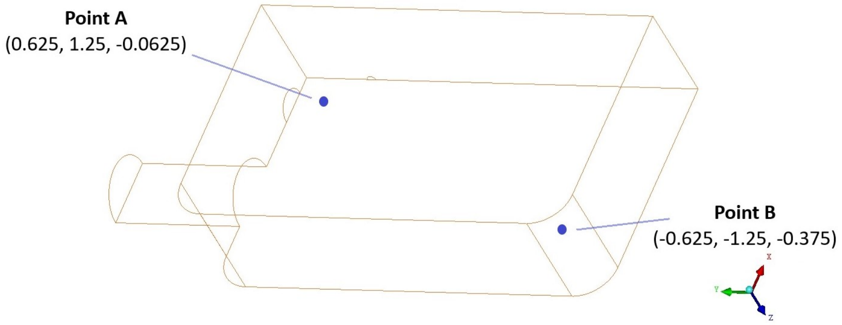

Figure 3.14: Placement of monitor points. Coordinates are given in inches.

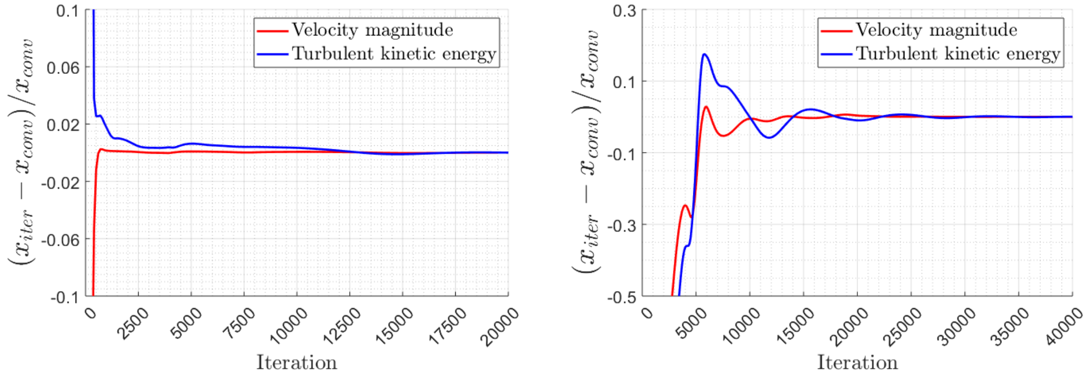

Figure 3.15: Evolution of velocity magnitude and turbulent kinetic energy at monitor point A (left) and point B (right) for the 760 000 element mesh, shown as relative deviation from converged values.

treatment. The energy equation and species transport for O_2, CO_2 and N_2 were enabled. Second order upwind discretization was used for all variables, with the motivation that the added accuracy of third order discretization was not needed and would increase computational time. Under-relaxation factors of 0.2 were used for pressure and momentum, while leaving the other factors at the default values. Inlet boundary conditions were imported from the profiles described in section 3.1.3 and Table 3.2, with pure CO_2 as fuel, and interpolated to the nodal coordinates using the built-in least-squares method in Fluent. Convergence was declared when the relative continuity residual had reduced to below 10^{-5} and all other relative residuals below 10^{-6}. In addition, the velocity magnitude and turbulent kinetic energy was monitored at two different points to ensure that their values were constant over the last thousand iterations. One point (A) was set in a high velocity region near the inlet jet, slightly offset to the symmetry plane. The second point (B) was set in a low velocity region, closer to the back wall. The placements are indicated in figure 3.14.

By the time the residuals had reduced below the prescribed values, the levels of velocity magnitude and turbulent kinetic energy had reached a steady value. In the high velocity region, (point A), the consecutive maximum deviation from the final value was less than 0.1% after only 2000 iterations for velocity magnitude and 12 000 iterations for turbulent kinetic energy. In the low velocity region (point B), it took about 20 000 and 30 000 iterations to reach the same levels for velocity magnitude and turbulent kinetic energy, respectively. Evolution of these monitors are shown in figure 3.15, here represented by results form the coarsest mesh, although all meshes showed similar behaviours.

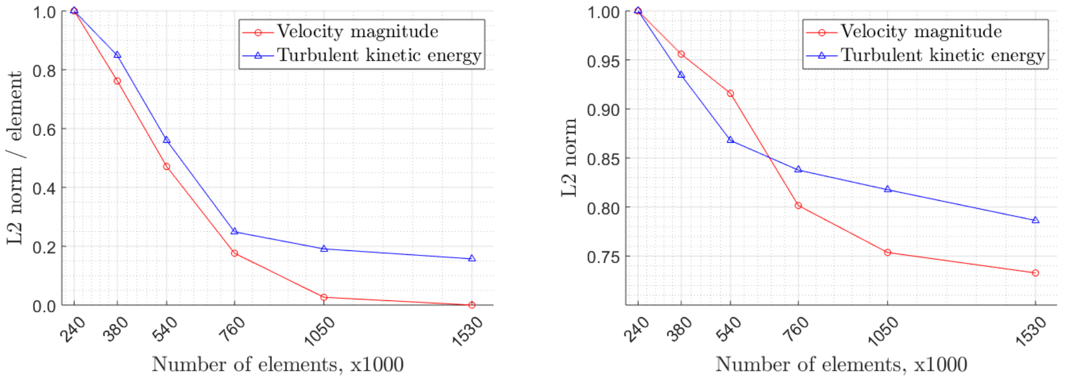

Figure 3.16: Gradient of solution with respect to number of elements scaled by maximum value (left) and absolute difference with respect to finest mesh scaled by maximum value (right) .

The differences in solution between meshes were evaluated by extracting all nodal values of velocity magnitude and turbulent kinetic energy. Because nodal coordinates inevitably vary between meshes, the fields were interpolated at specified coordinates to be comparable. This was done through in MATLAB using linear interpolation at 60x100x25 (=150 000) equally spaced points along the combustor width, height and depth, respectively. Scalar values representing the change in solution was found by calculating the L2 (least squares) norm of difference in velocity or turbulent kinetic energy between a mesh and the next, finer mesh, and between a mesh and the finest mesh, respectively. The values relative to the next mesh were then normalized by the difference in number of elements. The resulting scalars represents the local gradient in solution per additional element added and the absolute error in relation to the "true" solution, represented by the finest mesh. The results are shown in figure 3.16, where the level of solution improvement per additional cell added is seen to level off after the 760 000 element mesh for both velocity magnitude and turbulent kinetic energy.

The 4th mesh, containing roughly 760 000 elements, was chosen for further use in the study. Besides showing the relationship between grid size and solution, some additional observations could also be made. A contour plot of the first node y^+ value is seen in figure 3.17. It shows a maximum of $y^+ = 8$, present at the back wall close to the bottom of the combustor, with high values also being present at the exhaust pipe joint. In most of the domain, the y^+ value was found to be well below 5. The most problematic range is the buffer layer, defined by $5 < y^+ < 30$, where neither the linear relations for the viscous sub-layer nor the log-law for the fully turbulent region are accurate. Because nearly the entire domain were in the viscous sub-layer, further refinement was deemed unnecessary. However, high gradients were present in the shear layers near the inlet jets. In some cases, these led to extremely high turbulent viscosity ratios which resulted in convergence issues. Therefore, the mesh was refined in this area to better resolve the flow field, resulting in a final mesh with a total of 830 000 elements.

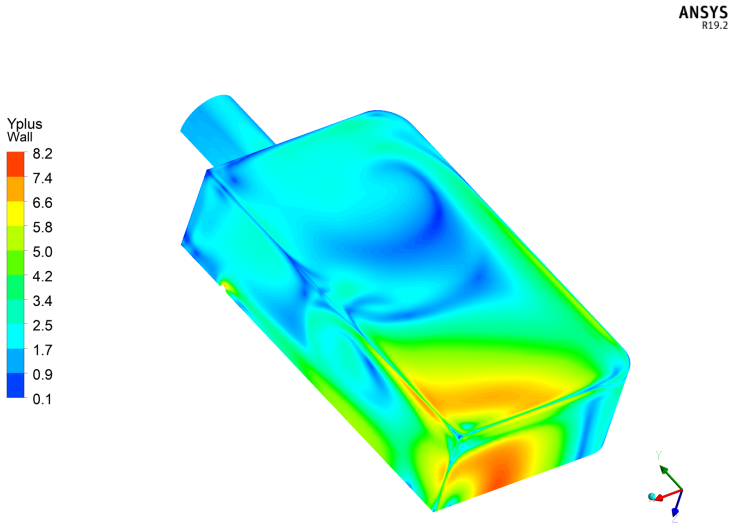

Figure 3.17: Wall y^+ for non-reacting flow using the realizable $k-\varepsilon$ model.

3.3 Simulation of non-reacting flow

The first part of the numerical study considered predicting the non-reacting flow field and turbulence quantity distributions. The case studied was that of mixing between inlet air diluted with N_2 and CO_2 and a fuel stream represented by pure CO_2 with boundary conditions as given in Table 3.2.

3.3.1 Boundary Conditions

Boundary conditions were set in the same manner as in the mesh dependency study, by interpolating the previously acquired velocity, turbulent kinetic energy and turbulent dissipation rate or specific dissipation rate distributions at the inlets. The exhaust outlet was set to pressure outlet. Wall temperature was set to a constant value of 293 K.

3.3.2 Physical models

Species transport with inlet diffusion and the energy equation were enabled. Constant species concentrations were specified at the inlets corresponding to the pipe boundary conditions. Numerical results were gathered using the realizable $k-\varepsilon$, SST $k-\omega$, SSG RSM and BSL RSM models to investigate which model best represented the experiments. Because the convergence of RSM models are relatively sensitive to the initial solution, the SSG RSM model was initialized from the converged realizable $k-\varepsilon$ solution and the BSL RSM model from the SST $k-\omega$ solution. This provided a superior "starting guess" as opposed to the built-in hybrid initialization method. For the two-equation models the production limiter were enabled to improve accuracy. Enhanced wall treatment was used for the realizable $k-\varepsilon$ model, but was not yet implemented in Fluent for RSM models. Out of the available wall treatment options, both the standard wall treatment and non-equilibrium wall functions propose a first layer cell height of $y^+ \geq 30$, considerably higher than the y^+ values of the mesh which were generally $y^+ \leq 6$. This left scalable wall functions as the only relevant option for the SSG RSM model. The PISO algorithm was used for the pressure-velocity coupling, with warped-face gradient correction (WFGC) enabled. WFGC improve gradient accuracy for meshes containing elements with high aspect ratio and non-flat element faces. High aspect ratio elements for the mesh used are

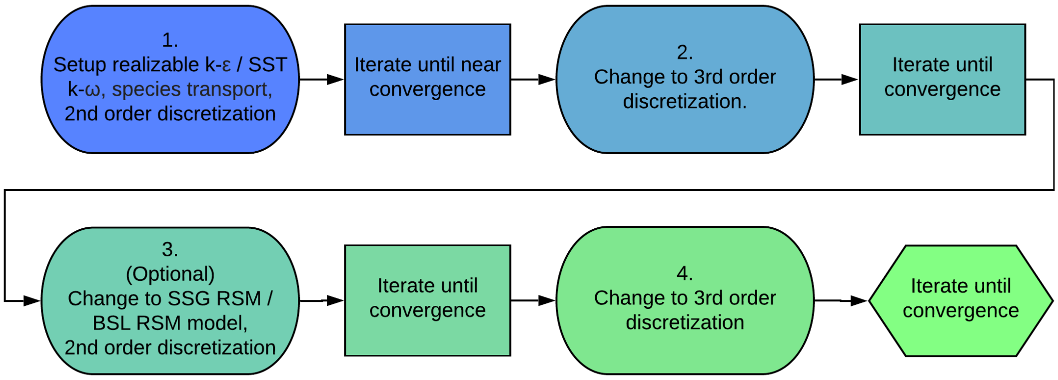

-

Figure 3.18: Simulation strategy for non-reacting flow.

found in the boundary layers and non-flat elements exist as a result of the o-grid blocking explained in section 3.1.2.

3.3.3 Solution strategy and discretization scheme

The first simulations were run using second order upwind discretization for all variables. Starting from the converged second order solution, simulations using third order MUSCL discretization was attempted to yield increased accuracy. This strategy is recommended as higher order schemes are notoriously more difficult to converge. The chance of achieving a converged solution, as well as the convergence rate, are thus improved by starting from a more accurate solution, similar to the strategy employed with increasingly complex turbulence models. While the realizable $k-\varepsilon$ model presented no issues using MUSCL for all variables, the SSG RSM model experienced divergence. Reducing k and ε discretization to the 2nd order QUICK scheme while keeping MUSCL for all other variables remedied this issue. Convergence criteria were identical to the mesh dependency study. A schematic of the solution strategy is presented in figure 3.18.

3.4 Simulation of reacting flow

The second part of the numerical study was aimed at resolving the reacting flow field using finite rate chemistry models as described in section 2.4.3. Different reaction mechanisms, turbulence models and EDC model parameters were compared to find the best setup. Then, predictions of pollutant emissions for various conditions were generated.

3.4.1 Boundary conditions

Velocity and species inlet boundary conditions were set in the same way as for the non-reacting cases, through interpolation of prescribed profiles and constant species concentrations. The exhaust outlet was kept as pressure outlet. Uniform wall temperatures were set based on the average measured temperatures (see section 2.5.2) for the current inlet O_2 concentration. For wall radiation properties, the walls were set as opaque with a diffuse fraction of 1, as recommended in the Fluent manual for unpolished surfaces [25]. The internal emissivity was set to 0.8, based on values for common stainless steels. This was an approximation, as parts of the side combustor walls were clad in a ceramic insulator, while the front and back walls were part quartz glass.

3.4.2 Physical models

Pressure-velocity coupling was provided by the PISO algorithm with WFGC enabled. Turbulence was modeled using the realizable $k-\varepsilon$ model with production limiter and enhanced wall treatment and the SSG RSM model with scalable wall functions. Turbulence-chemistry interaction was modeled using the EDC model with ISAT for final results and the steady diffusion flamelet mixture fraction (SDF-MF) model followed by finite-rate model to generate intial solutions, as will be explained later. Three different reaction mechanisms were used, being the JL and JL2 4-step and WD2 3-step mechanisms. NO formation was predicted using the NO_x pollutant model with the thermal-, prompt- and N_2O mechanisms enabled. O_2 and O concentrations were calculated using the partial-equilibium method. Turbulence-NO_x interaction was provided by a β pdf method, including temperature and O_2 interaction calculated at 20 points. Effects of radiation was included by the DO model, using 4 theta and phi divisions and 3 theta and phi pixels. Adsorption coefficients were calculated using the WSGG model.

3.4.3 Solution strategy and discretization scheme

When simulating the reacting case a more complicated strategy had to be employed. Similar to how the more complex RSM turbulence models are best initiated from a two-equation model solution, the EDC model is best initialized from a "starting guess" provided by some simpler model, in this case the SDF-MF model and finite-rate (FR) chemistry models. As described in section 2.4.3, the EDC model is computationally expensive in comparison to mixture fraction models. Solution time can be significantly reduced and possible divergence avoided by starting from a converged mixture fraction solution. In addition, because the mixture fraction model relies on the "fast chemistry" assumption, it will ignite the reactants even at ambient reactant stream temperatures, ideally removing the need to patch an ignition source or include a pilot flame in the EDC simulation. To make sure that the flame does not blow out before the EDC model finds the reacting path of convergence, the FR model was run until a all residuals were below 10^{-4} before changing to the EDC model. The convergence criterion used required relative residuals to fall below 10^{-6}, except continuity, which was set at 10^{-5}. Area-averaged temperature and mass fraction of CO and NO was monitored at the exhaust outlet, complimenting the previously mentioned velocity and k point monitors. The power law discretization scheme was used for all variables, which can be said to have 1st order accuracy.

When using ISAT, chemistry-integration time is dependent on the specified value of the error tolerance. Large values provide faster run times as more interpolations will be performed as opposed to direct integrations, but larger errors. It is therefore recommended to start a simulation with a large error tolerance which is then reduced as the solution stabilizes and approaches convergence [25]. Adding the reacting flow, pollutant and ISAT simulation strategies to the already established turbulence model and discretization strategies resulted in a rather lengthy procedure which is summarized in figure 3.19.

The final results were generated by starting with a simulation using the realizable $k-\varepsilon$ model and the SDF-MF model for chemistry. After achieving convergence, the chemistry model was changed to species transport, with species and reactions provided by one of the global mechanisms. Volumetric reactions were enabled and calculated through the FR model with ISAT enabled using the suggested starting tolerance of 10^{-3}. The simulation was run until all relative residuals had reduced below 10^{-4}. Next, the turbulence-chemistry model was changed to EDC and ISAT. The flow equations were disabled in order for the chemistry to adapt to the prescribed flow field. After iterating only the

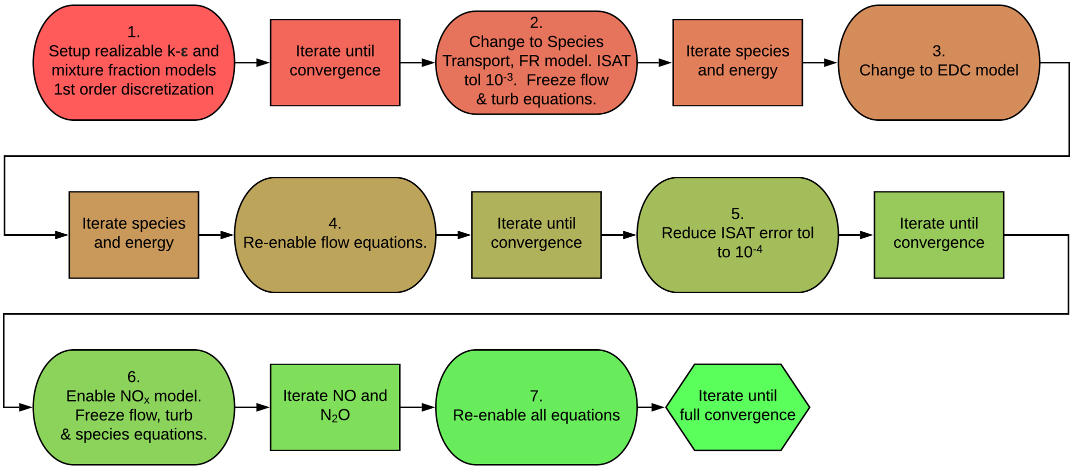

Figure 3.19: Simulation strategy for CDC.

species and energy equations to convergence, the flow, turbulence and radiation equations were enabled again. Once the levels of the temperature and CO monitors leveled off, the ISAT tolerance was reduced to 10^{-4}. After reaching convergence, the pollutant NO_x model was enabled. The flow, energy, turbulence and radiation equations were disabled and the NO and N_2O equations were iterated until convergence. Lastly, all equations were enabled and iterated until convergence.

Chemistry acceleration algorithm study

Before going forward with the reaction mechanism and EDC model parameter studies, the performance of two chemistry acceleration algorithms were evaluated, being ISAT and dynamic cell clustering (DCC). The use of a chemistry acceleration algorithm was necessary in order to reach acceptable computational time. In the evaluation the JL mechanism was used with either direct integration (DI), ISAT or DCC, starting from the same, semi-converged, FR solution and run for a fixed number of computing hours.

Reaction mechanism study

The capability of the computationally cheap global mechanisms to predict CDC behaviour was first analyzed on a coarse, 380 000 element mesh. This was done by running simulations with the JL, JL2 and WD2 mechanisms using the strategy previously described. The three simulations were run with the standard boundary conditions corresponding to 15.5 mol-% O_2, $\phi = 0.9$ and $TI = 25 \quad MW/m^3atm$ as seen in Table 3.3. Interestingly, while the JL and JL2 mechanisms predicted ignition, the WD mechanism did not. To alleviate this problem, a small pilot flame was added at the bottom of the combustor. A small region of four boundary elements were set as a velocity inlet with a uniform velocity of 10 m/s. It was set as a partly reacted mixture with 12.5% CH_4, 25% O_2, 25% H_2O and 12.5% CO_2 (by moles) and a temperature of 1600 K. After adding the pilot flame, the simulation was restarted at the first step.

4

Results and discussion

4.1 Computational domain and boundary conditions

A considerable part of the time spent on this thesis was occupied by setting up the computational domain. More specifically, much time was lost in trying to create a high quality hybrid mesh. Although not directly related to combustion simulation, many lessons were learned that are applicable to any project using ICEM CFD for mesh generation. The improvements seen by changing strategy from a hybrid to full structured mesh cannot be understated. As seen in Table 3.1, all mesh quality metrics were considerably improved. While the initial hybrid mesh showed no convergence issues in simulation of pure aerodynamics (without reactions and species transport) it is entirely possible that the lower element quality would have led to issues later on, as convergence becomes more difficult to achieve with each added level of complex physics. Moreover, a structured mesh was found to be a time saver when performing the mesh dependency study. After the blocking is finalized, it is simple to change the number of nodes on any edge, and generating a number of meshes with varying grid spacing can be done in a few hours. For a hybrid mesh, generating additional meshes after the first will take almost as long, as every step in the process has to be repeated after changing element sizing. The general recommendation is to avoid conformal merging of structured and unstructured meshes in ICEM CFD and attempt to generate a structured grid if possible. If not, a better strategy might be to use a fully unstructured mesh or a different software altogether, of which there are many on the market.

After acquiring the skills required to generate a structured mesh for the combustor geometry, the next important decision was how to deal with inlet pipes and boundary conditions. Because the inclusion of finite-rate chemistry is computationally expensive, there was considerable motivation to minimize the number of elements in the reacting flow simulations. Including the inlet pipes in the combustor mesh would add 50 000 elements or so for geometry alone. Additional elements also would be created due to the fine sizing required near the pipe walls, which would carry over into the combustor domain, as was described in Section 3.1.2. Moreover, most of the worst-quality elements in the structured mesh were located at the intersection between o-grid blocking and rectangular blocking. Thus, avoiding such areas is also of interest for mesh quality. Lastly, flow in the inlet pipes is unaffected by, for example, the choice of turbulence-chemistry model or reaction mechanism, as the reactants are not in contact. It can therefore be solved once for a particular case of mass flow, preheating temperature and composition.

No experimental data were available on the velocity and turbulence profiles in the actual piping, so one can only hypothesize about what they should look like. While the fuel inlet velocity and turbulent kinetic energy seems to be fully developed, it is less obvious regarding the air inlet quantities (Figure 3.10). The air inlet hydrodynamic entrance length predicted by equation (3.1) was only slightly longer than the simulated length at 5.5 inches versus 5.0 inches. On the other hand, the fuel pipe did not appear to be fully developed right after the predicted entrance length, which was 1.2 inches. The profiles presented in figures 3.11 - 3.13 qualitatively resemble results presented in [42], and as time was critical they were deemed good enough for use as boundary conditions. After matching the nodal distribution of the inlet pipes to that of the combustor, the interpolation errors of mass flowrate were below 1%. A low interpolation error would be especially important when comparing numerical results to experimental measurements of the reacting flowfield, as was originally intended. Unfortunately, no trustworthy experimental data were available by the time this report was written. If they were, the interpolation errors would still be lower than the error of the mass flow controllers used in the experimental setup. The nodal spacing used was rather coarse, however, and better resolution of the inlet profiles could have been achieved with a finer pipe mesh. This was difficult to achieve mostly because of the small pipe diameter (1/16") of the fuel inlet in comparison to other dimensions. This led to a compromise between high element aspect and volume ratios, number of elements and resolution at the fuel inlet.

4.2 Non-reacting flow

In the results of the non-reacting flow simulations, the $k-\omega$ and BSL RSM models have been omitted due to not achieving the set convergence criteria. The total number of computing hours to reach convergence for different turbulence models studied are presented in Table 4.1. Computing hours are calculated as the number of processors times the simulation run-time. Several approaches were attempted to reach convergence for the $k-\omega$ and BSL RSM models without success, such as extreme under-relaxation and use of 1st order discretization. It was not possible to achieve convergence for higher order discretization schemes, even if initiating from a converged solution using the 1st order upwind scheme. The velocity magnitude and turbulent kinetic energy monitors never reached a stable value, instead oscillating with an amplitude of more than 10% of their respective values. The residuals, most notably the continuity residual, also did not reach the prescibed values. By this point, the SST $k-\omega$ model had used more than twice as many CPU-hours as the $k-\varepsilon$ models. Thus, even if eventually reaching convergence, the ω models would not be the preferred choice due to considerably higher computational cost. Initiating the BSL RSM model from a converged realizable $k-\varepsilon$ solution did not yield any better results than by starting from a SST $k-\omega$ solution, either.

4.2.1 Velocity field

Contour plots of $\bar{v}$ velocity for the standard $k-\varepsilon$, realizable $k-\varepsilon$, SSG RSM model and experimental data are shown in Figure 4.1. Clearly, the measured and predicted flow fields are quantitatively similar, if not qualitatively. Notably, the measured jet velocities are lower in the upper half of the combustor. This is almost certainly due to experimental errors, as the average air jet velocity must be about 40 m/s to reach the specified mass flow rate. Assuming the lowest flowrates within the given uncertainty range for all streams, the average velocity would still be roughly 39 m/s, which does not explain the discrepancy.

Model	Computing hours [CPU-h]
Standard $k-\varepsilon$	440
Realizable $k-\varepsilon$	450
SSG RSM	720
SST $k-\omega$	>960
BSL RSM	>1200

Table 4.1: Total number of CPU-hours to reach convergence for different turbulence models.

Likely, the error is because of a too high density of seeding particles as the air enters the combustor, leading to the camera capturing a cloud instead of individual, crisp particles and resulting in incorrect tracking of particles by the PIV software. Another interesting phenomenon is that while the $k-\varepsilon$ models predict the jet curving towards the wall, the SSG RSM model seems to predict completely opposite behaviour. The tendency for the jet to curve towards the wall is also seen in the experimental measurements and is a well documented example of the so-called Quanda effect. A closer look at the predicted distributions of v velocity along the air jet, fuel jet and horizontal centerline are seen in Figures 4.2-4.4, respectively. The locations of the three lines are indicated in white on the SSG-RSM contour in figure 4.1.

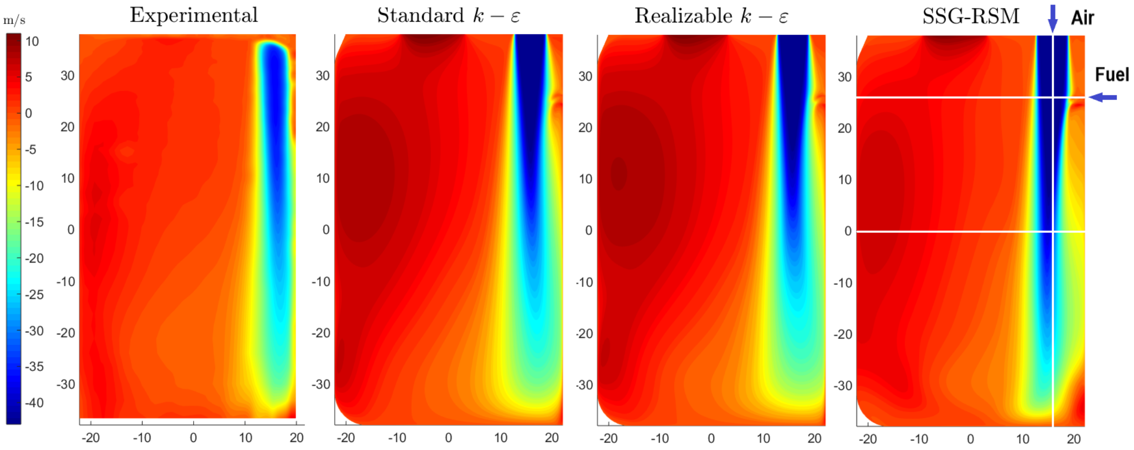

Figure 4.1: $\bar{v}$ velocity contour for standard $k-\varepsilon$ (left) and realizable $k-\varepsilon$ (right).

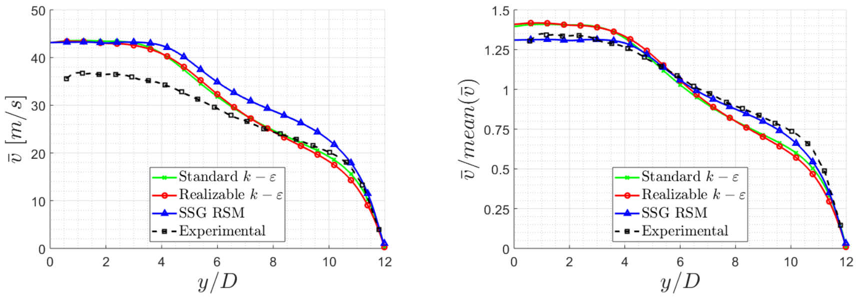

Figure 4.2: Inlet air jet v in absolute values (left) and normalized by the mean jet velocities (right).

Figures 4.2 and 4.3 confirm the systematic errors of the experimental measurements, as the jet centerline velocity is roughly 5 m/s shy of the expected values between $y = 0$

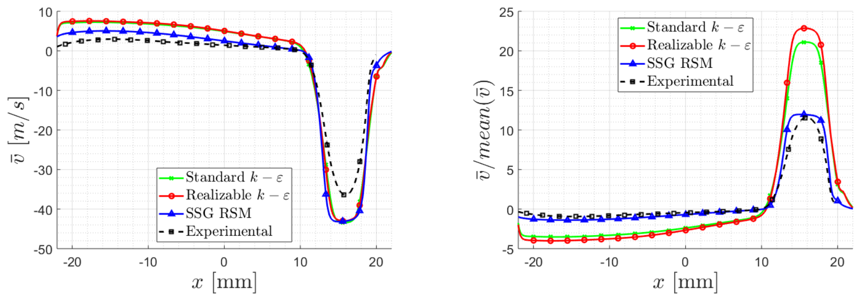

Figure 4.3: Inlet fuel jet v in absolute values (left) and normalized by the mean jet velocities (right).

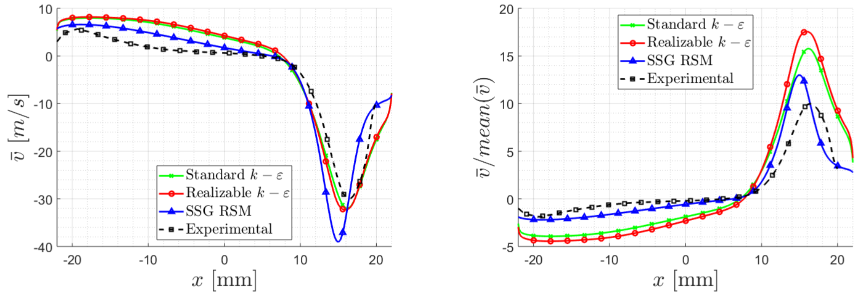

Figure 4.4: Horizontal centerline v in absolute values (left) and normalized by the mean jet velocities (right).

and $y = 6D$. However, if scaling the velocities by their respective mean line value, the SSG RSM model shows excellent agreement. At the half-way point the velocity error has diminished, as seen in Figure 4.4, although the erroneous prediction of jet curvature by the SSG RSM model is notable. The agreement of the scaled velocity magnitude at the centerline is worse, although once again the RSM model shows better conformity.

4.2.2 Turbulence

Profiles of *k* along the air jet, fuel jet and centerline are presented in Figure 4.5. For the experimental results, the three-dimensional *k* was estimated by assuming that the out-of-plane velocity fluctuation was equal to the velocity fluctuation normal to the flow direction.

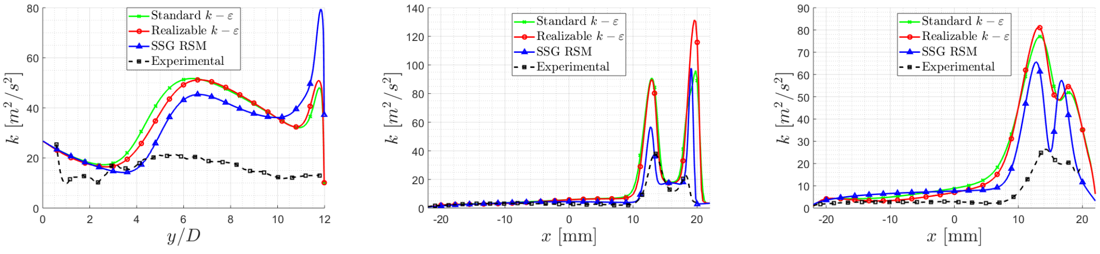

Figure 4.5: k distributions along the air jet (left), fuel jet (center) and centerline (right).

While there is large deviation between simulated and measured values along the air jet, the general trend is at least captured along the fuel jet and centerline. For the latter two, the RSM model once again seems to produce slightly better results, although the validity of the experimental results should be questioned because of the errors previously mentioned. For the SSG RSM model, a comparison between simulated and experimental Reynolds stresses was also made. The results are seen in Figures 4.6-4.8.

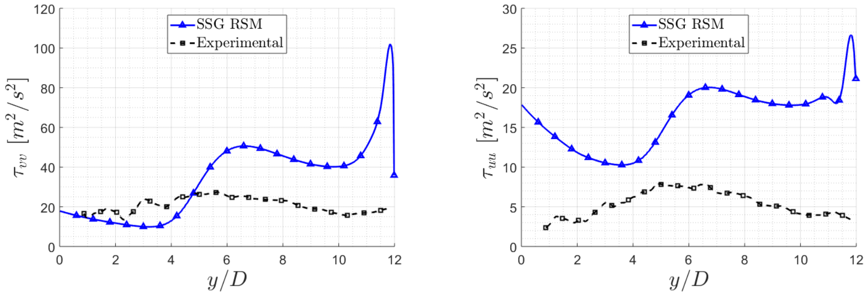

Figure 4.6: Air jet τ_{yy} distribution (left) and τ_{xx} distribution (right).

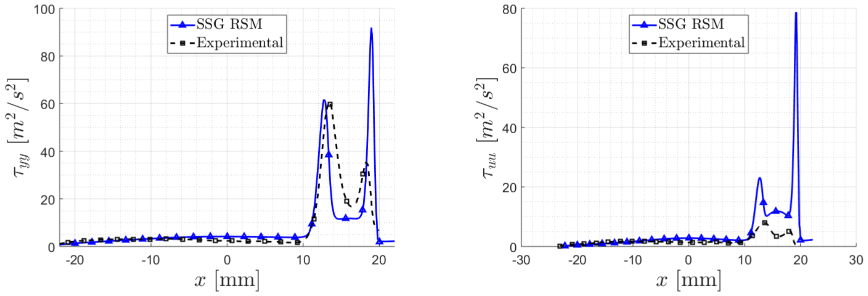

Figure 4.7: Fuel jet τ_{yy} distribution (left) and τ_{xx} distribution (right).

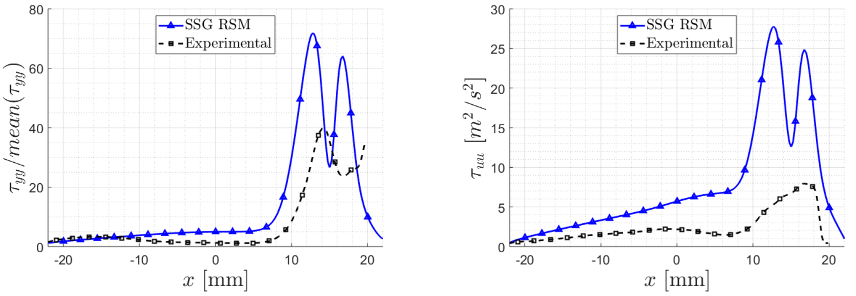

Figure 4.8: Centerline τ_{yy} distribution (left) and τ_{xx} distribution (right).

The air jet once again shows no correlation at all for either stress. However, it is difficult to compare the downstream parts of the jet centerlines as the simulation and experiment showed opposite jet curvatures. Therefore, the values below $y = 6-8D$ may correspond to an entirely different part of the flow field. The fuel jet and centerline τ_{yy} show qualitative agreement. The two maxima are expected due to the shear layers and can be seen in both numerical and experimental result, although the right-most top shows large discrepancy. In the left centerline plot the offset is most likely due to jet curvature. Discrepancies in maximum values may be both due to the experimental errors mentioned earlier and incorrectly set boundary turbulence levels. Scaling the values with their respective mean results in better conformity, as seen in Figure 4.9.

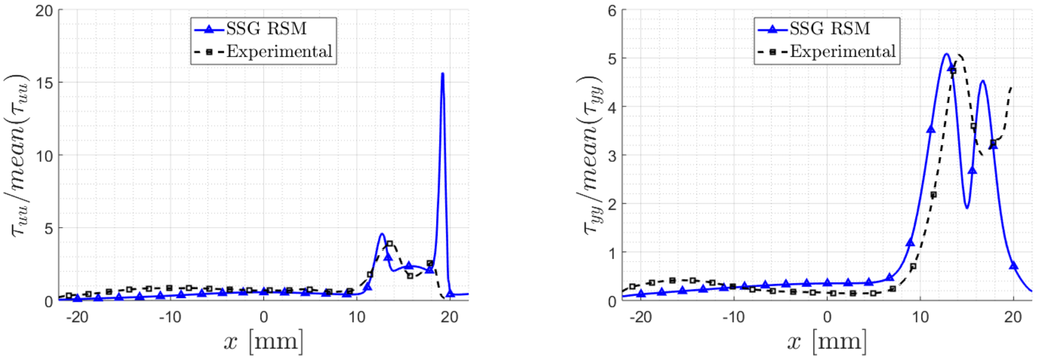

Figure 4.9: Fuel jet normalized τ_{xx} (left) and centerline normalized τ_{yy}(right).

Summarizing the resuls of the non-reacting flow, the SSG RSM model seems to provide the best prediction, if the experimental results can be considered to correctly predict the qualitative aspects of the flow field. Moreover, the higher level of completeness of the SSG RSM model should give it an advantage over the two-equation models, at least theoretically, as the flow contains both strongly curved streamlines and rotation. It is also possible that the capturing of history effects on turbulence is important because of the recirculation zone, as turbulence levels in the recirculating flow directly affect the mixing of reactants as well as flame speed in the shear layers. Based on this argument, the advantage of the SSG RSM model could be increased in the case of reacting flow compared to non-reacting flow. However, the standard and realizable $k-\varepsilon$ model is frequently used for reacting flows in academia ([32, 39, 40, 44], to name a few), and has better convergence behaviour than the RSM model. While the latter showed no issues besides a higher computational cost for the non-reacting flow, problems could arise when adding chemistry and radiation models.

4.2.3 Similarities with the reacting flow field

Unfortunately, the momentum flow rate of "fuel" (CO_2) does not match the one used in the reacting flows. The initial idea was to use propane for the reacting flow. Because CO_2 has a similar molecular weight, it could be used as a substitute to investigate the non-reacting flow field. The flow rate of propane to achieve an equivalence ratio of $\Theta = 0.9$ is vastly different than that of methane, as can be seen if comparing the boundary conditions in Tables 3.2 and 3.3. It was decided to switch fuel to methane because of the relative abundance of available reaction mechanisms. While several well-reviewed mechanisms, both global (i.e WD, JL and their derivatives) and detailed (GRI3.0, DRM22) are available for methane, there are very few for propane. Indeed, many publications are available for presenting at least relatively successful application of these mechanisms to distributed combustion, such as Wang et al. [39] and Kim, Schnell, and Scheffknecht [40]. No well-reviewed simple global propane mechanism could be found in the literature, at least not one that had previously been tested for CDC or MILD combustion. It would not be feasible to use a detailed mechanism such as the San Diego mechanism for every reacting flow simulation, thus the decision was made to use methane instead of propane. With that said, because the momentum of the fuel jet is small compared to the air jet, conclusions drawn here about the accuracy of different turbulence models should still hold for the methane simulations.

4.3 Reacting flow

Solving for the reacting flow posed several difficulties. Firstly, starting the EDC model from a converged solution of the SDF-MF model led to predictions of no reaction at all. Similar to a flame-blowout, after several thousand iterations the temperature field would resemble that of a non-reacting flow being heated by the walls, which had been set to a constant temperature of 1000 K based on measurements. When a finite-rate chemistry model is initiated, the solution can be seen as being at a bifurcation point, having two paths which it can follow: A non-reacting path, where the existing hot gases from the initial field would "blow out" before ignition, and a reacting path, where the flame ignites and is maintained by the recirculation of hot exhaust gas, as in the physical experiments. A strategy had to be found to "nudge" the solution towards the reacting path. For the JL and JL2 mechanisms, it seemed sufficient to solve only the species and energy equations using the finite-rate model (i.e, neglecting turbulence-chemistry interaction and only evaluating rate expressions) until a semi-converged state had been reached. Solving with the EDC model after this resulted in finding the reacting solution path. However, for the WD2 mechanism this was not sufficient and a small pilot flame had to be added, as described in section 3.4.

Significant issues arose when using ISAT in Fluent on the UMD high-performance computing cluster, often causing solver and memory errors that resulted in termination of the simulation. These issues seemed to stem from primarily two causes. The main source was found to be the setting of narrow ISAT tolerances. From a theoretical perspective, this should only result in increased computational time as more chemistry updates would be directly integrated as opposed to tabulated. However, directly lowering the tolerance from the standard value of 10^{-3} to 10^{-5} repeatedly caused crashes. Lowering the tolerance in an incremental fashion worked in the JL2 mechanism simulation, where it could eventually be set to 10^{-5}, whereas this caused the JL simulation to crash, even though the solution had converged at 10^{-4} before lowering the tolerance. Because the outlet CO level was changing in the iterations before the simulation terminated, it is expected that the predicted levels would be different, had a solution been achieved at 10^{-5}. This might have been true for the JL2 mechanism too, if reducing the error tolerance further, to 10^{-6}, although this was not attempted due to a lack of time. Indeed, the Fluent manual suggests that minor species such as CO can require very low tolerances before converging. The second source of simulation termination seemed to be the combination of ISAT and dynamic cell clustering (DCC), another chemistry acceleration algorithm implemented in Fluent. Thus, one or the other had to be chosen. Upon comparison, ISAT was shown to have the best performance, as seen in Table 4.2, where the relative residuals after 500 CPU-h are listed for the equations with highest residual values using direct integration

(DI), ISAT and DCC.

When added to several other delays, for example the lengthy mesh generation procedure and being given incorrect boundary conditions to match experiments, ISAT-related issues led to only a few reacting flow simulations being completed. The initial plan was to compare results from the JL, JL2 and WD2 reaction mechanisms to the GRI 3.0 mechanism using the SSG RSM model and the fine mesh. Because the GRI 3.0 mechanism includes the OH species, a direct comparison to chemiluminescence data could have been made. Then, the best match out of the global mechanisms, or even the GRI 3.0 mechanism, would be used in a parameter study. The original JL and WD mechanisms were designed to produce adequate results in premixed combustion for a range of equivalence ratios. Per definition, non-premixed combustion spans the entire range of possible equivalence ratios and therefore these mechanisms should be compared to a detailed mechanism that does not feature this design error. Another model error could be the use of the non-premixed SDF model. Because the delayed ignition in CDC, mixing of reactants take place before combustion. It is therefore possible that the partially premixed SDF model would produce better results than the non-premixed one. The EDC parameter study would investigate the effects on reaction zone, temperature field and emissions by EDC model parameters. Then, having found the best combination of reaction mechanism and EDC parameters, the effects of air preheating and oxygen level on reaction zone would have been studied. Due to the time constraint, only simulations using the global mechanisms with standard EDC parameters and the realizable $k-\varepsilon$ model on a coarse mesh with 380 000 elements were completed.

	Iterations per CPU-h	Continuity	Energy	CO	H_2
DI	9.8	$1.9 \cdot 10^{-4}$	$6.7 \cdot 10^{-6}$	$3.9 \cdot 10^{-5}$	$5.3 \cdot 10^{-5}$
ISAT	45.7	$3.8 \cdot 10^{-5}$	$9.3 \cdot 10^{-7}$	$8.5 \cdot 10^{-6}$	$3.0 \cdot 10^{-5}$
DCC	95.2	$1.3 \cdot 10^{-4}$	$1.4 \cdot 10^{-6}$	$2.3 \cdot 10^{-5}$	$5.7 \cdot 10^{-5}$

Table 4.2: Convergence behaviour of chemistry acceleration methods. Residual values are relative residuals after 500 CPU-h.

4.3.1 Experimental results

The evolution of the averaged and line-of-sight integrated OH^* radical field from a standard diffusion flame at 21 mol-% O_2 to CDC at 15.5 mol-% O_2 can be seen from direction of the "back" wall in Figure 4.10. The view direction was reversed to facilitate easier comparison to simulation results further on. The intensity scales are local scales in order to visualize both the area occupied by the OH^* reaction zone and the intensity levels. Clearly, the reaction zone as defined by the presence of the OH^* radical increased in size by a significant amount when reducing the O_2 concentration from 21% to 15.5%. Moreover, the maximum intensity was reduced from above 600 AU to 150 AU, indicating that the reactions in which OH^* participate are progressing at a slower rate at 15.5% O_2.

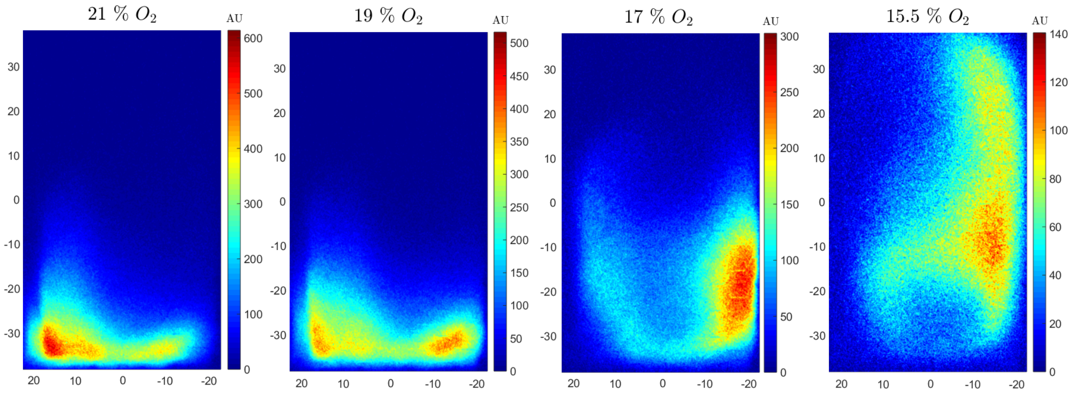

Figure 4.10: Evolution of OH^* intensity by O_2 level. Arbitrary units (AU). $TI = 25\ MW/m^3 atm$, $\Phi = 0.9$ and $T_{in} = 20$ °C.

The dependency of combustor exhaust pollutant levels by O_2 concentration is seen in figure 4.11. As expected by the discussion in section 2.3 and 2.2, the formation of NO is strongly inhibited in the CDC regime, showing a reduction of 97% at 15.5% O_2 as compared to 21 %. On the other hand, the CO levels are increased by over 400%. It is likely that the use of preheated air could counter the increase in CO formation, since low emissions are generally favored by higher temperatures. However, it is likely that this would result in higher NO emissions as well. Due to a lack of time, a preheated case could not be investigated. The exact composition of exhaust gases at every inlet O_2 level can be found in appendix A.

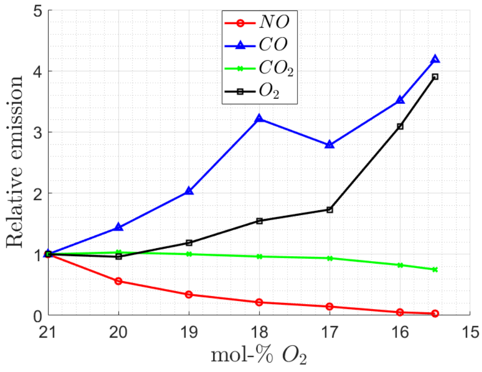

Figure 4.11: Measured dependency of exhaust NO, CO, CO_2 and O_2 vol-% by inlet air O_2 level. Values are scaled by their respective levels at 21 mol-% O_2.

4.3.2 Reaction zone and thermal field

Contour plots of static temperature and reaction rates for the four reactions in the JL and JL2 mechanisms as well as reaction rates of thermal and N_2O path NO will now be discussed. Due to a lack of space, contour plots some interesting species distributions (H_2, O_2 and H_2O) were confined to Appendix A. Plots of the prompt NO rate have been omitted due to only showing production in a small area surrounding the air inlet, similar to the maxima of thermal and N_2O path shown below. In order to visualize the distributions of the entire domain, four planes were used to generate the contour plots. These were the symmetry plane (named "Symmetry" in the figures), a plane offset to the symmetry plane by half the depth, or 0.375 inches (referred to as "Symmetry offset"), a plane through the air inlet axis, perpendicular to the symmetry plane (called "Air inlet" in the figures) and a plane through the exhaust outlet axis, perpendicular to the symmetry plane (named "Exhaust outlet"). Each set of four contours are also presented together in the plots called "Assembly". The planes are viewed from the "back" wall of the combustor, as the assembly view was otherwise obstructed by the symmetry plane.

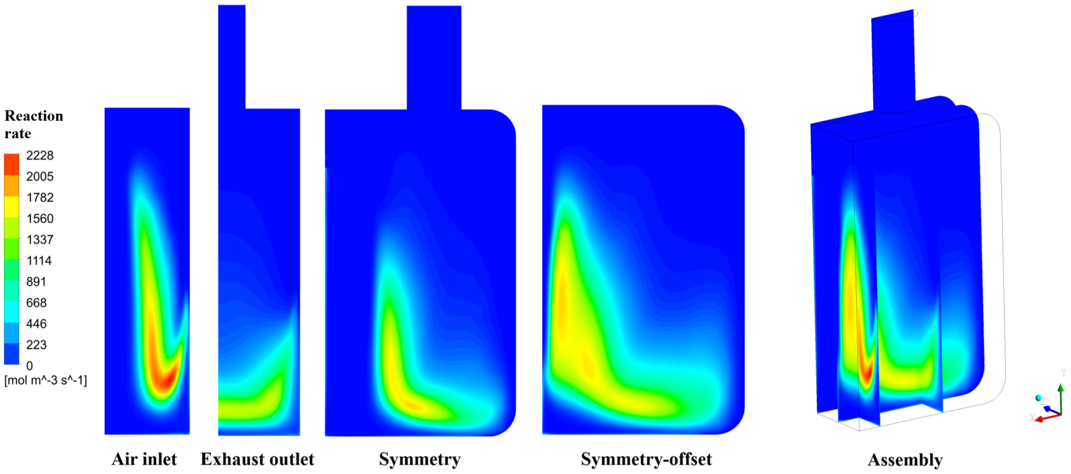

Figure 4.12: Contours of reaction rate for CH_4-O_2 oxidation (reaction 25) in the EDC-JL case.

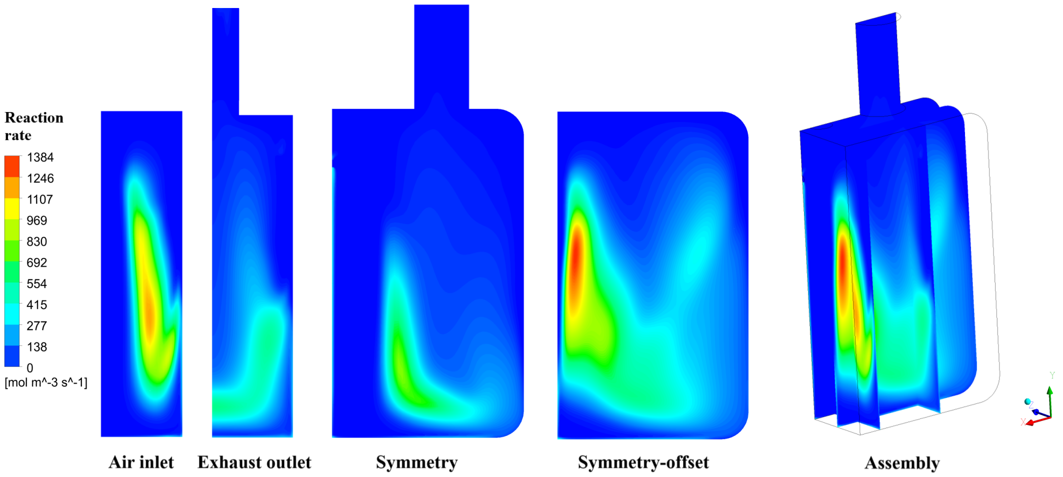

Figure 4.13: Contours of reaction rate for CH_4-O_2 oxidation (reaction 25) in the EDC-JL2 case.

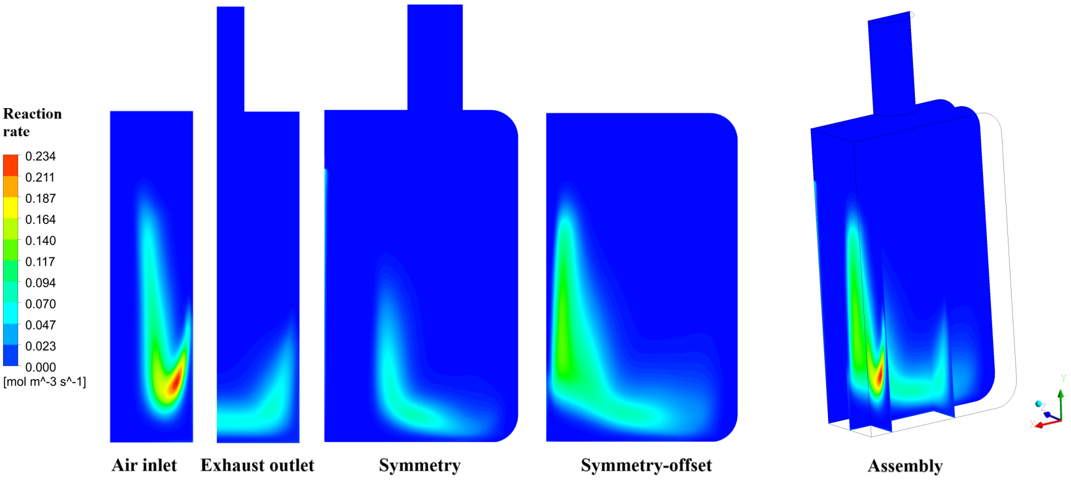

Figure 4.14: Contours of reaction rate for CH_4-O_2 oxidation (reaction 26) in the EDC-JL case.

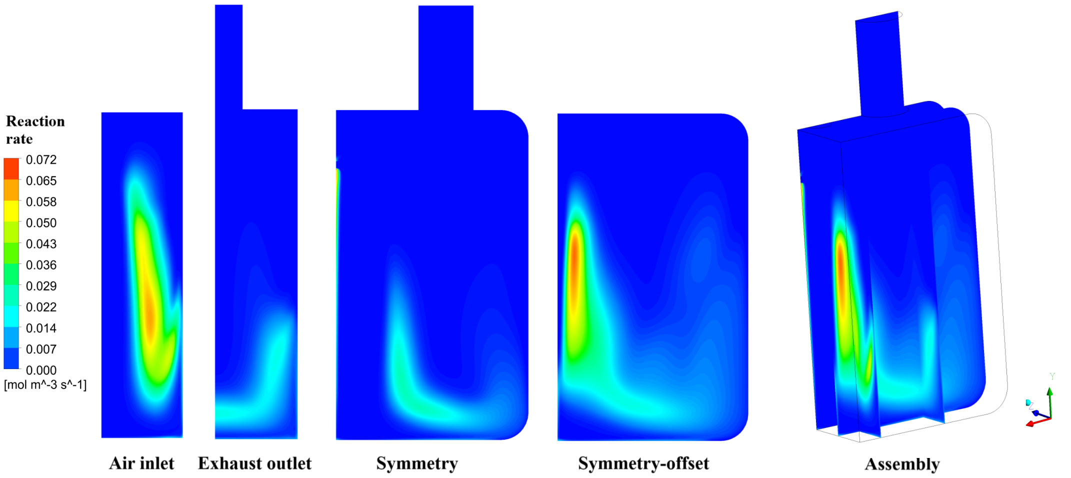

Figure 4.15: Contours of reaction rate for CH_4-O_2 oxidation (reaction 26) in the EDC-JL2 case.

The contours of the CH_4-O_2 oxidation rates (reaction 25) and CH_4-H_2O oxidation rates (reaction 26) are depicted in Figures 4.12- 4.14. Although similar in appearance between the two mechanisms, the JL2 rates are notably lower, with the maximum rate of the CH_4-O_2 oxidation being roughly half that of the JL mechanism and the maximum rate of the CH_4-H_2O being less than half. The slightly larger reaction volumes seen for the JL2 reactions are likely a result of this. The difference in reaction rates is expected to be a result of the difference in local temperatures, which are higher for the JL mechanism in the main reaction areas (see Figures 4.20 and 4.21).

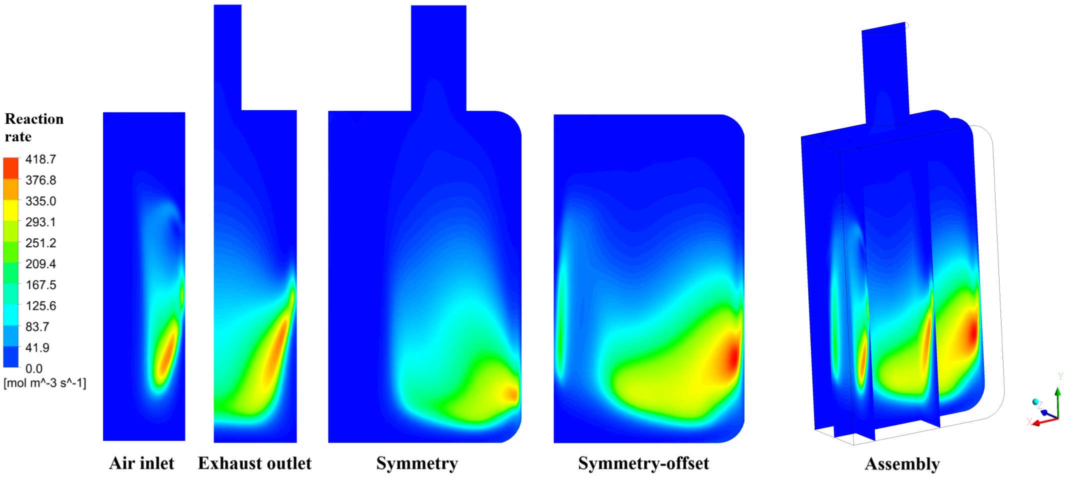

Figure 4.16: Contours of reaction rate for CO oxidation (reaction 27) in the EDC-JL case.

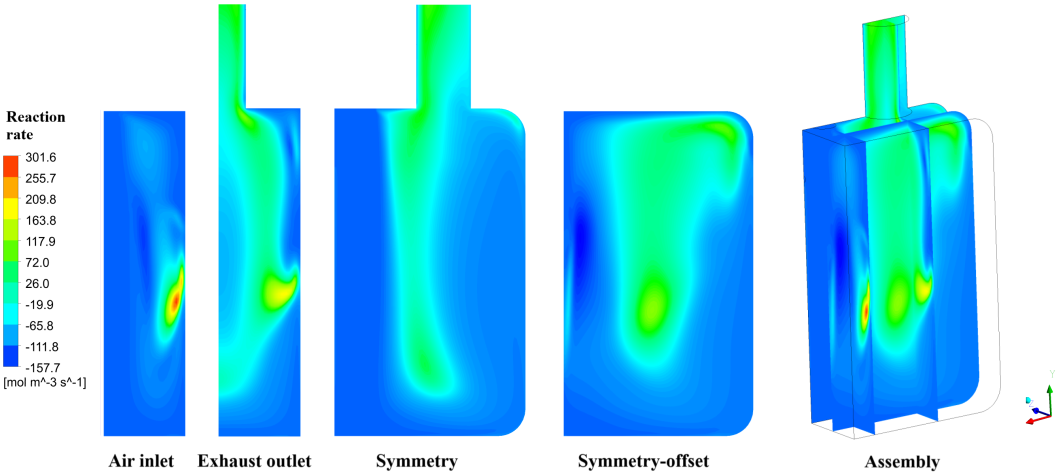

Figure 4.17: Contours of reaction rate for CO oxidation (reaction 27) in the EDC-JL2 case.

Greater differences are seen in the contours of CO-H_2O oxidation (reaction 27) seen in Figure 4.16 and 4.17. Here, the JL2 reaction is distributed over a much larger volume. The backward reaction is seen to have a greater presence, as evidenced by the negative minimum rate of the JL2 contours when compared to the JL contours. This can be explained by the difference in rate coefficients for the CO oxidation reaction (reaction four, 28) between the two mechanisms. The JL2 mechanism has a considerably smaller value of the pre-exponential constant than that of the JL mechanism. While this directly influences the rates of the H_2 oxidation, it results in a larger partial pressure of H_2 present in the JL2 case, because H_2 is not immediately converted to H_2O. This is confirmed in the H_2 distributions presented in Appendix A. While the two CH_4 oxidation reactions are irreversible and thus independent of H_2 concentration, the oxidation of CO (27) is reversible. The presence of H_2 as a product in this reaction will promote reduced forward rates and in some cases a backwards reaction when H_2 levels are significant. The lower rates of H_2 oxidation are clearly seen in Figures 4.18 and 4.19, where the maximum rate of the JL mechanism is 14 orders of magnitude higher than that of the JL2 mechanism. As a result, the H_2O levels are higher in most of the combustor, which is confirmed by contours of H_2O found in Appendix A.

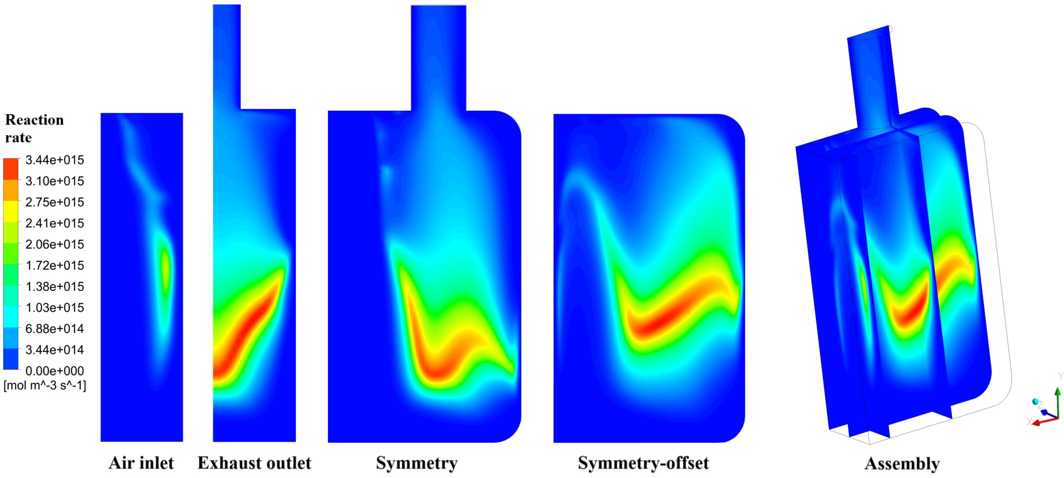

Figure 4.18: Contours of reaction rate for the H_2 oxidation (reaction 28) in the EDC-JL case.

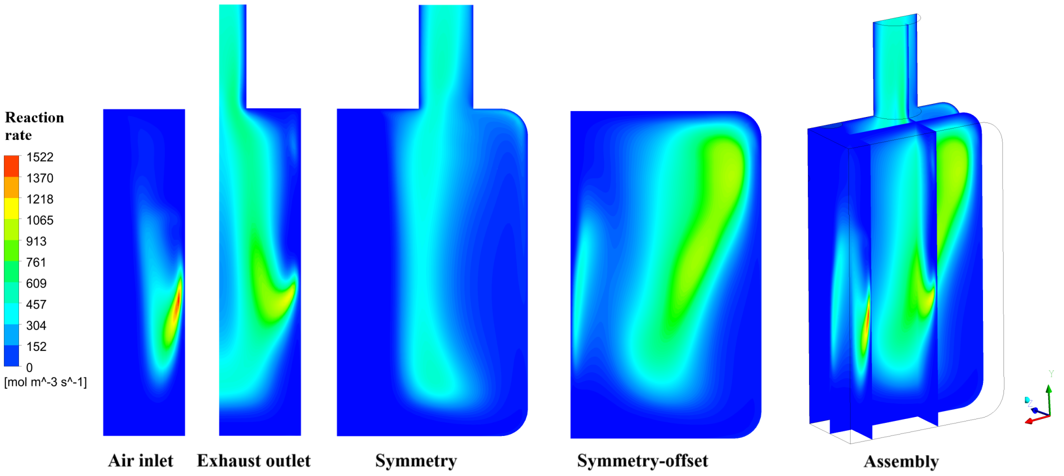

Figure 4.19: Contours of reaction rate for the H_2 oxidation (reaction 28) in the EDC-JL2 case.

Interestingly, while the JL2 mechanism predicts lower reaction rates and larger reaction zones, the temperature field is distinctly more uniform for the JL mechanism. One explanation could be that reactions are completed earlier (upstream) in the JL case, giving more time for mixing and heat transfer to distribute the energy released in the combustion process over a larger fluid volume. The high temperature regions can be correlated to the existence of high reaction rates of the third and fourth reactions (27,28), in both cases, although it is particularly notable for the JL2 mechanism.

No direct comparison to the experimental measurements of OH^* can be made because neither OH or OH^* are included as a species in the simulation. However, OH^* is known to form in high temperature reaction areas. A qualitative comparison can therefore be made by factoring in the temperature and reaction rate distributions of the third and fourth reactions. Because the OH^* chemiluminescence is line-of-sight integrated, the volumetric distributions must be considered and not just the symmetry plane contours. By studying Figures 4.16-4.19, the JL2 mechanism would be expected to produce the best match to experimental data, with the primary reaction zones spanning most of the combustor height, whereas those of the JL mechanism are confined to a smaller region in the bottom half. However, the JL2 temperature field is shifted to the top, where there is minimal OH^* present. It is therefore hard to make a conclusion for which mechanism best represents the measurements, but it may be concluded that the trends seem to be reasonable.

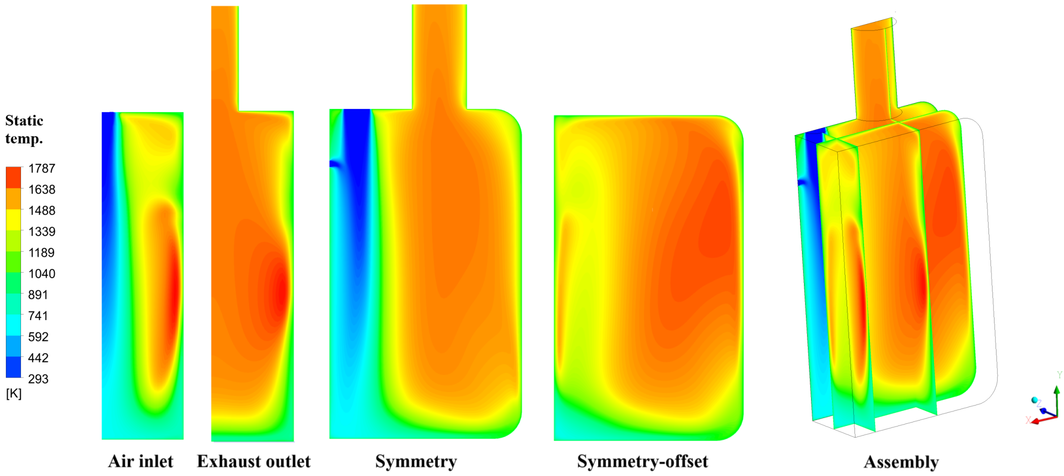

Figure 4.20: Contours of static temperature in the EDC-JL case.

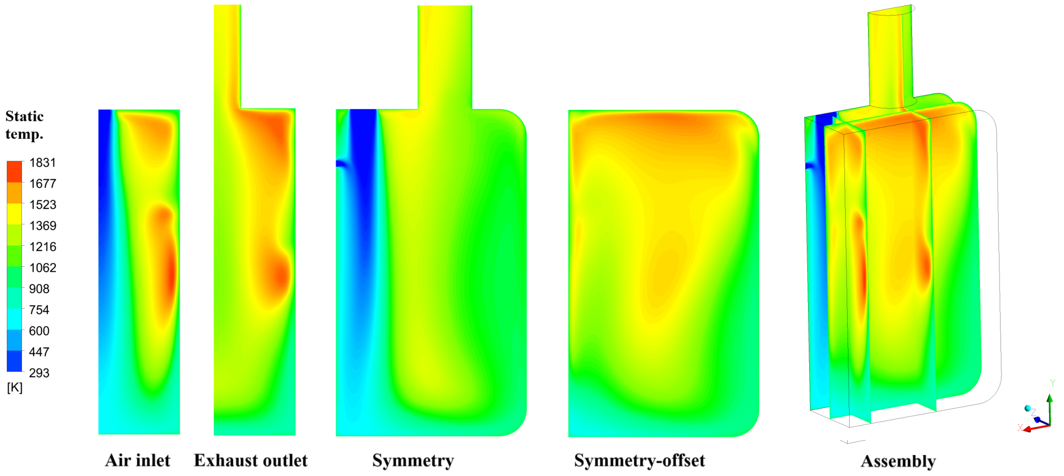

Figure 4.21: Contours of static temperature in the EDC-JL2 case.

Lastly, the NO predictions through the thermal and N_2O mechanisms are presented in Figures 4.22-4.25. Interestingly, all reaction rate maxima are found in a small region near the air inlet, with rates in the rest of the combustor volume being significantly lower. This is likely a result of the combination of high oxygen concentration and relatively high temperature (contours of O_2 distribution are found in Appendix A). In reality, the rates are primarily governed by presence of OH and O (as seen in reactions 13-20) in regions of high temperature, and the maximum rates are then expected to be found in the primary flame zone. The simulated rates are based on O_2 in the partial-equilibrium approach and thus ends up predicting the maxima in a rather unlikely region. However, besides the maxima, the regions of NO formation approximately correlate to those of high CO and H_2 oxidation rates and temperature. The reaction rates of both the thermal and N_2O mechanism are an order of magnitude higher for the JL2 case as is evidenced by the higher outlet NO level presented in Table 4.3. This is reasonable given the higher partial pressures of O_2 and higher temperature peaks.

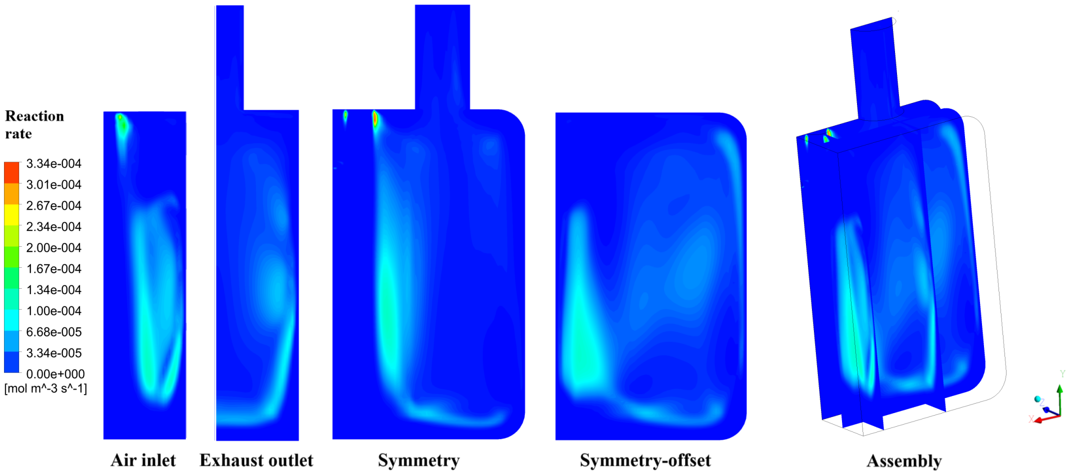

Figure 4.22: Contours of reaction rate for the thermal route NO mechanism in the EDC-JL case.

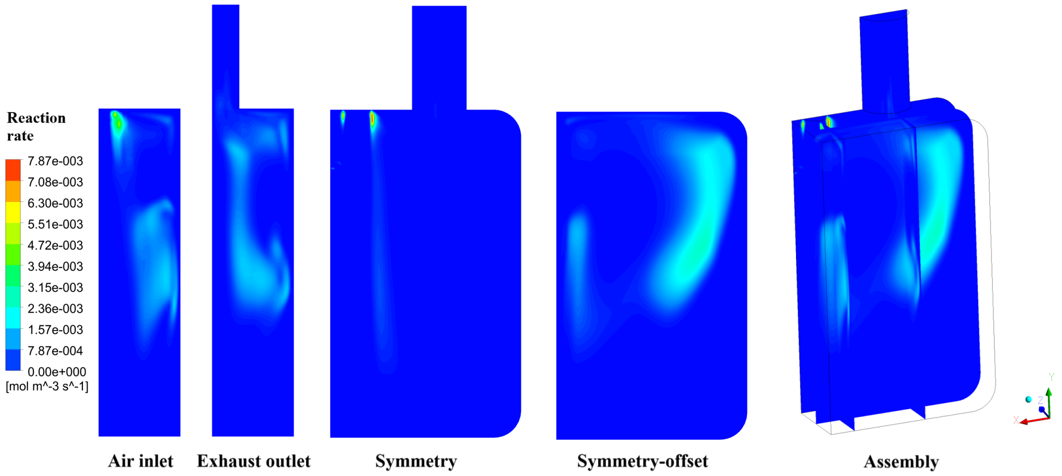

Figure 4.23: Contours of reaction rate for the thermal route NO mechanism in the EDC-JL2 case.

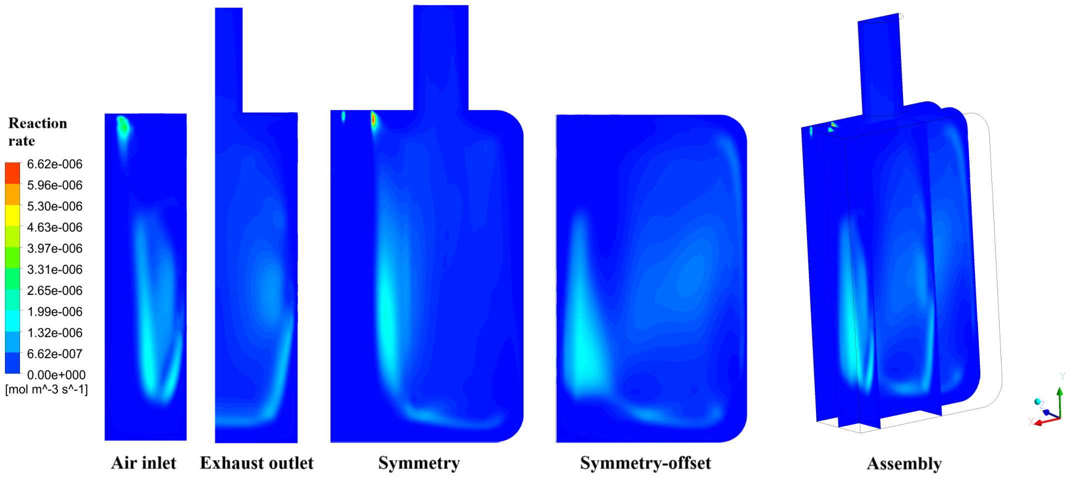

Figure 4.24: Contours of reaction rate for the N_2O route NO mechanism in the EDC-JL case.

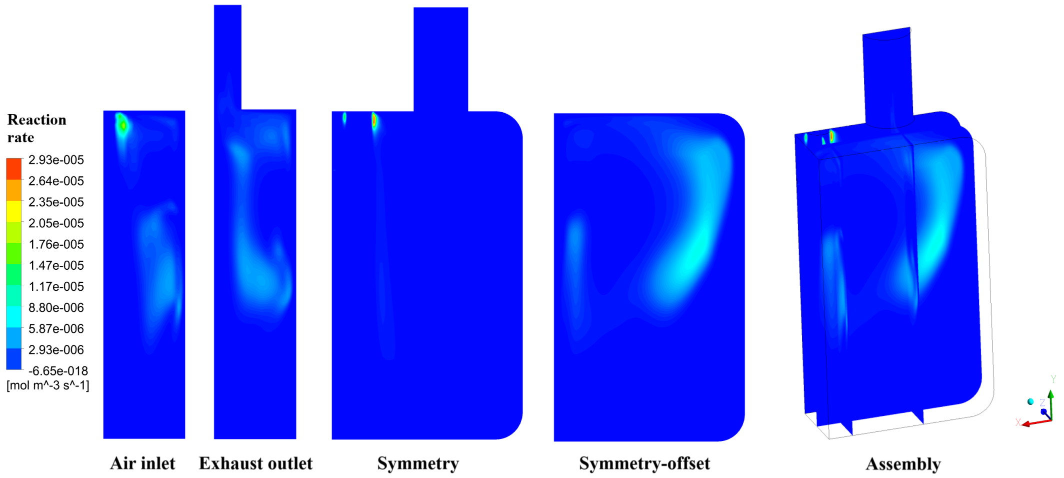

Figure 4.25: Contours of reaction rate for the N_2O route NO mechanism in the EDC-JL2 case.

Pollutant emissions and outlet temperature

The predicted levels of temperature and species concentration in the exhaust outlet are presented in Table 4.3. The simulated values were evaluated at the exhaust outlet plane and corrected to dry mass fraction by removal of the mass fraction of H_2O, which was 0.080, 0.0825 and 0.0763 for the SDF-MF, EDC-JL and EDC-JL2 cases, respectively.

	SDF-MF	EDC-JL	EDC-JL2	Experimental
Avg. outlet T [K]	1369	1503	1389	1310
Mass-ppm CO	1239	58.2	15690	6450
Mass-ppm NO	159	0.0600	0.0784	0.593
Mass frac. CO_2	0.146	0.150	0.124	0.125
Mass frac. O_2	0.0232	0.0200	0.0353	0.0504

Table 4.3: Average outlet temperatures and exhaust gas compositions. Mass fractions are calculated on a dry basis.

Based on the fact that the JL2 mechanism features a modification made to better represent combustion under diluted conditions, it is not unexpected that it seems to be more accurate than the JL mechanism for CDC. Indeed, the JL2 mechanism outperforms the JL mechanism in every metric, giving predictions unexpectedly close to measured values considering that the coarse mesh and the first order discretization scheme that were used expected to introduce notable errors. The JL simulation predicts outlet temperature and species concentrations that resemble those of a conventional diffusion flame (see Figure 4.11) with relatively low levels of O_2 and CO and high temperature. Contours of O_2 distribution as seen in Appendix A confirm that predictions of O_2 levels inside the combustor are considerably lower for the JL mechanism than the JL2 mechanism. While the JL mechanism over-predicted the outlet temperature by almost 15%, the JL2 mechanism differed by only 6%. The level of agreement could be improved by setting of more exact, non-uniform boundary temperature, as it dictates the rate of heat transferred to the environment. Even greater improvements are seen in the levels of CO_2 and O_2, particularly for that of CO_2 which were nearly identical between JL2 and experimental measurement.

Emissions of minor species such as CO and NO are notoriously difficult to simulate, and as such the disparities seen with the JL2 mechanism should not be too disheartening. At any rate, the CO level is on the same order of magnitude as the experimental measurement, unlike that of the JL mechanism. A source of disparity can stem from the fact that the measured exhaust composition is sampled 1.5 inches further downstream than the simulations. According to Figure 4.17, oxidation of CO is still taking place in the exhaust pipe for the JL2 mechanism. The simulated CO level can therefore be expected to be lower further downstream. Predicted CO levels could also have been improved by further reducing the ISAT error tolerance.

The predictions of NO were expected to be inaccurate due to the mechanisms used not including NO chemistry and therefore requiring the need of the separate NO_x model. Moreover, the thermal and N_2O reaction rates are calculated based on O and OH concentration, neither of which were present in the species that were solved for, thus further reducing accuracy by necessitating the partial-equilibrium approximation to calculate their concentrations based on O_2. Lastly, it is interesting to note that based on the metrics presented here, the mixture fraction model performed better than the EDC model with the JL mechanism. While the latter allows for more detailed analysis of chemical kinetics and has a larger margin for improvements, it can be useful to remember that the EDC model requires more careful setup, for example in choice of reaction mechanism. If it is not used correctly, it might not be worthwhile to use over simpler models such as the SDF-MF.

5

Conclusion

5.1 Turbulence model

Unfortunately, the quality of the PIV data makes it difficult to draw a confident conclusion regarding choice of turbulence model. However, based on convergence behaviour and computational expense the $k-\omega$ and BSL RSM model are ruled out for this particular combination of geometry and flow conditions. Assuming that the PIV is erroneous in a way where the flow pattern is correctly captured although the magnitude of mean velocity is incorrect, the SSG RSM model seems to provide the best accuracy based on the agreement shown for the air and fuel jet velocity distributions. The incorrect jet curvature is relatively minor in comparison to the deviations shown by the $k-\varepsilon$ models in Figures 4.2 and 4.3. On the other hand, it can be argued that because the experimental data is not trustworthy, no conclusions can be drawn. The higher level of completeness offered by the SSG RSM model should theoretically provide an advantage, particularly for the present flow case which features strongly curved streamlines, rotation and possibly important turbulence history effects. Higher quality PIV data of the non-reacting flow, preferably complemented by PIV data of the reacting flow, is necessary in order to make a confident recommendation on choice of turbulence model.

5.2 Reaction mechanism

Simulations using the JL2 mechanism produced unexpectedly accurate results when compared to experimental measurements, considering the coarse mesh that was used (380 000 elements) and first-order discretization scheme. The modified JL mechanism (JL2) performed better than the standard JL mechanism in most regards. It predicted reduced reaction rates and larger reaction zones which roughly matched the location of high temperature reactions as shown by OH^* chemiluminescence. However, the JL mechanism predicted a more uniform temperature field, which could be explained by earlier ignition and heat release that spread downstream, whereas the JL2 mechanism predicted ignition closer to the outlet. The outlet temperature and species composition simulated using the JL2 mechanism matched measured values well, with an average temperature difference of less than 80 K and nearly identical levels of CO_2. The outlet temperature prediction could be improved by setting more accurate (non-uniform) wall boundary temperatures. However, pollutant emission levels showed larger disparity. The CO level was over-predicted by almost three times the measured value. The fact that measured emissions were sampled 1.5 inches further downstream than in the simulations could be a significant source of error, as the reaction rate contours for JL2 showed that CO oxidation was still taking place in the exhaust pipe. Another source of possible errors is the disparity between the range of equivalence ratios that the global mechanisms were optimized for in premixed mode and the full range that is found in the non-premixed mode that was studied here. The use of partial-equilibrium approximations in the NO_x models can explain the errors in the prediction of NO levels. For the predicted level to reach an acceptable error margin it might be necessary to use a reaction that includes at least the formation of OH and O, or preferably NO_x chemistry so that the external model can be avoided altogether. Lastly, improved results for the mixture fraction model could be achieved by using the partially-premixed version instead of the non-premixed SDF model.

5.3 Future research

Future research efforts should be directed at completing the initial objectives of this thesis in greater detail. The non-reacting flow simulations could be re-done at a momentum flow rate which matches that of the reacting flow. Then, after making sure that the PIV data is trustworthy, a better conclusion could be drawn about the choice of turbulence model. A way to improve the comparison is to use a stereo setup of cameras. This would allow capturing the out-of-plane mean and fluctuating velocity. A direct comparison between three-dimensional turbulence kinetic energy can then be made. Moreover, the actual turbulence levels in the inlet pipes could be estimated and the levels specified in the simulations corrected accordingly.

Reacting flow simulation should then be carried out using both the realizable $k-\varepsilon$ model and the SSG RSM model. The results could be compared to the PIV of the reacting flow field, particularly comparing turbulence levels in the shear layer, where both streamline curvature and turbulence history effects should be notable. Subsequent simulations are performed using the best fit of turbulence model and boundary conditions. The mesh dependency study in this thesis assumed that temperature and species fields would exhibit the same behaviour as that of the flow and turbulence fields. Preferably, a mesh dependency study should be performed on the reacting flow, tracking the change of temperature in addition to velocity and turbulent kinetic energy. The research could be initiated by comparing the accuracy of global mechanisms to the GRI 3.0 mechanism. This could be complemented by investigating the use of reduced or skeletal mechanisms. Reduced mechanisms are mathematically optimized from detailed mechanisms (for methane usually GRI 3.0) to offer greater accuracy and detail when compared to global mechanisms, at a computational cost that is lower than that of detailed mechanisms. An example is the 19-species reduced methane-air mechanism including NO_x chemistry developed by Lu and Law [45]. However, rate expressions do not follow the standard Arrhenius formula used in the global and detailed mechanisms. Evaluation of reduced mechanism reaction rates then require modification of subroutine files in Chemkin, which was found to be too time consuming to be included in this thesis. Besides studying different reaction mechanisms, various EDC parameter combinations should be investigated to find a setup which best captures the distributed nature of CDC. A modified local parameter EDC model proposed by Parente et al. [32] was briefly described in section 2.4.3 and can be implemented in Fluent using user-defined functions (UDFs). Results can be compared to a solution acquired using the more detailed and computationally expensive transported PDF model. A wholly different line of inquiry that could have comparable ratio between accuracy and computational cost is use of unsteady RANS simulation with a partially-premixed SDF model. While not taking finite rate chemistry into account, the lower cost of the mixture fraction model would allow for unsteady simulation, which would have other benefits. Preferably, results would also be compared to PIV measurements of the reacting flow and temperature fields. Indeed, measurement of the symmetry plane temperature field would much improve the assessment of turbulence-chemistry models, as currently the exhaust gas composition and OH chemiluminescence were the only available experimental methods for reacting flow. The temperature field can be measured using PIV by adding a thermography camera set. After finding an optimal setup of turbulence model, turbulence-chemistry model and reaction mechanism, the actual behaviour of CDC can be studied. For example, by observing changes in reaction zone sizes and reaction rates of different reactions as the inlet O_2 level is reduced or the inlet air temperature is increased.

Bibliography

[1] *World Energy Model - Scenario analysis of future energy trends*. 2018. URL: https://www.iea.org/weo/weomodel/ (visited on 01/18/2019).

[2] *Greenhouse gas emission statistics - emission inventories*. June 2018. URL: http://ec.europa.eu/eurostat/statistics-explained/index.php/Greenhouse_gas_emission_statistics_-_emission_inventories (visited on 01/17/2019).

[3] F. Xing, A. Kumar, Y. Huang, S. Chan, C. Ruan, S. Gu, and X. Fan. "Flameless combustion with liquid fuel: A review focusing on fundamentals and gas turbine application". In: *Applied Energy* 193 (2017), pp. 28–51. DOI: 10.1016/j.apenergy.2017.02.010.

[4] T. C. Lieuwen and V. Yang. *Gas turbine emissions*. Cambridge University Press, 2013.

[5] *British Petroleum - The changing energy mix*. 2018. URL: https://www.bp.com/en/global/corporate/sustainability/climate-change/a-low-carbon-future/the-changing-energy-mix.html (visited on 01/18/2019).

[6] S. M. Correa. "Power generation and aeropropulsion gas turbines: From combustion science to combustion technology". In: *Symposium (International) on Combustion* 27.2 (1998), pp. 1793–1807. DOI: 10.1016/s0082-0784(98)80021-0.

[7] A. H. Lefebvre and D. R. Ballal. *Gas turbine combustion: alternative fuels and emissions*. 3rd ed. CRC, 2010.

[8] A. Poullikkas. "An overview of current and future sustainable gas turbine technologies". In: *Renewable and Sustainable Energy Reviews* 9.2 (2005), pp. 409–443. DOI: https://doi.org/10.1016/j.rser.2004.05.009.

[9] M. P. Boyce. *Gas turbine engineering handbook*. 4th ed. Elsevier, 2012.

[10] A. E. Khalil and A. K. Gupta. "Towards colorless distributed combustion regime". In: *Fuel* 195 (May 2017), pp. 113–122. DOI: 10.1016/j.fuel.2016.12.093.

[11] S. M. Correa. "A Review of NOx Formation Under Gas-Turbine Combustion Conditions". In: *Combustion Science and Technology* 87.1-6 (1993), pp. 329–362. DOI: 10.1080/00102209208947221.

[12] A. Rebola, M. Costa, and P. J. Coelho. "Experimental evaluation of the performance of a flameless combustor". In: *Applied Thermal Engineering* 50.1 (July 2012), pp. 805–815. DOI: 10.1016/j.applthermaleng.2012.07.027.

[13] A. Cavaliere and M. De Joannon. "Mild Combustion". In: *Progress in Energy and Combustion Science* 30 (2004), pp. 329–366. DOI: 10.1016/j.pecs.2004.02.003..

[14] R. Weber, J. P. Smart, and W. V. Kamp. “On the (MILD) combustion of gaseous, liquid, and solid fuels in high temperature preheated air”. In: *Proceedings of the Combustion Institute* 30.2 (2005), pp. 2623–2629. DOI: `10.1016/j.proci.2004.08.101`.

[15] A. E. Khalil and A. K. Gupta. “Swirling distributed combustion for clean energy conversion in gas turbine applications”. In: *Applied Energy* 88.11 (2011), pp. 3685–3693. DOI: `10.1016/j.apenergy.2011.03.048`.

[16] A. E. Khalil and A. K. Gupta. “Acoustic and Heat Release Signatures for Oxy-fuel Swirl Assisted Distributed Combustion”. In: *Applied Energy* 193 (May 2017), pp. 125–138. DOI: `10.2514/6.2017-4812`.

[17] N. Peters. *Turbulent combustion*. 1st ed. Cambridge University Press, 2000.

[18] H. Tsuji, A. K. Gupta, T. Hasegawa, M. Katsuki, K. Kishimoto, and M. Morita. *High temperature air combustion from energy conservation to pollution reduction*. CRC Press, 2003.

[19] M. Katsuki and T. Hasegawa. “The science and technology of combustion in highly preheated air”. In: *Symposium (International) on Combustion* 27.2 (1998), pp. 3135–3146. DOI: `10.1016/s0082-0784(98)80176-8`.

[20] *Protecting the environment and the energy supply*. URL: `https://www.acare4europe.org/sria/flightpath-2050-goals/protecting-environment-and-energy-supply-0`.

[21] A. Veríssimo, A. Rocha, and M. Costa. “Importance of the inlet air velocity on the establishment of flameless combustion in a laboratory combustor”. In: *Experimental Thermal and Fluid Science* 44 (June 2013), pp. 75–81. DOI: `10.1016/j.expthermflusci.2012.05.015`.

[22] A. E. Khalil and A. K. Gupta. “Velocity and turbulence effects on high intensity distributed combustion”. In: *Applied Energy* 125 (July 2014), pp. 1–9. DOI: `10.1016/j.apenergy.2013.11.078`.

[23] S. B. Pope. *Turbulent flows*. Cambridge Univ. Press, 2010.

[24] D. C. Wilcox. *Turbulence modeling for CFD*. 3rd ed. DCW Industries, 2006.

[25] *ANSYS Academic Research Fluent, Release 19.2, Help System, Theory Guide, Chapter 4: Turbulence*. 2019. URL: `https://ansyshelp.ansys.com/account/secured?returnurl=/Views/Secured/corp/v192/flu_th/flu_th_chap_turbulence.html`.

[26] W. Jones and B. Launder. “The prediction of laminarization with a two-equation model of turbulence”. In: *International Journal of Heat and Mass Transfer* 15.2 (1972), pp. 301–314. DOI: `10.1016/0017-9310(72)90076-2`.

[27] T.-H. Shih, W. W. Liou, A. Shabbir, Z. Yang, and J. Zhu. “A new k- eddy viscosity model for high reynolds number turbulent flows”. In: *Computers Fluids* 24.3 (1995), pp. 227–238. DOI: `10.1016/0045-7930(94)00032-t`.

[28] F. R. Menter. “Two-equation eddy-viscosity turbulence models for engineering applications”. In: *AIAA Journal* 32.8 (1994), pp. 1598–1605. DOI: `10.2514/3.12149`.

[29] C. G. Speziale, S. Sarkar, and T. B. Gatski. “Modelling the pressure–strain correlation of turbulence: an invariant dynamical systems approach”. In: *Journal of Fluid Mechanics* 227.-1 (1991), p. 245. DOI: `10.1017/s0022112091000101`.

[30] B. E. Launder, G. J. Reece, and W. Rodi. “Progress in the development of a Reynolds-stress turbulence closure”. In: *Journal of Fluid Mechanics* 68.3 (1975), pp. 537–566. DOI: `10.1017/S0022112075001814`.

[31] A. Rebola, P. J. Coelho, and M. Costa. “Assessment of the Performance of Several Turbulence and Combustion Models in the Numerical Simulation of a Flameless Combustor”. In: *Combustion Science and Technology* 185.4 (Mar. 2013), pp. 600–626. DOI: `10.1080/00102202.2012.739222`.

[32] A. Parente, M. R. Malik, F. Contino, A. Cuoci, and B. B. Dally. “Extension of the Eddy Dissipation Concept for turbulence/chemistry interactions to MILD combustion”. In: *Fuel* 163 (2016), pp. 98–111. DOI: `10.1016/j.fuel.2015.09.020`.

[33] B. Magnussen. “On the structure of turbulence and a generalized eddy dissipation concept for chemical reaction in turbulent flow”. In: *19th Aerospace Sciences Meeting* (Jan. 1981). DOI: `10.2514/6.1981-42`.

[34] A. De, E. Oldenhof, P. Sathiah, and D. Roekaerts. “Numerical Simulation of Delft-Jet-in-Hot-Coflow (DJHC) Flames Using the Eddy Dissipation Concept Model for Turbulence–Chemistry Interaction”. In: *Flow, Turbulence and Combustion* 87.4 (2011), pp. 537–567. DOI: `10.1007/s10494-011-9337-0`.

[35] M. J. Evans, P. R. Medwell, and Z. F. Tian. “Modeling Lifted Jet Flames in a Heated Coflow Using an Optimized Eddy Dissipation Concept Model”. In: *Combustion Science and Technology* 187.7 (June 2015), pp. 1093–1109. DOI: `10.1080/00102202.2014.1002836`.

[36] G. P. Smith, D. M. Golden, M. Frenklach, N. W. Moriarty, B. Eiteneer, M. Goldenberg, C. T. Bowman, R. K. Hanson, S. Song, W. C. Gardiner, and et al. *GRI-Mech 3.0*. URL: `http://combustion.berkeley.edu/gri-mech/version30/text30.html`.

[37] W. Jones and R. Lindstedt. “Global reaction schemes for hydrocarbon combustion”. In: *Combustion and Flame* 73.3 (1988), pp. 233–249. DOI: `10.1016/0010-2180(88)90021-1`.

[38] N. M. Marinov, C. K. Westbrook, and W. J. Pitz. *Transport phenomena in combustion: proceedings of the Eighth International Symposium on Transport Phenomena in Combustion (ISTP-VIII) held in San Francisco, California, July 16-20, 1995*. Ed. by S. H. Chan. Taylor Francis, 1996.

[39] L. Wang, Z. Liu, S. Chen, and C. Zheng. “Comparison of Different Global Combustion Mechanisms Under Hot and Diluted Oxidation Conditions”. In: *Combustion Science and Technology* 184.2 (2012), pp. 259–276. DOI: `10.1080/00102202.2011.635612`.

[40] J. P. Kim, U. Schnell, and G. Scheffknecht. “Comparison of Different Global Reaction Mechanisms for MILD Combustion of Natural Gas”. In: *Combustion Science and Technology* 180.4 (2008), pp. 565–592. DOI: `10.1080/00102200701838735`.

[41] C. K. Westbrook and F. L. Dryer. “Simplified Reaction Mechanisms for the Oxidation of Hydrocarbon Fuels in Flames”. In: *Combustion Science and Technology* 27.1-2 (1981), pp. 31–43. DOI: `10.1080/00102208108946970`.

[42] F. Russo and N. T. Basse. “Scaling of turbulence intensity for low-speed flow in smooth pipes”. In: *Flow Measurement and Instrumentation* 52 (2016), pp. 101–114. DOI: `10.1016/j.flowmeasinst.2016.09.012`.

[43] H. K. Versteeg and W. Malalasekera. *An introduction to computational fluid dynamics: the finite volume method*. 2nd ed. Pearson Education, 2007.

[44] A. Mardani. “Optimization of the Eddy Dissipation Concept (EDC) model for turbulence-chemistry interactions under hot diluted combustion of CH 4 /H 2”. In: *Fuel* 191 (2017), pp. 114–129. DOI: `10.1016/j.fuel.2016.11.056`.

[45] T. Lu and C. K. Law. “A criterion based on computational singular perturbation for the identification of quasi steady state species: A reduced mechanism for methane oxidation with NO chemistry”. In: *Combustion and Flame* 154.4 (2008), pp. 761–774. DOI: `10.1016/j.combustflame.2008.04.025`.

Appendix A

Additional results

Exhaust gas composition measurements

Below are presented the measured exhaust gas compositions at seven cases between standard air-combustion (21 mol-%) to CDC (15.5 mol-%).

O_2 level [mol-%]	21	20	19	18	17	16	15.5
Avg. NO [ppm-vol]	12.11	6.78	4.12	2.58	1.74	0.60	0.36
Std. dev. NO [ppm-vol]	0.03	0.17	0.04	0.03	0.04	0.05	0.04
Avg. CO [ppm-vol]	1626	2332	3292	5227	4528	5715	6803
Std. dev. CO [ppm-vol]	9.38	47.5	45.0	105	81.1	56.6	22.2
Avg. CO_2 [vol-%]	10.09	10.39	10.10	9.71	9.45	8.32	7.57
Std. dev. CO_2 [vol-%]	0.01	0.04	0.01	0.05	0.02	0.04	0.05
Avg. O_2 [vol-%]	1.19	1.14	1.41	1.84	2.06	3.68	4.65
Std. dev. O_2 [vol-%]	0.03	0.03	0.02	0.04	0.03	0.00	0.05

Measured exhaust gas compositions at varying O_2 levels. Levels are calculated on a dry basis.

Simulated species distributions

Below are presented contour plots of mass fraction of H_2, O_2 and H_2O for the EDC-JL and EDC-JL2 cases.

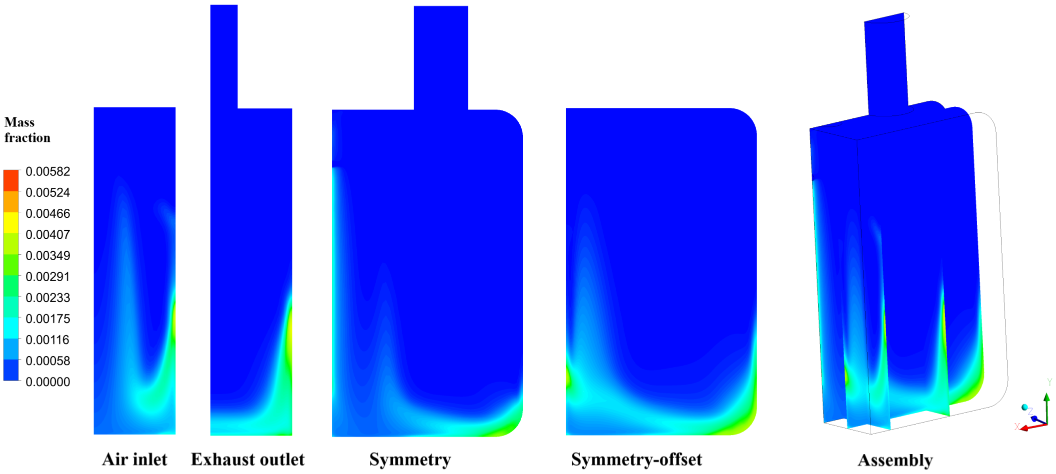

Air inlet **Exhaust outlet** **Symmetry** **Symmetry-offset** **Assembly**

Contours of H_2 mass fraction in the EDC-JL case.

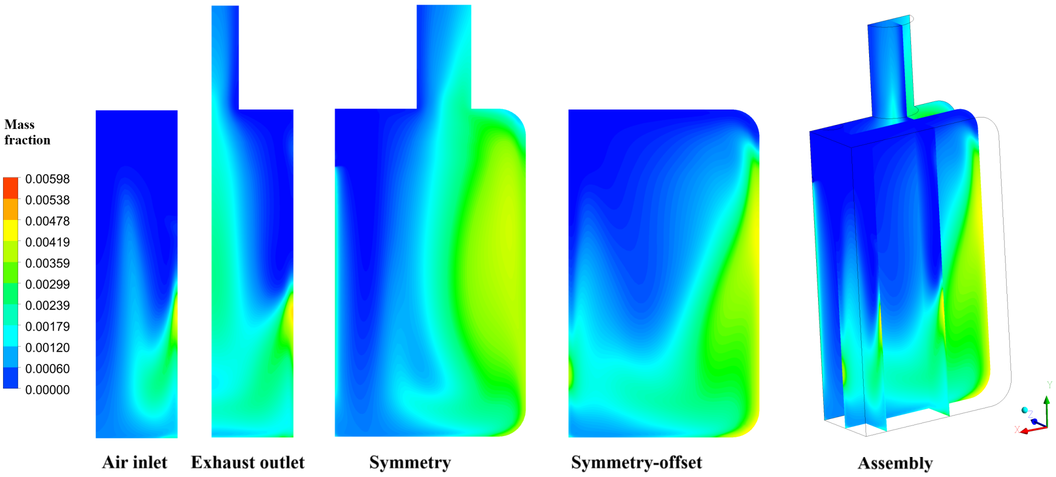

Air inlet **Exhaust outlet** **Symmetry** **Symmetry-offset** **Assembly**

Contours of H_2 mass fraction in the EDC-JL2 case.

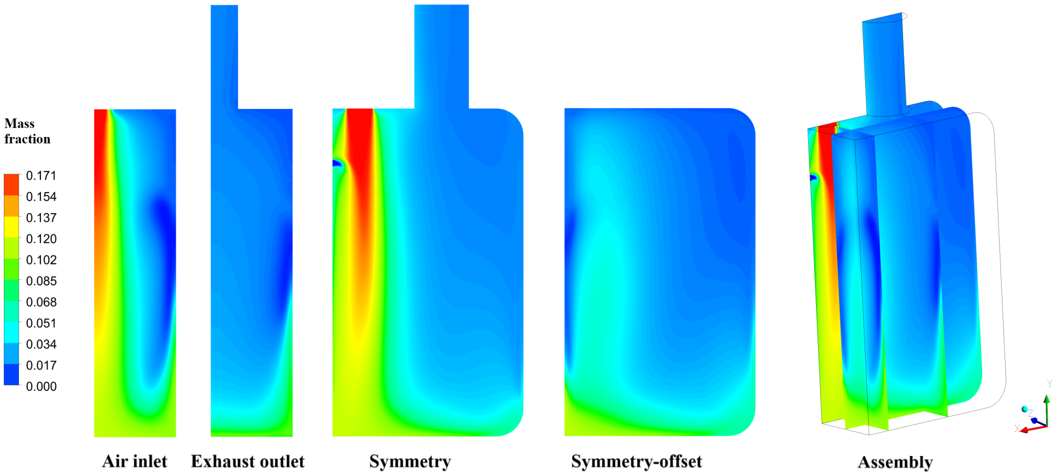

Air inlet **Exhaust outlet** **Symmetry** **Symmetry-offset** **Assembly**

Contours of O_2 mass fraction in the EDC-JL case.

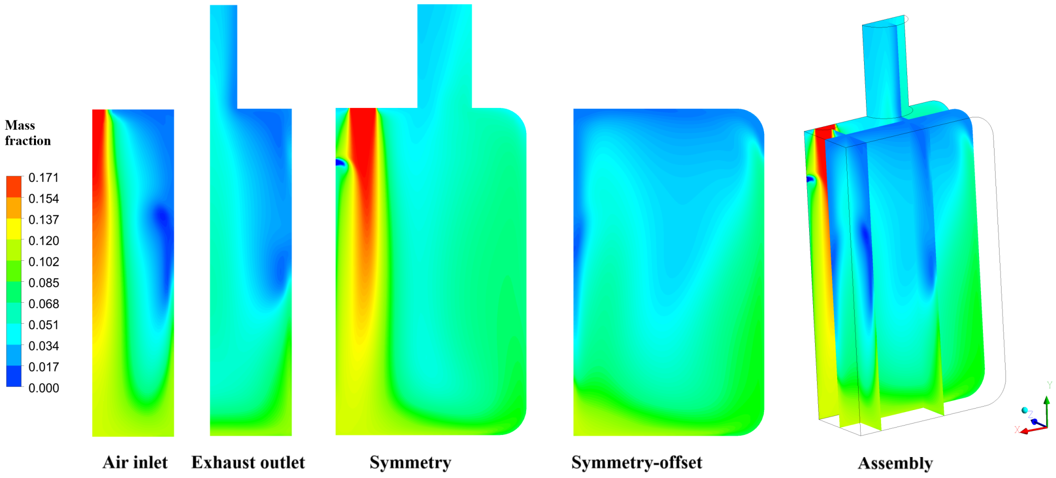

Contours of O_2 mass fraction in the EDC-JL2 case.

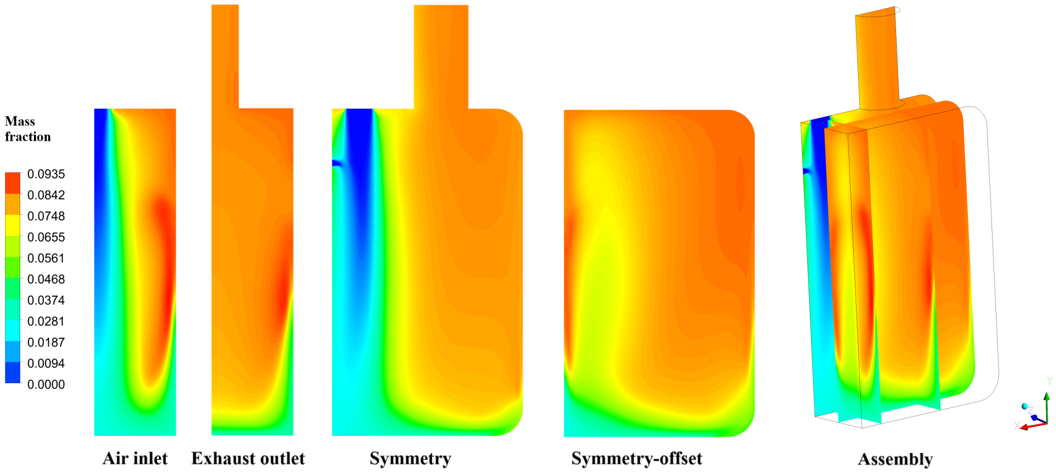

Contours of H_2O mass fraction in the EDC-JL case.

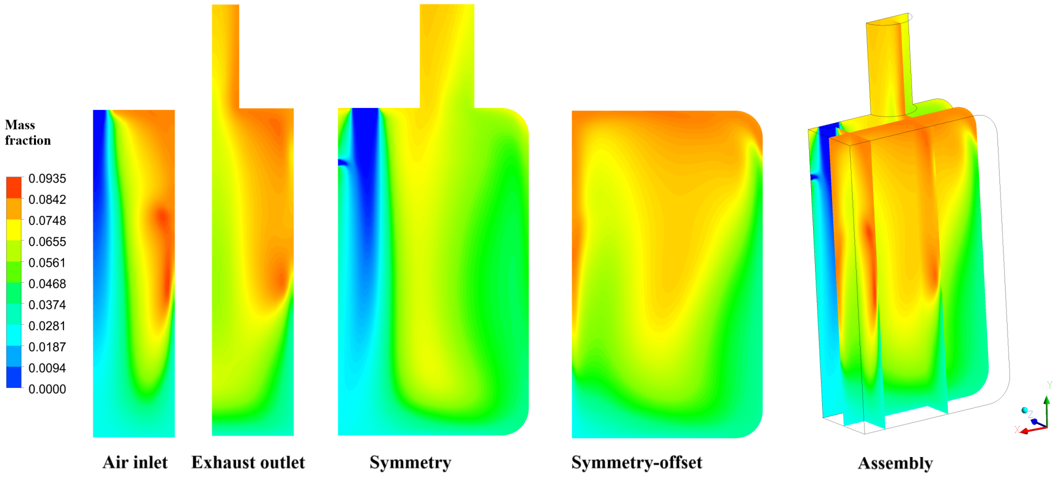

Contours of H_2O mass fraction in the EDC-JL2 case.

Appendix B

Global methane-air reaction mechanisms

Reaction rate parameters

Reaction	A	β	E	Reaction order
25	$7.82 \cdot 10^{11}$	0	30000	$[CH_4]^{0.5}[O_2]^{1.25}$
26	$3.00 \cdot 10^{11}$	0	30000	$[CH_4][O_2]$
27, f	$2.75 \cdot 10^{12}$	0	20000	$[CO][H_2O]$
27, r	$6.71 \cdot 10^{13}$	0	27200	$[CO_2][H_2]$
28/31, f	$2.5 \cdot 10^{12}$	0	35000	$[H_2][O_2]^{0.5}$
28/31, r	$3.47 \cdot 10^{13}$	0	95200	$[H_2O]$
29	$1.59 \cdot 10^{13}$	0	47800	$[CH_4]^{0.7}[O_2]^{0.8}$
30, f	$3.98 \cdot 10^{8}$	0	34990	$[CO][O_2]^{0.25}[H_2O]^{0.5}$
30, r	$6.18 \cdot 10^{13}$	-0.97	95200	$[CO][O_2]^{-0.25}[H_2O]^{0.5}$

Table B.1: Reaction rate parameters for the JL and WD mechanisms. Forward rate parameters indicated by f and reverse rate parameters by r. Units of A are $mole - cm^3 - s$ *and E are* $J/mole$*.*

Chemkin mechanism implementation

Jones-Lindstedt mechanism

```
! 4-Step Jones-Lindstedt Mechanism for methane-air combustion
! Adapted for Chemkin Pro by Hampus Olsson, Lund University

ELEMENTS
O H C N
END

SPECIES
CH4     O2      CO      H2      H2O     CO2     N2
END

REACTIONS
CH4 + 0.5O2 => CO + 2H2              7.82E13     0      30000
FORD /CH4 0.5/
FORD /O2 1.25/
CH4 + H2O => CO + 3H2                3E11        0      30000
CO + H2O <=> CO2 + H2                2.75E12     0      20000
REV                                  /6.71E13    0      27200/
H2 + 0.5O2 <=> H2O                   1.209E18   -1      40000
REV                                  /7.06E17   -0.877  97900/
FORD /H2 0.25/
FORD /O2 1.5/
RORD /H2 -0.75/
RORD /O2 1/
RORD /H2O 1/
END
```

Modified Jones-Lindstedt mechanism

```
! 4-Step modified Jones-Lindstedt Mechanism for methane-air combustion
! Adapted for Chemkin Pro by Hampus Olsson, Lund University

ELEMENTS
O H C N
END

SPECIES
CH4     O2      CO      H2      H2O     CO2     N2
END

REACTIONS
CH4 + 0.5O2 => CO + 2H2              7.82E13     0   30000
FORD /CH4 0.5/
FORD /O2 1.25/
CH4 + H2O => CO + 3H2                3E11        0   30000
CO + H2O <=> CO2 + H2                2.75E12     0   20000
REV                                  /6.71E13    0   27200/
H2 + 0.5O2 <=> H2O                   2.50E12     0   35000
REV                                  /3.48E13    0   95200/
FORD /H2 1/
FORD /O2 0.5/
RORD /H2O 1/
END
```

Modified Westbrook-Dryer mechanism

```
! 3-Step Modified Westbrook-Dryer Mechanism for methane-air combustion
! Adapted for Chemkin Pro by Hampus Olsson, Lund University

ELEMENTS
O H C N
END

SPECIES
CH4     O2      CO      H2      H2O     CO2     N2
END

REACTIONS
CH4 + 1.5O2 => CO + 2H2O            1.59E13 0       47800
FORD /CH4 0.7/
FORD /O2 0.8/
CO + 0.5O2 <=> CO2                  3.98E14         0       40700
REV                                 /5.0E8          0       40700/
FORD /CO 1.0/
FORD /O2 0.25/
FORD /H2O 0.5/
RORD /CO2 1/
H2 + 0.5O2 <=> H2O                  2.5014E12       0       34991
REV                                 /3.48E13        0       95196/
FORD /H2 1/
FORD /O2 0.5/
RORD /H2O 1/
```

Appendix C

The Fluent NO model

In Ansys Fluent, all reactions of the thermal NO mechanism (reactions 13-15) are implemented. However, only the first reaction of the prompt NO route (reaction 21) and the first two reactions of the N_2O route (reactions 16 and 17) are considered. The Arrhenius rate constants are shown in Table C.1. Reaction rates are not shown as the rates are calculated in a different manner than those of the global methane-air and GRI 3.0 mechanism. The partial-equilibrium approach calculates concentration of O by the following expression

$$[\mathrm{O}] = AT^{\beta}e^{-\frac{E/R}{T}}[\mathrm{O}]^{0.5}$$

and the concentration of OH is calculated by

$$[\mathrm{OH}] = AT^{\beta}e^{-\frac{E/R}{T}}[\mathrm{O}]^{0.5}[\mathrm{H_2O}]^{0.5} \quad .$$

The rates of both are found in table C.1 below. The rate of thermal NO production is evaluated as

$$\frac{d[\mathrm{NO}]}{dt} = 2k_{f,13}[\mathrm{O}][\mathrm{N_2}]\frac{(1-\frac{k_{r,13}k_{f,14}[\mathrm{NO}]^2}{k_{f,13}k_{f,14}[\mathrm{N_2}][\mathrm{O_2}]})}{(1+\frac{k_{r,13}[\mathrm{NO}]}{k_{f,14}k_{f,15}[\mathrm{O_2}][\mathrm{OH}]})} \quad ,$$

and the rate of prompt NO by

$$\frac{d[\mathrm{NO}]}{dt} = fAe^{-\frac{E/R}{T}}[\mathrm{O_2}]^a[\mathrm{N_2}][\mathrm{CH_4}](RT/p)^{a+1} \quad ,$$

where f is a function of equivalence ratio Φ, as

$$f = 4.75 + 0.0819 - 23.2\Phi + 32\Phi^2 - 12.2\Phi^3 \quad ,$$

and a is a function of O_2 concentration as given by

$$a = \begin{cases} 1.0 & 4.1\cdot 10^{-3} \leq X_{O_2} \\ -3.95 - 0.9ln(X_{O_2}) & 4.1\cdot 10^{-3} \leq X_{O_2} \leq 1.1\cdot 10^{-2} \\ -0.35 - 0.1ln(X_{O_2}) & 1.1\cdot 10^{-2} \leq X_{O_2} \leq 3.0\cdot 10^{-2} \\ 0 & 3.0\cdot 10^{-2} \leq X_{O_2} \end{cases}$$

where X_{O_2} is the molar concentration of $chO2$. Lastly, the rate of NO production through the N_2O route is given by

$$\frac{d[\mathrm{NO}]}{dt} = 2(k_{f,17}[\mathrm{N_2O}][\mathrm{O}] - 2(k_{r,17}[\mathrm{NO}]^2$$

where the concentration of N_2O is calculated as

$$[\mathrm{N_2O}] = \frac{k_{f,16}[\mathrm{N_2}][\mathrm{O}][\mathrm{M}] + k_{r,17}[\mathrm{NO}]^2}{k_{r,16}[\mathrm{M}] + k_{f,17}[\mathrm{o}]}$$

Reaction	A	β	E/R
13, f	$1.80 \cdot 10^8$	0	38370
13, r	$3.80 \cdot 10^7$	0	425
14, f	$1.80 \cdot 10^4$	1	-4680
14, r	$3.81 \cdot 10^3$	0	20820
15, f	$7.10 \cdot 10^7$	0	450
15, r	$1.70 \cdot 10^8$	0	24560
21	$6.40 \cdot 10^6$	0	36502
16, f	$4.40 \cdot 10^{32}$	-8.358	29234
16, r	$4.00 \cdot 10^8$	0	28234
17, f	$2.90 \cdot 10^7$	0	11651
17, r	$1.45 \cdot 10^{-29}$	9.259	11651
[O]	$3.66 \cdot 10^1$	0.5	27123
[OH]	$2.13 \cdot 10^2$	-0.57	4595

Table C.1: Reaction rate parameters for the thermal, prompt and N_2O route NO mechanisms. Forward rate parameters indicated by f and reverse rate parameters by r. Units of A are $mole - cm^3 - s$ and E are $J/mole$.

Appendix D

The GRI 3.0 mechanism

Reaction mechanism

```
! 12/8/08 CVN removed Ar, C3H8, C3H7
!
! GRI-Mech Version 3.0 7/30/99  CHEMKIN format
! See README30 file at anonymous FTP site unix.sri.com, directory gri;
! WorldWideWeb home page http://www.me.berkeley.edu/gri_mech/ or
! through http://www.gri.org , under 'Basic  Research',
! for additional information, contacts, and disclaimer

ELEMENTS
O  H  C  N

END
SPECIES
H2       H        O        O2       OH       H2O      HO2      H2O2
C        CH       CH2      CH2(S)   CH3      CH4      CO       CO2
HCO      CH2O     CH2OH    CH3O     CH3OH    C2H      C2H2     C2H3
C2H4     C2H5     C2H6     HCCO     CH2CO    HCCOH    N        NH
NH2      NH3      NNH      NO       NO2      N2O      HNO      CN
HCN      H2CN     HCNN     HCNO     HOCN     HNCO     NCO
!AR        C3H7     C3H8
CH2CHO   CH3CHO  N2
END

REACTIONS
2O+M<=>O2+M                              1.200E+17    -1.000         .00
H2/ 2.40/ H2O/15.40/ CH4/ 2.00/ CO/ 1.75/ CO2/ 3.60/ C2H6/ 3.00/ !AR/  .83/
O+H+M<=>OH+M                             5.000E+17    -1.000         .00
H2/2.00/ H2O/6.00/ CH4/2.00/ CO/1.50/ CO2/2.00/ C2H6/3.00/ !AR/ .70/
O+H2<=>H+OH                              3.870E+04     2.700     6260.00
O+HO2<=>OH+O2                            2.000E+13      .000         .00
O+H2O2<=>OH+HO2                          9.630E+06     2.000     4000.00
O+CH<=>H+CO                              5.700E+13      .000         .00
O+CH2<=>H+HCO                            8.000E+13      .000         .00
O+CH2(S)<=>H2+CO                         1.500E+13      .000         .00
O+CH2(S)<=>H+HCO                         1.500E+13      .000         .00
O+CH3<=>H+CH2O                           5.060E+13      .000         .00
O+CH4<=>OH+CH3                           1.020E+09     1.500     8600.00
O+CO(+M)<=>CO2(+M)                       1.800E+10      .000     2385.00
   LOW/ 6.020E+14      .000      3000.00/
H2/2.00/ O2/6.00/ H2O/6.00/ CH4/2.00/ CO/1.50/ CO2/3.50/ C2H6/3.00/ !AR/ .50/
O+HCO<=>OH+CO                            3.000E+13      .000         .00
O+HCO<=>H+CO2                            3.000E+13      .000         .00
O+CH2O<=>OH+HCO                          3.900E+13      .000     3540.00
O+CH2OH<=>OH+CH2O                        1.000E+13      .000         .00
O+CH3O<=>OH+CH2O                         1.000E+13      .000         .00
O+CH3OH<=>OH+CH2OH                       3.880E+05     2.500     3100.00
O+CH3OH<=>OH+CH3O                        1.300E+05     2.500     5000.00
O+C2H<=>CH+CO                            5.000E+13      .000         .00
O+C2H2<=>H+HCCO                          1.350E+07     2.000     1900.00
```

```
O+C2H2<=>OH+C2H                          4.600E+19   -1.410   28950.00
O+C2H2<=>CO+CH2                          6.940E+06    2.000    1900.00
O+C2H3<=>H+CH2CO                         3.000E+13     .000        .00
O+C2H4<=>CH3+HCO                         1.250E+07    1.830     220.00
O+C2H5<=>CH3+CH2O                        2.240E+13     .000        .00
O+C2H6<=>OH+C2H5                         8.980E+07    1.920    5690.00
O+HCCO<=>H+2CO                           1.000E+14     .000        .00
O+CH2CO<=>OH+HCCO                        1.000E+13     .000    8000.00
O+CH2CO<=>CH2+CO2                        1.750E+12     .000    1350.00
O2+CO<=>O+CO2                            2.500E+12     .000   47800.00
O2+CH2O<=>HO2+HCO                        1.000E+14     .000   40000.00
H+O2+M<=>HO2+M                           2.800E+18    -.860        .00
O2/ .00/ H2O/ .00/ CO/ .75/ CO2/1.50/ C2H6/1.50/ N2/ .00/ !AR/ .00/
H+2O2<=>HO2+O2                           2.080E+19   -1.240        .00
H+O2+H2O<=>HO2+H2O                       11.26E+18    -.760        .00
H+O2+N2<=>HO2+N2                         2.600E+19   -1.240        .00
!H+O2+AR<=>HO2+AR                         7.000E+17    -.800        .00
H+O2<=>O+OH                              2.650E+16    -.6707  17041.00
2H+M<=>H2+M                              1.000E+18   -1.000        .00
H2/ .00/ H2O/ .00/ CH4/2.00/ CO2/ .00/ C2H6/3.00/ !AR/ .63/
2H+H2<=>2H2                              9.000E+16    -.600        .00
2H+H2O<=>H2+H2O                          6.000E+19   -1.250        .00
2H+CO2<=>H2+CO2                          5.500E+20   -2.000        .00
H+OH+M<=>H2O+M                           2.200E+22   -2.000        .00
H2/ .73/ H2O/3.65/ CH4/2.00/ C2H6/3.00/ !AR/ .38/
H+HO2<=>O+H2O                            3.970E+12     .000     671.00
H+HO2<=>O2+H2                            4.480E+13     .000    1068.00
H+HO2<=>2OH                              0.840E+14     .000     635.00
H+H2O2<=>HO2+H2                          1.210E+07    2.000    5200.00
H+H2O2<=>OH+H2O                          1.000E+13     .000    3600.00
H+CH<=>C+H2                              1.650E+14     .000        .00
H+CH2(+M)<=>CH3(+M)                      6.000E+14     .000        .00
     LOW  /   1.040E+26    -2.760    1600.00/
     TROE/    .5620   91.00   5836.00   8552.00/
H2/2.00/ H2O/6.00/ CH4/2.00/ CO/1.50/ CO2/2.00/ C2H6/3.00/ !AR/ .70/
H+CH2(S)<=>CH+H2                         3.000E+13     .000        .00
H+CH3(+M)<=>CH4(+M)                      13.90E+15    -.534     536.00
     LOW  /   2.620E+33    -4.760    2440.00/
     TROE/    .7830   74.00   2941.00   6964.00 /
H2/2.00/ H2O/6.00/ CH4/3.00/ CO/1.50/ CO2/2.00/ C2H6/3.00/ !AR/ .70/
H+CH4<=>CH3+H2                           6.600E+08    1.620   10840.00
H+HCO(+M)<=>CH2O(+M)                     1.090E+12     .480    -260.00
     LOW  /   2.470E+24    -2.570     425.00/
     TROE/    .7824  271.00   2755.00   6570.00 /
H2/2.00/ H2O/6.00/ CH4/2.00/ CO/1.50/ CO2/2.00/ C2H6/3.00/ !AR/ .70/
H+HCO<=>H2+CO                            7.340E+13     .000        .00
H+CH2O(+M)<=>CH2OH(+M)                   5.400E+11     .454    3600.00
     LOW  /   1.270E+32    -4.820    6530.00/
     TROE/    .7187  103.00   1291.00   4160.00 /
H2/2.00/ H2O/6.00/ CH4/2.00/ CO/1.50/ CO2/2.00/ C2H6/3.00/
H+CH2O(+M)<=>CH3O(+M)                    5.400E+11     .454    2600.00
     LOW  /   2.200E+30    -4.800    5560.00/
     TROE/    .7580   94.00   1555.00   4200.00 /
H2/2.00/ H2O/6.00/ CH4/2.00/ CO/1.50/ CO2/2.00/ C2H6/3.00/
H+CH2O<=>HCO+H2                          5.740E+07    1.900    2742.00
H+CH2OH(+M)<=>CH3OH(+M)                  1.055E+12     .500      86.00
     LOW  /   4.360E+31    -4.650    5080.00/
     TROE/    .600   100.00   90000.0   10000.0 /
H2/2.00/ H2O/6.00/ CH4/2.00/ CO/1.50/ CO2/2.00/ C2H6/3.00/
H+CH2OH<=>H2+CH2O                        2.000E+13     .000        .00
H+CH2OH<=>OH+CH3                         1.650E+11     .650    -284.00
H+CH2OH<=>CH2(S)+H2O                     3.280E+13    -.090     610.00
H+CH3O(+M)<=>CH3OH(+M)                   2.430E+12     .515      50.00
     LOW  /   4.660E+41    -7.440   14080.0/
     TROE/    .700   100.00   90000.0 10000.00 /
H2/2.00/ H2O/6.00/ CH4/2.00/ CO/1.50/ CO2/2.00/ C2H6/3.00/
H+CH3O<=>H+CH2OH                         4.150E+07    1.630    1924.00
H+CH3O<=>H2+CH2O                         2.000E+13     .000        .00
H+CH3O<=>OH+CH3                          1.500E+12     .500    -110.00
H+CH3O<=>CH2(S)+H2O                      2.620E+14    -.230    1070.00
H+CH3OH<=>CH2OH+H2                       1.700E+07    2.100    4870.00
H+CH3OH<=>CH3O+H2                        4.200E+06    2.100    4870.00
H+C2H(+M)<=>C2H2(+M)                     1.000E+17   -1.000        .00
```

```
     LOW  /   3.750E+33    −4.800    1900.00/
     TROE/    .6464   132.00   1315.00   5566.00 /
H2/2.00/ H2O/6.00/ CH4/2.00/ CO/1.50/ CO2/2.00/ C2H6/3.00/ !AR/ .70/
H+C2H2(+M)<=>C2H3(+M)                    5.600E+12     .000     2400.00
     LOW  /   3.800E+40    −7.270    7220.00/
     TROE/    .7507    98.50   1302.00   4167.00 /
H2/2.00/ H2O/6.00/ CH4/2.00/ CO/1.50/ CO2/2.00/ C2H6/3.00/ !AR/ .70/
H+C2H3(+M)<=>C2H4(+M)                    6.080E+12     .270      280.00
     LOW  /   1.400E+30    −3.860    3320.00/
     TROE/    .7820   207.50   2663.00   6095.00 /
H2/2.00/ H2O/6.00/ CH4/2.00/ CO/1.50/ CO2/2.00/ C2H6/3.00/ !AR/ .70/
H+C2H3<=>H2+C2H2                         3.000E+13     .000         .00
H+C2H4(+M)<=>C2H5(+M)                    0.540E+12     .454     1820.00
     LOW  /   0.600E+42    −7.620    6970.00/
     TROE/    .9753   210.00    984.00   4374.00 /
H2/2.00/ H2O/6.00/ CH4/2.00/ CO/1.50/ CO2/2.00/ C2H6/3.00/ !AR/ .70/
H+C2H4<=>C2H3+H2                         1.325E+06    2.530    12240.00
H+C2H5(+M)<=>C2H6(+M)                    5.210E+17    −.990     1580.00
     LOW  /   1.990E+41    −7.080    6685.00/
     TROE/    .8422   125.00   2219.00   6882.00 /
H2/2.00/ H2O/6.00/ CH4/2.00/ CO/1.50/ CO2/2.00/ C2H6/3.00/ !AR/ .70/
H+C2H5<=>H2+C2H4                         2.000E+12     .000         .00
H+C2H6<=>C2H5+H2                         1.150E+08    1.900     7530.00
H+HCCO<=>CH2(S)+CO                       1.000E+14     .000         .00
H+CH2CO<=>HCCO+H2                        5.000E+13     .000     8000.00
H+CH2CO<=>CH3+CO                         1.130E+13     .000     3428.00
H+HCCOH<=>H+CH2CO                        1.000E+13     .000         .00
H2+CO(+M)<=>CH2O(+M)                     4.300E+07    1.500    79600.00
     LOW  /   5.070E+27    −3.420   84350.00/
     TROE/    .9320   197.00   1540.00  10300.00 /
H2/2.00/ H2O/6.00/ CH4/2.00/ CO/1.50/ CO2/2.00/ C2H6/3.00/ !AR/ .70/
OH+H2<=>H+H2O                            2.160E+08    1.510     3430.00
2OH(+M)<=>H2O2(+M)                       7.400E+13    −.370         .00
     LOW  /   2.300E+18     −.900   −1700.00/
     TROE/    .7346    94.00   1756.00   5182.00 /
H2/2.00/ H2O/6.00/ CH4/2.00/ CO/1.50/ CO2/2.00/ C2H6/3.00/ !AR/ .70/
2OH<=>O+H2O                              3.570E+04    2.400    −2110.00
OH+HO2<=>O2+H2O                          1.450E+13     .000     −500.00
 DUPLICATE
OH+H2O2<=>HO2+H2O                        2.000E+12     .000      427.00
 DUPLICATE
OH+H2O2<=>HO2+H2O                        1.700E+18     .000    29410.00
 DUPLICATE
OH+C<=>H+CO                              5.000E+13     .000         .00
OH+CH<=>H+HCO                            3.000E+13     .000         .00
OH+CH2<=>H+CH2O                          2.000E+13     .000         .00
OH+CH2<=>CH+H2O                          1.130E+07    2.000     3000.00
OH+CH2(S)<=>H+CH2O                       3.000E+13     .000         .00
OH+CH3(+M)<=>CH3OH(+M)                   2.790E+18   −1.430     1330.00
     LOW  /   4.000E+36    −5.920    3140.00/
     TROE/    .4120   195.0    5900.00   6394.00/
H2/2.00/ H2O/6.00/ CH4/2.00/ CO/1.50/ CO2/2.00/ C2H6/3.00/
OH+CH3<=>CH2+H2O                         5.600E+07    1.600     5420.00
OH+CH3<=>CH2(S)+H2O                      6.440E+17   −1.340     1417.00
OH+CH4<=>CH3+H2O                         1.000E+08    1.600     3120.00
OH+CO<=>H+CO2                            4.760E+07    1.228       70.00
OH+HCO<=>H2O+CO                          5.000E+13     .000         .00
OH+CH2O<=>HCO+H2O                        3.430E+09    1.180     −447.00
OH+CH2OH<=>H2O+CH2O                      5.000E+12     .000         .00
OH+CH3O<=>H2O+CH2O                       5.000E+12     .000         .00
OH+CH3OH<=>CH2OH+H2O                     1.440E+06    2.000     −840.00
OH+CH3OH<=>CH3O+H2O                      6.300E+06    2.000     1500.00
OH+C2H<=>H+HCCO                          2.000E+13     .000         .00
OH+C2H2<=>H+CH2CO                        2.180E−04    4.500    −1000.00
OH+C2H2<=>H+HCCOH                        5.040E+05    2.300    13500.00
OH+C2H2<=>C2H+H2O                        3.370E+07    2.000    14000.00
OH+C2H2<=>CH3+CO                         4.830E−04    4.000    −2000.00
OH+C2H3<=>H2O+C2H2                       5.000E+12     .000         .00
OH+C2H4<=>C2H3+H2O                       3.600E+06    2.000     2500.00
OH+C2H6<=>C2H5+H2O                       3.540E+06    2.120      870.00
OH+CH2CO<=>HCCO+H2O                      7.500E+12     .000     2000.00
2HO2<=>O2+H2O2                           1.300E+11     .000    −1630.00
 DUPLICATE
```

```
2HO2<=>O2+H2O2                           4.200E+14     .000   12000.00
 DUPLICATE
HO2+CH2<=>OH+CH2O                        2.000E+13     .000        .00
HO2+CH3<=>O2+CH4                         1.000E+12     .000        .00
HO2+CH3<=>OH+CH3O                        3.780E+13     .000        .00
HO2+CO<=>OH+CO2                          1.500E+14     .000   23600.00
HO2+CH2O<=>HCO+H2O2                      5.600E+06    2.000   12000.00
C+O2<=>O+CO                              5.800E+13     .000     576.00
C+CH2<=>H+C2H                            5.000E+13     .000        .00
C+CH3<=>H+C2H2                           5.000E+13     .000        .00
CH+O2<=>O+HCO                            6.710E+13     .000        .00
CH+H2<=>H+CH2                            1.080E+14     .000    3110.00
CH+H2O<=>H+CH2O                          5.710E+12     .000    -755.00
CH+CH2<=>H+C2H2                          4.000E+13     .000        .00
CH+CH3<=>H+C2H3                          3.000E+13     .000        .00
CH+CH4<=>H+C2H4                          6.000E+13     .000        .00
CH+CO(+M)<=>HCCO(+M)                     5.000E+13     .000        .00
     LOW  /  2.690E+28   -3.740    1936.00/
     TROE/   .5757   237.00   1652.00   5069.00 /
H2/2.00/ H2O/6.00/ CH4/2.00/ CO/1.50/ CO2/2.00/ C2H6/3.00/ !AR/ .70/
CH+CO2<=>HCO+CO                          1.900E+14     .000   15792.00
CH+CH2O<=>H+CH2CO                        9.460E+13     .000    -515.00
CH+HCCO<=>CO+C2H2                        5.000E+13     .000        .00
CH2+O2=>OH+H+CO                          5.000E+12     .000    1500.00
CH2+H2<=>H+CH3                           5.000E+05    2.000    7230.00
2CH2<=>H2+C2H2                           1.600E+15     .000   11944.00
CH2+CH3<=>H+C2H4                         4.000E+13     .000        .00
CH2+CH4<=>2CH3                           2.460E+06    2.000    8270.00
CH2+CO(+M)<=>CH2CO(+M)                   8.100E+11     .500    4510.00
     LOW  /  2.690E+33   -5.110    7095.00/
     TROE/   .5907   275.00   1226.00   5185.00 /
H2/2.00/ H2O/6.00/ CH4/2.00/ CO/1.50/ CO2/2.00/ C2H6/3.00/ !AR/ .70/
CH2+HCCO<=>C2H3+CO                       3.000E+13     .000        .00
CH2(S)+N2<=>CH2+N2                       1.500E+13     .000     600.00
!CH2(S)+AR<=>CH2+AR                       9.000E+12     .000     600.00
CH2(S)+O2<=>H+OH+CO                      2.800E+13     .000        .00
CH2(S)+O2<=>CO+H2O                       1.200E+13     .000        .00
CH2(S)+H2<=>CH3+H                        7.000E+13     .000        .00
CH2(S)+H2O(+M)<=>CH3OH(+M)               4.820E+17   -1.160    1145.00
     LOW  /  1.880E+38   -6.360    5040.00/
     TROE/   .6027   208.00   3922.00   10180.0 /
H2/2.00/ H2O/6.00/ CH4/2.00/ CO/1.50/ CO2/2.00/ C2H6/3.00/
CH2(S)+H2O<=>CH2+H2O                     3.000E+13     .000        .00
CH2(S)+CH3<=>H+C2H4                      1.200E+13     .000    -570.00
CH2(S)+CH4<=>2CH3                        1.600E+13     .000    -570.00
CH2(S)+CO<=>CH2+CO                       9.000E+12     .000        .00
CH2(S)+CO2<=>CH2+CO2                     7.000E+12     .000        .00
CH2(S)+CO2<=>CO+CH2O                     1.400E+13     .000        .00
CH2(S)+C2H6<=>CH3+C2H5                   4.000E+13     .000    -550.00
CH3+O2<=>O+CH3O                          3.560E+13     .000   30480.00
CH3+O2<=>OH+CH2O                         2.310E+12     .000   20315.00
CH3+H2O2<=>HO2+CH4                       2.450E+04    2.470    5180.00
2CH3(+M)<=>C2H6(+M)                      6.770E+16   -1.180     654.00
     LOW  /  3.400E+41   -7.030    2762.00/
     TROE/   .6190   73.20   1180.00   9999.00 /
H2/2.00/ H2O/6.00/ CH4/2.00/ CO/1.50/ CO2/2.00/ C2H6/3.00/ !AR/ .70/
2CH3<=>H+C2H5                            6.840E+12     .100   10600.00
CH3+HCO<=>CH4+CO                         2.648E+13     .000        .00
CH3+CH2O<=>HCO+CH4                       3.320E+03    2.810    5860.00
CH3+CH3OH<=>CH2OH+CH4                    3.000E+07    1.500    9940.00
CH3+CH3OH<=>CH3O+CH4                     1.000E+07    1.500    9940.00
CH3+C2H4<=>C2H3+CH4                      2.270E+05    2.000    9200.00
CH3+C2H6<=>C2H5+CH4                      6.140E+06    1.740   10450.00
HCO+H2O<=>H+CO+H2O                       1.500E+18   -1.000   17000.00
HCO+M<=>H+CO+M                           1.870E+17   -1.000   17000.00
H2/2.00/ H2O/ .00/ CH4/2.00/ CO/1.50/ CO2/2.00/ C2H6/3.00/
HCO+O2<=>HO2+CO                          13.45E+12     .000     400.00
CH2OH+O2<=>HO2+CH2O                      1.800E+13     .000     900.00
CH3O+O2<=>HO2+CH2O                       4.280E-13    7.600   -3530.00
C2H+O2<=>HCO+CO                          1.000E+13     .000    -755.00
C2H+H2<=>H+C2H2                          5.680E+10    0.900    1993.00
C2H3+O2<=>HCO+CH2O                       4.580E+16   -1.390    1015.00
C2H4(+M)<=>H2+C2H2(+M)                   8.000E+12     .440   86770.00
```

```
     LOW  /   1.580E+51    −9.300   97800.00/
     TROE/    .7345    180.00    1035.00    5417.00  /
H2/2.00/ H2O/6.00/ CH4/2.00/ CO/1.50/ CO2/2.00/ C2H6/3.00/ !AR/ .70/
C2H5+O2<=>HO2+C2H4                        8.400E+11     .000     3875.00
HCCO+O2<=>OH+2CO                          3.200E+12     .000      854.00
2HCCO<=>2CO+C2H2                          1.000E+13     .000         .00
N+NO<=>N2+O                               2.700E+13     .000      355.00
N+O2<=>NO+O                               9.000E+09    1.000     6500.00
N+OH<=>NO+H                               3.360E+13     .000      385.00
N2O+O<=>N2+O2                             1.400E+12     .000    10810.00
N2O+O<=>2NO                               2.900E+13     .000    23150.00
N2O+H<=>N2+OH                             3.870E+14     .000    18880.00
N2O+OH<=>N2+HO2                           2.000E+12     .000    21060.00
N2O(+M)<=>N2+O(+M)                        7.910E+10     .000    56020.00
     LOW  /   6.370E+14      .000    56640.00/
H2/2.00/ H2O/6.00/ CH4/2.00/ CO/1.50/ CO2/2.00/ C2H6/3.00/ !AR/ .625/
HO2+NO<=>NO2+OH                           2.110E+12     .000     −480.00
NO+O+M<=>NO2+M                            1.060E+20   −1.410         .00
H2/2.00/ H2O/6.00/ CH4/2.00/ CO/1.50/ CO2/2.00/ C2H6/3.00/ !AR/ .70/
NO2+O<=>NO+O2                             3.900E+12     .000     −240.00
NO2+H<=>NO+OH                             1.320E+14     .000      360.00
NH+O<=>NO+H                               4.000E+13     .000         .00
NH+H<=>N+H2                               3.200E+13     .000      330.00
NH+OH<=>HNO+H                             2.000E+13     .000         .00
NH+OH<=>N+H2O                             2.000E+09    1.200         .00
NH+O2<=>HNO+O                             4.610E+05    2.000     6500.00
NH+O2<=>NO+OH                             1.280E+06    1.500      100.00
NH+N<=>N2+H                               1.500E+13     .000         .00
NH+H2O<=>HNO+H2                           2.000E+13     .000    13850.00
NH+NO<=>N2+OH                             2.160E+13    −.230         .00
NH+NO<=>N2O+H                             3.650E+14    −.450         .00
NH2+O<=>OH+NH                             3.000E+12     .000         .00
NH2+O<=>H+HNO                             3.900E+13     .000         .00
NH2+H<=>NH+H2                             4.000E+13     .000     3650.00
NH2+OH<=>NH+H2O                           9.000E+07    1.500     −460.00
NNH<=>N2+H                                3.300E+08     .000         .00
NNH+M<=>N2+H+M                            1.300E+14    −.110     4980.00
H2/2.00/ H2O/6.00/ CH4/2.00/ CO/1.50/ CO2/2.00/ C2H6/3.00/ !AR/ .70/
NNH+O2<=>HO2+N2                           5.000E+12     .000         .00
NNH+O<=>OH+N2                             2.500E+13     .000         .00
NNH+O<=>NH+NO                             7.000E+13     .000         .00
NNH+H<=>H2+N2                             5.000E+13     .000         .00
NNH+OH<=>H2O+N2                           2.000E+13     .000         .00
NNH+CH3<=>CH4+N2                          2.500E+13     .000         .00
H+NO+M<=>HNO+M                            4.480E+19   −1.320      740.00
H2/2.00/ H2O/6.00/ CH4/2.00/ CO/1.50/ CO2/2.00/ C2H6/3.00/ !AR/ .70/
HNO+O<=>NO+OH                             2.500E+13     .000         .00
HNO+H<=>H2+NO                             9.000E+11     .720      660.00
HNO+OH<=>NO+H2O                           1.300E+07    1.900     −950.00
HNO+O2<=>HO2+NO                           1.000E+13     .000    13000.00
CN+O<=>CO+N                               7.700E+13     .000         .00
CN+OH<=>NCO+H                             4.000E+13     .000         .00
CN+H2O<=>HCN+OH                           8.000E+12     .000     7460.00
CN+O2<=>NCO+O                             6.140E+12     .000     −440.00
CN+H2<=>HCN+H                             2.950E+05    2.450     2240.00
NCO+O<=>NO+CO                             2.350E+13     .000         .00
NCO+H<=>NH+CO                             5.400E+13     .000         .00
NCO+OH<=>NO+H+CO                          0.250E+13     .000         .00
NCO+N<=>N2+CO                             2.000E+13     .000         .00
NCO+O2<=>NO+CO2                           2.000E+12     .000    20000.00
NCO+M<=>N+CO+M                            3.100E+14     .000    54050.00
H2/2.00/ H2O/6.00/ CH4/2.00/ CO/1.50/ CO2/2.00/ C2H6/3.00/ !AR/ .70/
NCO+NO<=>N2O+CO                           1.900E+17   −1.520      740.00
NCO+NO<=>N2+CO2                           3.800E+18   −2.000      800.00
HCN+M<=>H+CN+M                            1.040E+29   −3.300   126600.00
H2/2.00/ H2O/6.00/ CH4/2.00/ CO/1.50/ CO2/2.00/ C2H6/3.00/ !AR/ .70/
HCN+O<=>NCO+H                             2.030E+04    2.640     4980.00
HCN+O<=>NH+CO                             5.070E+03    2.640     4980.00
HCN+O<=>CN+OH                             3.910E+09    1.580    26600.00
HCN+OH<=>HOCN+H                           1.100E+06    2.030    13370.00
HCN+OH<=>HNCO+H                           4.400E+03    2.260     6400.00
HCN+OH<=>NH2+CO                           1.600E+02    2.560     9000.00
H+HCN(+M)<=>H2CN(+M)                      3.300E+13     .000         .00
```

```
     LOW  /   1.400E+26    -3.400      1900.00/
H2/2.00/ H2O/6.00/ CH4/2.00/ CO/1.50/ CO2/2.00/ C2H6/3.00/ !AR/ .70/
H2CN+N<=>N2+CH2                          6.000E+13      .000      400.00
C+N2<=>CN+N                              6.300E+13      .000    46020.00
CH+N2<=>HCN+N                            3.120E+09     0.880    20130.00
CH+N2(+M)<=>HCNN(+M)                     3.100E+12      .150         .00
    LOW   /   1.300E+25    -3.160      740.00/
    TROE/    .6670    235.00   2117.00   4536.00  /
H2/2.00/ H2O/6.00/ CH4/2.00/ CO/1.50/ CO2/2.00/ C2H6/3.00/ !AR/ 1.0/
CH2+N2<=>HCN+NH                          1.000E+13      .000    74000.00
CH2(S)+N2<=>NH+HCN                       1.000E+11      .000    65000.00
C+NO<=>CN+O                              1.900E+13      .000         .00
C+NO<=>CO+N                              2.900E+13      .000         .00
CH+NO<=>HCN+O                            4.100E+13      .000         .00
CH+NO<=>H+NCO                            1.620E+13      .000         .00
CH+NO<=>N+HCO                            2.460E+13      .000         .00
CH2+NO<=>H+HNCO                          3.100E+17    -1.380     1270.00
CH2+NO<=>OH+HCN                          2.900E+14     -.690      760.00
CH2+NO<=>H+HCNO                          3.800E+13     -.360      580.00
CH2(S)+NO<=>H+HNCO                       3.100E+17    -1.380     1270.00
CH2(S)+NO<=>OH+HCN                       2.900E+14     -.690      760.00
CH2(S)+NO<=>H+HCNO                       3.800E+13     -.360      580.00
CH3+NO<=>HCN+H2O                         9.600E+13      .000    28800.00
CH3+NO<=>H2CN+OH                         1.000E+12      .000    21750.00
HCNN+O<=>CO+H+N2                         2.200E+13      .000         .00
HCNN+O<=>HCN+NO                          2.000E+12      .000         .00
HCNN+O2<=>O+HCO+N2                       1.200E+13      .000         .00
HCNN+OH<=>H+HCO+N2                       1.200E+13      .000         .00
HCNN+H<=>CH2+N2                          1.000E+14      .000         .00
HNCO+O<=>NH+CO2                          9.800E+07     1.410     8500.00
HNCO+O<=>HNO+CO                          1.500E+08     1.570    44000.00
HNCO+O<=>NCO+OH                          2.200E+06     2.110    11400.00
HNCO+H<=>NH2+CO                          2.250E+07     1.700     3800.00
HNCO+H<=>H2+NCO                          1.050E+05     2.500    13300.00
HNCO+OH<=>NCO+H2O                        3.300E+07     1.500     3600.00
HNCO+OH<=>NH2+CO2                        3.300E+06     1.500     3600.00
HNCO+M<=>NH+CO+M                         1.180E+16      .000    84720.00
H2/2.00/ H2O/6.00/ CH4/2.00/ CO/1.50/ CO2/2.00/ C2H6/3.00/ !AR/ .70/
HCNO+H<=>H+HNCO                          2.100E+15     -.690     2850.00
HCNO+H<=>OH+HCN                          2.700E+11      .180     2120.00
HCNO+H<=>NH2+CO                          1.700E+14     -.750     2890.00
HOCN+H<=>H+HNCO                          2.000E+07     2.000     2000.00
HCCO+NO<=>HCNO+CO                        0.900E+13      .000         .00
CH3+N<=>H2CN+H                           6.100E+14     -.310      290.00
CH3+N<=>HCN+H2                           3.700E+12      .150      -90.00
NH3+H<=>NH2+H2                           5.400E+05     2.400     9915.00
NH3+OH<=>NH2+H2O                         5.000E+07     1.600      955.00
NH3+O<=>NH2+OH                           9.400E+06     1.940     6460.00
NH+CO2<=>HNO+CO                          1.000E+13      .000    14350.00
CN+NO2<=>NCO+NO                          6.160E+15    -0.752      345.00
NCO+NO2<=>N2O+CO2                        3.250E+12      .000     -705.00
N+CO2<=>NO+CO                            3.000E+12      .000    11300.00
O+CH3=>H+H2+CO                           3.370E+13      .000         .00
O+C2H4<=>H+CH2CHO                        6.700E+06     1.830      220.00
O+C2H5<=>H+CH3CHO                        1.096E+14      .000         .00
OH+HO2<=>O2+H2O                          0.500E+16      .000    17330.00
  DUPLICATE
OH+CH3=>H2+CH2O                          8.000E+09      .500    -1755.00
CH+H2(+M)<=>CH3(+M)                      1.970E+12      .430     -370.00
   LOW/  4.820E+25   -2.80   590.0  /
   TROE/  .578   122.0   2535.0   9365.0  /
H2/2.00/ H2O/6.00/ CH4/2.00/ CO/1.50/ CO2/2.00/ C2H6/3.00/ !AR/ .70/
CH2+O2=>2H+CO2                           5.800E+12      .000     1500.00
CH2+O2<=>O+CH2O                          2.400E+12      .000     1500.00
CH2+CH2=>2H+C2H2                         2.000E+14      .000    10989.00
CH2(S)+H2O=>H2+CH2O                      6.820E+10      .250     -935.00
C2H3+O2<=>O+CH2CHO                       3.030E+11      .290       11.00
C2H3+O2<=>HO2+C2H2                       1.337E+06     1.610     -384.00
O+CH3CHO<=>OH+CH2CHO                     2.920E+12      .000     1808.00
O+CH3CHO=>OH+CH3+CO                      2.920E+12      .000     1808.00
O2+CH3CHO=>HO2+CH3+CO                    3.010E+13      .000    39150.00
H+CH3CHO<=>CH2CHO+H2                     2.050E+09     1.160     2405.00
H+CH3CHO=>CH3+H2+CO                      2.050E+09     1.160     2405.00
```

```
OH+CH3CHO=>CH3+H2O+CO                    2.343E+10    0.730   -1113.00
HO2+CH3CHO=>CH3+H2O2+CO                  3.010E+12     .000   11923.00
CH3+CH3CHO=>CH3+CH4+CO                   2.720E+06    1.770    5920.00
H+CH2CO(+M)<=>CH2CHO(+M)                 4.865E+11    0.422   -1755.00
    LOW/ 1.012E+42   -7.63   3854.0/
    TROE/ 0.465   201.0   1773.0   5333.0 /
H2/2.00/ H2O/6.00/ CH4/2.00/ CO/1.50/ CO2/2.00/ C2H6/3.00/ !AR/ .70/
O+CH2CHO=>H+CH2+CO2                      1.500E+14     .000        .00
O2+CH2CHO=>OH+CO+CH2O                    1.810E+10     .000        .00
O2+CH2CHO=>OH+2HCO                       2.350E+10     .000        .00
H+CH2CHO<=>CH3+HCO                       2.200E+13     .000        .00
H+CH2CHO<=>CH2CO+H2                      1.100E+13     .000        .00
OH+CH2CHO<=>H2O+CH2CO                    1.200E+13     .000        .00
OH+CH2CHO<=>HCO+CH2OH                    3.010E+13     .000        .00
!CH3+C2H5(+M)<=>C3H8(+M)                  .9430E+13     .000        .00
!     LOW/ 2.710E+74   -16.82   13065.0 /
!     TROE/ .1527   291.0   2742.0   7748.0 /
!H2/2.00/ H2O/6.00/ CH4/2.00/ CO/1.50/ CO2/2.00/ C2H6/3.00/ !AR/ .70/
!O+C3H8<=>OH+C3H7                         1.930E+05    2.680    3716.00
!H+C3H8<=>C3H7+H2                         1.320E+06    2.540    6756.00
!OH+C3H8<=>C3H7+H2O                       3.160E+07    1.800     934.00
!C3H7+H2O2<=>HO2+C3H8                     3.780E+02    2.720    1500.00
!CH3+C3H8<=>C3H7+CH4                      0.903E+00    3.650    7154.00
!CH3+C2H4(+M)<=>C3H7(+M)                  2.550E+06    1.600    5700.00
!      LOW/ 3.00E+63   -14.6   18170./
!      TROE/ .1894   277.0   8748.0   7891.0 /
!H2/2.00/ H2O/6.00/ CH4/2.00/ CO/1.50/ CO2/2.00/ C2H6/3.00/ !AR/ .70/
!O+C3H7<=>C2H5+CH2O                       9.640E+13     .000        .00
!H+C3H7(+M)<=>C3H8(+M)                    3.613E+13     .000        .00
!      LOW/ 4.420E+61   -13.545   11357.0/
!      TROE/ .315   369.0   3285.0   6667.0 /
!H2/2.00/ H2O/6.00/ CH4/2.00/ CO/1.50/ CO2/2.00/ C2H6/3.00/ !AR/ .70/
!H+C3H7<=>CH3+C2H5                        4.060E+06    2.190     890.00
!OH+C3H7<=>C2H5+CH2OH                     2.410E+13     .000        .00
!HO2+C3H7<=>O2+C3H8                       2.550E+10    0.255    -943.00
!HO2+C3H7=>OH+C2H5+CH2O                   2.410E+13     .000        .00
!CH3+C3H7<=>2C2H5                         1.927E+13   -0.320        .00
END
```

Thermodynamic data

```
THERMO
   300.000   1000.000   5000.000
! GRI-Mech Version 3.0 Thermodynamics released 7/30/99
! NASA Polynomial format for CHEMKIN-II
! see README file for disclaimer
O                 L 1/90O   1               G    200.000   3500.000   1000.000      1
 2.56942078E+00-8.59741137E-05 4.19484589E-08-1.00177799E-11 1.22833691E-15    2
 2.92175791E+04 4.78433864E+00 3.16826710E+00-3.27931884E-03 6.64306396E-06    3
-6.12806624E-09 2.11265971E-12 2.91222592E+04 2.05193346E+00                   4
O2                TPIS89O   2               G    200.000   3500.000   1000.000      1
 3.28253784E+00 1.48308754E-03-7.57966669E-07 2.09470555E-10-2.16717794E-14    2
-1.08845772E+03 5.45323129E+00 3.78245636E+00-2.99673416E-03 9.84730201E-06    3
-9.68129509E-09 3.24372837E-12-1.06394356E+03 3.65767573E+00                   4
H                 L 7/88H   1               G    200.000   3500.000   1000.000      1
 2.50000001E+00-2.30842973E-11 1.61561948E-14-4.73515235E-18 4.98197357E-22    2
 2.54736599E+04-4.46682914E-01 2.50000000E+00 7.05332819E-13-1.99591964E-15    3
 2.30081632E-18-9.27732332E-22 2.54736599E+04-4.46682853E-01                   4
H2                TPIS78H   2               G    200.000   3500.000   1000.000      1
 3.33727920E+00-4.94024731E-05 4.99456778E-07-1.79566394E-10 2.00255376E-14    2
-9.50158922E+02-3.20502331E+00 2.34433112E+00 7.98052075E-03-1.94781510E-05    3
 2.01572094E-08-7.37611761E-12-9.17935173E+02 6.83010238E-01                   4
OH                RUS 78O   1H   1          G    200.000   3500.000   1000.000      1
 3.09288767E+00 5.48429716E-04 1.26505228E-07-8.79461556E-11 1.17412376E-14    2
 3.85865700E+03 4.47669610E+00 3.99201543E+00-2.40131752E-03 4.61793841E-06    3
-3.88113333E-09 1.36411470E-12 3.61508056E+03-1.03925458E-01                   4
H2O               L 8/89H   2O   1          G    200.000   3500.000   1000.000      1
 3.03399249E+00 2.17691804E-03-1.64072518E-07-9.70419870E-11 1.68200992E-14    2
-3.00042971E+04 4.96677010E+00 4.19864056E+00-2.03643410E-03 6.52040211E-06    3
```

```
-5.48797062E-09 1.77197817E-12-3.02937267E+04-8.49032208E-01                   4
HO2               L 5/89H   1O   2          G   200.000  3500.000  1000.000    1
 4.01721090E+00 2.23982013E-03-6.33658150E-07 1.14246370E-10-1.07908535E-14    2
 1.11856713E+02 3.78510215E+00 4.30179801E+00-4.74912051E-03 2.11582891E-05    3
-2.42763894E-08 9.29225124E-12 2.94808040E+02 3.71666245E+00                   4
H2O2              L 7/88H   2O   2          G   200.000  3500.000  1000.000    1
 4.16500285E+00 4.90831694E-03-1.90139225E-06 3.71185986E-10-2.87908305E-14    2
-1.78617877E+04 2.91615662E+00 4.27611269E+00-5.42822417E-04 1.67335701E-05    3
-2.15770813E-08 8.62454363E-12-1.77025821E+04 3.43505074E+00                   4
C                 L11/88C   1               G   200.000  3500.000  1000.000    1
 2.49266888E+00 4.79889284E-05-7.24335020E-08 3.74291029E-11-4.87277893E-15    2
 8.54512953E+04 4.80150373E+00 2.55423955E+00-3.21537724E-04 7.33792245E-07    3
-7.32234889E-10 2.66521446E-13 8.54438832E+04 4.53130848E+00                   4
CH                TPIS79C   1H   1          G   200.000  3500.000  1000.000    1
 2.87846473E+00 9.70913681E-04 1.44445655E-07-1.30687849E-10 1.76079383E-14    2
 7.10124364E+04 5.48497999E+00 3.48981665E+00 3.23835541E-04-1.68899065E-06    3
 3.16217327E-09-1.40609067E-12 7.07972934E+04 2.08401108E+00                   4
CH2               L S/93C   1H   2          G   200.000  3500.000  1000.000    1
 2.87410113E+00 3.65639292E-03-1.40894597E-06 2.60179549E-10-1.87727567E-14    2
 4.62636040E+04 6.17119324E+00 3.76267867E+00 9.68872143E-04 2.79489841E-06    3
-3.85091153E-09 1.68741719E-12 4.60040401E+04 1.56253185E+00                   4
CH2(S)            L S/93C   1H   2          G   200.000  3500.000  1000.000    1
 2.29203842E+00 4.65588637E-03-2.01191947E-06 4.17906000E-10-3.39716365E-14    2
 5.09259997E+04 8.62650169E+00 4.19860411E+00-2.36661419E-03 8.23296220E-06    3
-6.68815981E-09 1.94314737E-12 5.04968163E+04-7.69118967E-01                   4
CH3               L11/89C   1H   3          G   200.000  3500.000  1000.000    1
 2.28571772E+00 7.23990037E-03-2.98714348E-06 5.95684644E-10-4.67154394E-14    2
 1.67755843E+04 8.48007179E+00 3.67359040E+00 2.01095175E-03 5.73021856E-06    3
-6.87117425E-09 2.54385734E-12 1.64449988E+04 1.60456433E+00                   4
CH4               L 8/88C   1H   4          G   200.000  3500.000  1000.000    1
 7.48514950E-02 1.33909467E-02-5.73285809E-06 1.22292535E-09-1.01815230E-13    2
-9.46834459E+03 1.84373180E+01 5.14987613E+00-1.36709788E-02 4.91800599E-05    3
-4.84743026E-08 1.66693956E-11-1.02466476E+04-4.64130376E+00                   4
CO                TPIS79C   1O   1          G   200.000  3500.000  1000.000    1
 2.71518561E+00 2.06252743E-03-9.98825771E-07 2.30053008E-10-2.03647716E-14    2
-1.41518724E+04 7.81868772E+00 3.57953347E+00-6.10353680E-04 1.01681433E-06    3
 9.07005884E-10-9.04424499E-13-1.43440860E+04 3.50840928E+00                   4
CO2               L 7/88C   1O   2          G   200.000  3500.000  1000.000    1
 3.85746029E+00 4.41437026E-03-2.21481404E-06 5.23490188E-10-4.72084164E-14    2
-4.87591660E+04 2.27163806E+00 2.35677352E+00 8.98459677E-03-7.12356269E-06    3
 2.45919022E-09-1.43699548E-13-4.83719697E+04 9.90105222E+00                   4
HCO               L12/89H   1C   1O   1     G   200.000  3500.000  1000.000    1
 2.77217438E+00 4.95695526E-03-2.48445613E-06 5.89161778E-10-5.33508711E-14    2
 4.01191815E+03 9.79834492E+00 4.22118584E+00-3.24392532E-03 1.37799446E-05    3
-1.33144093E-08 4.33768865E-12 3.83956496E+03 3.39437243E+00                   4
CH2O              L 8/88H   2C   1O   1     G   200.000  3500.000  1000.000    1
 1.76069008E+00 9.20000082E-03-4.42258813E-06 1.00641212E-09-8.83855640E-14    2
-1.39958323E+04 1.36563230E+01 4.79372315E+00-9.90833369E-03 3.73220008E-05    3
-3.79285261E-08 1.31772652E-11-1.43089567E+04 6.02812900E-01                   4
CH2OH             GUNL93C   1H   3O   1     G   200.000  3500.000  1000.000    1
 3.69266569E+00 8.64576797E-03-3.75101120E-06 7.87234636E-10-6.48554201E-14    2
-3.24250627E+03 5.81043215E+00 3.86388918E+00 5.59672304E-03 5.93271791E-06    3
-1.04532012E-08 4.36967278E-12-3.19391367E+03 5.47302243E+00                   4
CH3O              121686C   1H   3O   1     G   300.00   3000.00   1000.000    1
 0.03770799E+02 0.07871497E-01-0.02656384E-04 0.03944431E-08-0.02112616E-12    2
 0.12783252E+03 0.02929575E+02 0.02106204E+02 0.07216595E-01 0.05338472E-04    3
-0.07377636E-07 0.02075610E-10 0.09786011E+04 0.13152177E+02                   4
CH3OH             L 8/88C   1H   4O   1     G   200.000  3500.000  1000.000    1
 1.78970791E+00 1.40938292E-02-6.36500835E-06 1.38171085E-09-1.17060220E-13    2
-2.53748747E+04 1.45023623E+01 5.71539582E+00-1.52309129E-02 6.52441155E-05    3
-7.10806889E-08 2.61352698E-11-2.56427656E+04-1.50409823E+00                   4
C2H               L 1/91C   2H   1          G   200.000  3500.000  1000.000    1
 3.16780652E+00 4.75221902E-03-1.83787077E-06 3.04190252E-10-1.77232770E-14    2
 6.71210650E+04 6.63589475E+00 2.88965733E+00 1.34099611E-02-2.84769501E-05    3
 2.94791045E-08-1.09331511E-11 6.68393932E+04 6.22296438E+00                   4
C2H2              L 1/91C   2H   2          G   200.000  3500.000  1000.000    1
 4.14756964E+00 5.96166664E-03-2.37294852E-06 4.67412171E-10-3.61235213E-14    2
 2.59359992E+04-1.23028121E+00 8.08681094E-01 2.33615629E-02-3.55171815E-05    3
 2.80152437E-08-8.50072974E-12 2.64289807E+04 1.39397051E+01                   4
C2H3              L 2/92C   2H   3          G   200.000  3500.000  1000.000    1
 3.01672400E+00 1.03302292E-02-4.68082349E-06 1.01763288E-09-8.62607041E-14    2
 3.46128739E+04 7.78732378E+00 3.21246645E+00 1.51479162E-03 2.59209412E-05    3
-3.57657847E-08 1.47150873E-11 3.48598468E+04 8.51054025E+00                   4
```

```
C2H4              L 1/91C   2H   4          G   200.000  3500.000  1000.000    1
 2.03611116E+00 1.46454151E-02-6.71077915E-06 1.47222923E-09-1.25706061E-13    2
 4.93988614E+03 1.03053693E+01 3.95920148E+00-7.57052247E-03 5.70990292E-05    3
-6.91588753E-08 2.69884373E-11 5.08977593E+03 4.09733096E+00                   4
C2H5              L12/92C   2H   5          G   200.000  3500.000  1000.000    1
 1.95465642E+00 1.73972722E-02-7.98206668E-06 1.75217689E-09-1.49641576E-13    2
 1.28575200E+04 1.34624343E+01 4.30646568E+00-4.18658892E-03 4.97142807E-05    3
-5.99126606E-08 2.30509004E-11 1.28416265E+04 4.70720924E+00                   4
C2H6              L 8/88C   2H   6          G   200.000  3500.000  1000.000    1
 1.07188150E+00 2.16852677E-02-1.00256067E-05 2.21412001E-09-1.90002890E-13    2
-1.14263932E+04 1.51156107E+01 4.29142492E+00-5.50154270E-03 5.99438288E-05    3
-7.08466285E-08 2.68685771E-11-1.15222055E+04 2.66682316E+00                   4
CH2CO             L 5/90C   2H   2O   1     G   200.000  3500.000  1000.000    1
 4.51129732E+00 9.00359745E-03-4.16939635E-06 9.23345882E-10-7.94838201E-14    2
-7.55105311E+03 6.32247205E-01 2.13583630E+00 1.81188721E-02-1.73947474E-05    3
 9.34397568E-09-2.01457615E-12-7.04291804E+03 1.22156480E+01                   4
HCCO              SRIC91H   1C   2O   1     G  300.00    4000.00   1000.000    1
 0.56282058E+01 0.40853401E-02-0.15934547E-05 0.28626052E-09-0.19407832E-13    2
 0.19327215E+05-0.39302595E+01 0.22517214E+01 0.17655021E-01-0.23729101E-04    3
 0.17275759E-07-0.50664811E-11 0.20059449E+05 0.12490417E+02                   4
HCCOH              SRI91C   2O   1H   2     G   300.000  5000.000  1000.000    1
 0.59238291E+01 0.67923600E-02-0.25658564E-05 0.44987841E-09-0.29940101E-13    2
 0.72646260E+04-0.76017742E+01 0.12423733E+01 0.31072201E-01-0.50866864E-04    3
 0.43137131E-07-0.14014594E-10 0.80316143E+04 0.13874319E+02                   4
H2CN               41687H   2C   1N   1     G  300.00    4000.000  1000.000    1
 0.52097030E+01 0.29692911E-02-0.28555891E-06-0.16355500E-09 0.30432589E-13    2
 0.27677109E+05-0.44444780E+01 0.28516610E+01 0.56952331E-02 0.10711400E-05    3
-0.16226120E-08-0.23511081E-12 0.28637820E+05 0.89927511E+01                   4
HCN               GRI/98H   1C   1N   1     G   200.000  6000.000  1000.000    1
 0.38022392E+01 0.31464228E-02-0.10632185E-05 0.16619757E-09-0.97997570E-14    2
 0.14407292E+05 0.15754601E+01 0.22589886E+01 0.10051170E-01-0.13351763E-04    3
 0.10092349E-07-0.30089028E-11 0.14712633E+05 0.89164419E+01                   4
HNO               And93 H   1N   1O   1     G   200.000  6000.000  1000.000    1
 0.29792509E+01 0.34944059E-02-0.78549778E-06 0.57479594E-10-0.19335916E-15    2
 0.11750582E+05 0.86063728E+01 0.45334916E+01-0.56696171E-02 0.18473207E-04    3
-0.17137094E-07 0.55454573E-11 0.11548297E+05 0.17498417E+01                   4
N                 L 6/88N   1               G   200.000  6000.000  1000.000    1
 0.24159429E+01 0.17489065E-03-0.11902369E-06 0.30226245E-10-0.20360982E-14    2
 0.56133773E+05 0.46496096E+01 0.25000000E+01 0.00000000E+00 0.00000000E+00    3
 0.00000000E+00 0.00000000E+00 0.56104637E+05 0.41939087E+01                   4
NNH               T07/93N   2H   1          G   200.000  6000.000  1000.000    1
 0.37667544E+01 0.28915082E-02-0.10416620E-05 0.16842594E-09-0.10091896E-13    2
 0.28650697E+05 0.44705067E+01 0.43446927E+01-0.48497072E-02 0.20059459E-04    3
-0.21726464E-07 0.79469539E-11 0.28791973E+05 0.29779410E+01                   4
N2O               L 7/88N   2O   1          G   200.000  6000.000  1000.000    1
 0.48230729E+01 0.26270251E-02-0.95850874E-06 0.16000712E-09-0.97752303E-14    2
 0.80734048E+04-0.22017207E+01 0.22571502E+01 0.11304728E-01-0.13671319E-04    3
 0.96819806E-08-0.29307182E-11 0.87417744E+04 0.10757992E+02                   4
NH                And94 N   1H   1          G   200.000  6000.000  1000.000    1
 0.27836928E+01 0.13298430E-02-0.42478047E-06 0.78348501E-10-0.55044470E-14    2
 0.42120848E+05 0.57407799E+01 0.34929085E+01 0.31179198E-03-0.14890484E-05    3
 0.24816442E-08-0.10356967E-11 0.41880629E+05 0.18483278E+01                   4
NH2               And89 N   1H   2          G   200.000  6000.000  1000.000    1
 0.28347421E+01 0.32073082E-02-0.93390804E-06 0.13702953E-09-0.79206144E-14    2
 0.22171957E+05 0.65204163E+01 0.42040029E+01-0.21061385E-02 0.71068348E-05    3
-0.56115197E-08 0.16440717E-11 0.21885910E+05-0.14184248E+00                   4
NH3               J 6/77N   1H   3          G   200.000  6000.000  1000.000    1
 0.26344521E+01 0.56662560E-02-0.17278676E-05 0.23867161E-09-0.12578786E-13    2
-0.65446958E+04 0.65662928E+01 0.42860274E+01-0.46605230E-02 0.21718513E-04    3
-0.22808887E-07 0.82638046E-11-0.67417285E+04-0.62537277E+00                   4
NO                RUS 78N   1O   1          G   200.000  6000.000  1000.000    1
 0.32606056E+01 0.11911043E-02-0.42917048E-06 0.69457669E-10-0.40336099E-14    2
 0.99209746E+04 0.63693027E+01 0.42184763E+01-0.46389760E-02 0.11041022E-04    3
-0.93361354E-08 0.28035770E-11 0.98446230E+04 0.22808464E+01                   4
NO2               L 7/88N   1O   2          G   200.000  6000.000  1000.000    1
 0.48847542E+01 0.21723956E-02-0.82806906E-06 0.15747510E-09-0.10510895E-13    2
 0.23164983E+04-0.11741695E+00 0.39440312E+01-0.15854290E-02 0.16657812E-04    3
-0.20475426E-07 0.78350564E-11 0.28966179E+04 0.63119917E+01                   4
HCNO              BDEA94H   1N   1C   1O   1G   300.000  5000.000  1382.000    1
 6.59860456E+00 3.02778626E-03-1.07704346E-06 1.71666528E-10-1.01439391E-14    2
 1.79661339E+04-1.03306599E+01 2.64727989E+00 1.27505342E-02-1.04794236E-05    3
 4.41432836E-09-7.57521466E-13 1.92990252E+04 1.07332972E+01                   4
HOCN              BDEA94H   1N   1C   1O   1G   300.000  5000.000  1368.000    1
```

```
 5.89784885E+00 3.16789393E-03-1.11801064E-06 1.77243144E-10-1.04339177E-14    2
-3.70653331E+03-6.18167825E+00 3.78604952E+00 6.88667922E-03-3.21487864E-06    3
 5.17195767E-10 1.19360788E-14-2.82698400E+03 5.63292162E+00                   4
HNCO              BDEA94H  1N   1C   1O   1G   300.000  5000.000 1478.000    1
 6.22395134E+00 3.17864004E-03-1.09378755E-06 1.70735163E-10-9.95021955E-15    2
-1.66599344E+04-8.38224741E+00 3.63096317E+00 7.30282357E-03-2.28050003E-06    3
-6.61271298E-10 3.62235752E-13-1.55873636E+04 6.19457727E+00                   4
NCO               EA 93 N  1C   1O   1     G   200.000  6000.000 1000.000    1
 0.51521845E+01 0.23051761E-02-0.88033153E-06 0.14789098E-09-0.90977996E-14    2
 0.14004123E+05-0.25442660E+01 0.28269308E+01 0.88051688E-02-0.83866134E-05    3
 0.48016964E-08-0.13313595E-11 0.14682477E+05 0.95504646E+01                   4
CN                HBH92 C  1N   1          G   200.000  6000.000 1000.000    1
 0.37459805E+01 0.43450775E-04 0.29705984E-06-0.68651806E-10 0.44134173E-14    2
 0.51536188E+05 0.27867601E+01 0.36129351E+01-0.95551327E-03 0.21442977E-05    3
-0.31516323E-09-0.46430356E-12 0.51708340E+05 0.39804995E+01                   4
HCNN              SRI/94C  1N   2H   1     G   300.000  5000.000 1000.000    1
 0.58946362E+01 0.39895959E-02-0.15982380E-05 0.29249395E-09-0.20094686E-13    2
 0.53452941E+05-0.51030502E+01 0.25243194E+01 0.15960619E-01-0.18816354E-04    3
 0.12125540E-07-0.32357378E-11 0.54261984E+05 0.11675870E+02                   4
N2                121286N  2               G   300.000  5000.000 1000.000    1
 0.02926640E+02 0.14879768E-02-0.05684760E-05 0.10097038E-09-0.06753351E-13    2
-0.09227977E+04 0.05980528E+02 0.03298677E+02 0.14082404E-02-0.03963222E-04    3
 0.05641515E-07-0.02444854E-10-0.10208999E+04 0.03950372E+02                   4
AR                120186AR 1               G   300.000  5000.000 1000.000    1
 0.02500000E+02 0.00000000E+00 0.00000000E+00 0.00000000E+00 0.00000000E+00    2
-0.07453750E+04 0.04366000E+02 0.02500000E+02 0.00000000E+00 0.00000000E+00    3
 0.00000000E+00 0.00000000E+00-0.07453750E+04 0.04366000E+02                   4
C3H8              L 4/85C  3H   8          G   300.000  5000.000 1000.000    1
 0.75341368E+01 0.18872239E-01-0.62718491E-05 0.91475649E-09-0.47838069E-13    2
-0.16467516E+05-0.17892349E+02 0.93355381E+00 0.26424579E-01 0.61059727E-05    3
-0.21977499E-07 0.95149253E-11-0.13958520E+05 0.19201691E+02                   4
C3H7              L 9/84C  3H   7          G   300.000  5000.000 1000.000    1
 0.77026987E+01 0.16044203E-01-0.52833220E-05 0.76298590E-09-0.39392284E-13    2
 0.82984336E+04-0.15480180E+02 0.10515518E+01 0.25991980E-01 0.23800540E-05    3
-0.19609569E-07 0.93732470E-11 0.10631863E+05 0.21122559E+02                   4
CH3CHO            L 8/88C  2H   4O   1     G   200.000  6000.000 1000.000    1
 0.54041108E+01 0.11723059E-01-0.42263137E-05 0.68372451E-09-0.40984863E-13    2
-0.22593122E+05-0.34807917E+01 0.47294595E+01-0.31932858E-02 0.47534921E-04    3
-0.57458611E-07 0.21931112E-10-0.21572878E+05 0.41030159E+01                   4
CH2CHO            SAND86O  1H   3C   2     G   300.000  5000.000 1000.000    1
 0.05975670E+02 0.08130591E-01-0.02743624E-04 0.04070304E-08-0.02176017E-12    2
 0.04903218E+04-0.05045251E+02 0.03409062E+02 0.10738574E-01 0.01891492E-04    3
-0.07158583E-07 0.02867385E-10 0.15214766E+04 0.09558290E+02                   4
END
```

Transport data

```
TRANSPORT
AR                 0   136.500     3.330     0.000     0.000     0.000
C                  0    71.400     3.298     0.000     0.000     0.000 ! *
C2                 1    97.530     3.621     0.000     1.760     4.000
C2O                1   232.400     3.828     0.000     0.000     1.000 ! *
CN2                1   232.400     3.828     0.000     0.000     1.000 ! OIS
C2H                1   209.000     4.100     0.000     0.000     2.500
C2H2               1   209.000     4.100     0.000     0.000     2.500
C2H2OH             2   224.700     4.162     0.000     0.000     1.000 ! *
C2H3               2   209.000     4.100     0.000     0.000     1.000 ! *
C2H4               2   280.800     3.971     0.000     0.000     1.500
C2H5               2   252.300     4.302     0.000     0.000     1.500
C2H6               2   252.300     4.302     0.000     0.000     1.500
C2N                1   232.400     3.828     0.000     0.000     1.000 ! OIS
C2N2               1   349.000     4.361     0.000     0.000     1.000 ! OIS
C3H2               2   209.000     4.100     0.000     0.000     1.000 ! *
C3H4               1   252.000     4.760     0.000     0.000     1.000
C3H6               2   266.800     4.982     0.000     0.000     1.000
C3H7               2   266.800     4.982     0.000     0.000     1.000
C4H6               2   357.000     5.180     0.000     0.000     1.000
I*C3H7             2   266.800     4.982     0.000     0.000     1.000
N*C3H7             2   266.800     4.982     0.000     0.000     1.000
```

```
C3H8          2   266.800   4.982   0.000   0.000    1.000
C4H           1   357.000   5.180   0.000   0.000    1.000
C4H2          1   357.000   5.180   0.000   0.000    1.000
C4H2OH        2   224.700   4.162   0.000   0.000    1.000  !  *
C4H8          2   357.000   5.176   0.000   0.000    1.000
C4H9          2   357.000   5.176   0.000   0.000    1.000
I*C4H9        2   357.000   5.176   0.000   0.000    1.000
C5H2          1   357.000   5.180   0.000   0.000    1.000
C5H3          1   357.000   5.180   0.000   0.000    1.000
C6H2          1   357.000   5.180   0.000   0.000    1.000
C6H5          2   412.300   5.349   0.000   0.000    1.000  !  JAM
C6H5O         2   450.000   5.500   0.000   0.000    1.000  !  JAM
C5H5OH        2   450.000   5.500   0.000   0.000    1.000  !  JAM
C6H6          2   412.300   5.349   0.000   0.000    1.000  !  SVE
C6H7          2   412.300   5.349   0.000   0.000    1.000  !  JAM
CH            1    80.000   2.750   0.000   0.000    0.000
CH2           1   144.000   3.800   0.000   0.000    0.000
CH2(S)        1   144.000   3.800   0.000   0.000    0.000
CH2*          1   144.000   3.800   0.000   0.000    0.000
CH2CHCCH      2   357.000   5.180   0.000   0.000    1.000  !  JAM
CH2CHCCH2     2   357.000   5.180   0.000   0.000    1.000  !  JAM
CH2CHCH2      2   260.000   4.850   0.000   0.000    1.000  !  JAM
CH2CHCHCH     2   357.000   5.180   0.000   0.000    1.000  !  JAM
CH2CHCHCH2    2   357.000   5.180   0.000   0.000    1.000  !  JAM
CH2CO         2   436.000   3.970   0.000   0.000    2.000
CH2O          2   498.000   3.590   0.000   0.000    2.000
CH2OH         2   417.000   3.690   1.700   0.000    2.000
CH3           1   144.000   3.800   0.000   0.000    0.000
CH3CC         2   252.000   4.760   0.000   0.000    1.000  !  JAM
CH3CCCH2      2   357.000   5.180   0.000   0.000    1.000  !  JAM
CH3CCCH3      2   357.000   5.180   0.000   0.000    1.000  !  JAM
CH3CCH2       2   260.000   4.850   0.000   0.000    1.000  !  JAM
CH3CHCH       2   260.000   4.850   0.000   0.000    1.000  !  JAM
CH3CH2CCH     2   357.000   5.180   0.000   0.000    1.000  !  JAM
CH3CHO        2   436.000   3.970   0.000   0.000    2.000
CH2CHO        2   436.000   3.970   0.000   0.000    2.000
CH3CO         2   436.000   3.970   0.000   0.000    2.000
CH3O          2   417.000   3.690   1.700   0.000    2.000
CH3OH         2   481.800   3.626   0.000   0.000    1.000  !  SVE
CH4           2   141.400   3.746   0.000   2.600   13.000
CH4O          2   417.000   3.690   1.700   0.000    2.000
CN            1    75.000   3.856   0.000   0.000    1.000  !  OIS
CNC           1   232.400   3.828   0.000   0.000    1.000  !  OIS
CNN           1   232.400   3.828   0.000   0.000    1.000  !  OIS
CO            1    98.100   3.650   0.000   1.950    1.800
CO2           1   244.000   3.763   0.000   2.650    2.100
H             0   145.000   2.050   0.000   0.000    0.000
H2C4O         2   357.000   5.180   0.000   0.000    1.000  !  JAM
H2            1    38.000   2.920   0.000   0.790  280.000
H2CCCCH       2   357.000   5.180   0.000   0.000    1.000  !  JAM
H2CCCCH2      2   357.000   5.180   0.000   0.000    1.000  !  JAM
H2CCCH        2   252.000   4.760   0.000   0.000    1.000  !  JAM
H2CN          1   569.000   3.630   0.000   0.000    1.000  !  os/jm
H2NO          2   116.700   3.492   0.000   0.000    1.000  !  JAM
H2O           2   572.400   2.605   1.844   0.000    4.000
H2O2          2   107.400   3.458   0.000   0.000    3.800
HC2N2         1   349.000   4.361   0.000   0.000    1.000  !  OIS
HCCHCCH       2   357.000   5.180   0.000   0.000    1.000  !  JAM
HCCO          2   150.000   2.500   0.000   0.000    1.000  !  *
HCNN          2   150.000   2.500   0.000   0.000    1.000  !  *
HCCOH         2   436.000   3.970   0.000   0.000    2.000
HCN           1   569.000   3.630   0.000   0.000    1.000  !  OIS
HCO           2   498.000   3.590   0.000   0.000    0.000
HE            0    10.200   2.576   0.000   0.000    0.000  !  *
HCNO          2   232.400   3.828   0.000   0.000    1.000  !  JAM
HOCN          2   232.400   3.828   0.000   0.000    1.000  !  JAM
HNCO          2   232.400   3.828   0.000   0.000    1.000  !  OIS
HNNO          2   232.400   3.828   0.000   0.000    1.000  !  *
HNO           2   116.700   3.492   0.000   0.000    1.000  !  *
HNOH          2   116.700   3.492   0.000   0.000    1.000  !  JAM
HO2           2   107.400   3.458   0.000   0.000    1.000  !  *
N             0    71.400   3.298   0.000   0.000    0.000  !  *
N2            1    97.530   3.621   0.000   1.760    4.000
```

```
N2H2              2    71.400     3.798     0.000     0.000     1.000  !  *
N2H3              2   200.000     3.900     0.000     0.000     1.000  !  *
N2H4              2   205.000     4.230     0.000     4.260     1.500
N2O               1   232.400     3.828     0.000     0.000     1.000  !  *
NCN               1   232.400     3.828     0.000     0.000     1.000  !  OIS
NCO               1   232.400     3.828     0.000     0.000     1.000  !  OIS
NH                1    80.000     2.650     0.000     0.000     4.000
NH2               2    80.000     2.650     0.000     2.260     4.000
NH3               2   481.000     2.920     1.470     0.000    10.000
NNH               2    71.400     3.798     0.000     0.000     1.000  !  *
NO                1    97.530     3.621     0.000     1.760     4.000
NCNO              2   232.400     3.828     0.000     0.000     1.000  !  OIS
NO2               2   200.000     3.500     0.000     0.000     1.000  !  *
O                 0    80.000     2.750     0.000     0.000     0.000
O2                1   107.400     3.458     0.000     1.600     3.800
OH                1    80.000     2.750     0.000     0.000     0.000
END
```

Appendix E

MATLAB code

Turbulence boundary condition profiles

```
%% Turbulence Boundary Condition Writer
% Summary:  Scales the inlet turbulence intensity of an inlet profile to prescribed
%           value TI_2
%
% Inputs:   'inlet_turbulence_profile.xlsx' - contains the point profile file of
%           turbulence parameters given by an earlier pipe simulation
%           'inlet_coords.xlsx' - contains the coordinates of the inlet in
%           the mesh to be used, in case they are different from those in
%           the 'inlet_turbulence_profile' file.
%
% Outputs:  'scaled_turbulence_profile.txt' - contains the point profile of
%           turbulence parameters, scaled to turbulence intensity TI_2, at the
%           specified coordinates.
% Author:   Hampus Olsson, Department of Energy Science, Lund University

clear all
close all
clc

% Read excel turbulence profile data
[inlet_turb_num,inlet_turb_txt,inlet_turb_raw] = xlsread('inlet_turbulence_profile.xlsx');

% Evaluate number of points in profile
nbr_p = length(inlet_turb_num(:,1));

% Read excel inlet coordinates
[coord_num,coord_txt,coord_raw] = xlsread('inlet_coords.xlsx');

xcoord = coord_num(:,1);
ycoord = coord_num(:,2);
zcoord = coord_num(:,3);

% Open .txt file to write .prof
fileID = fopen('scaled_turbulence_profile.txt','w');

% Specify turbulence intensities
TI_1 = mean(inlet_turb_num(:,6)); % Current mean turbulence intensity
TI_2 = 0.1;                        % Prescribed mean turbulence intensity

% Create scaled profile matrix at inlet
% First four columns are node number, x, y and z coordinates
turb_scaled = inlet_turb_num;
turb_scaled(:,5) = inlet_turb_num(:,5).*(TI_2/TI_1)^2; % Tke
turb_scaled(:,6) = inlet_turb_num(:,6).*(TI_2/TI_1); % TI
turb_scaled(:,7) = inlet_turb_num(:,7).*(TI_2/TI_1)^3; % Epsilon
turb_scaled(:,8) = inlet_turb_num(:,8).*(TI_2/TI_1); % Omega

% Write scaled profile to .txt
```

```
fprintf(fileID,['((air_inlet point ', num2str(nbr_p),' \r\n']);

for i = 1:length(turb_scaled(1,:))
    if i <= 3

    fprintf(fileID,'(%s \r\n',inlet_turb_txt{5,i});
    fprintf(fileID,'%.8g \r\n',turb_scaled(:,i));
    fprintf(fileID,') \r\n');

    else

    fprintf(fileID,'(%s \r\n',inlet_turb_txt{5,i});
    fprintf(fileID,'%8f \r\n',turb_scaled(:,i));
    fprintf(fileID,') \r\n');
    end
end

fclose(fileID);
```